DESIGN AND PREPARATION OF ELECTRICALLY CONDUCTIVE GRAPHENE NANOCOMPOSITES BASED ON PA6/POE

Milad Hadaeghnia

A Thesis

In the department

of

Mechanical Engineering

Presented in Partial Fulfillment of Requirements

For the Degree of

Doctor of Philosophy (Mechanical engineering) at

Concordia University

Montreal, Quebec, Canada

April 2022

CONCORDIA UNIVERSITY

School of Graduate Studies

This is to certify that the thesis prepared

By: **Milad Hadaeghnia**

Entitled: **Design and preparation of electrically conductive graphene nanocomposites based on PA6/POE**

and submitted in partial fulfillment of the requirements for the degree of:

Doctor of Philosophy (Mechanical Engineering)

complies with the regulations of the University and meets the accepted standards with respect to originality and quality.

Signed by the final examining committee:

_______________________________________ Chair

Dr. Chun Wang

_______________________________________ External Examiner

Dr. Marianna Kontopoulou

_______________________________________ External to Program

Dr. Zhibin Ye

_______________________________________ Examiner

Dr. Martin D. Pugh

_______________________________________ Examiner
Dr. Mehdi Hojjati

_______________________________________ Thesis Co-Supervisor

Dr. Paula Wood-Adams

_______________________________________ Thesis Co-Supervisor

Dr. Shervin Ahmadi

Approved by

____

Dr. Ivan Contreras, Graduate Program Director

____

Dr. Mourad Debbabi, Dean
Gina Cody School of Engineering and Computer Science

____

Date 4/14/2022

____

ABSTRACT

Design and preparation of electrically conductive graphene nanocomposites based on PA6/POE

Milad Hadaeghnia, Ph.D.

Concordia University 2022

Polymer blending is commonly used to engineer materials with favorable properties. Due to the low entropy of mixing, in most cases, polymer blending results in a phase-separated morphology which governs the ultimate properties. Nanoparticles can significantly alter the phase morphology even at low contents. In the case of droplet-matrix morphology, the addition of nanoparticles can cause refinement, produce large and irregular domains, or even induce a co-continuous morphology. By employing a proper strategy of mixing for a particular system it is possible to manipulate the morphology and achieve desired properties. In this study, I investigate the impact of graphene particles on the phase morphology and mechanical and electrical properties of polyamide 6/ polyolefin elastomer blends. It is shown that a wide range of properties can be obtained by changing the composition and the localization of graphene. Inducing a co-continuous morphology at low graphene host phase content results in unique mechanical and electrical properties. The mechanism of graphene-induced co-continuity was further investigated by changing the rheological properties of the POE and the addition of compatibilizer. I found that the final phase morphology is governed by the structural features of the graphene network structure which in turn is dependent on the self-assembly of graphene particles.

The graphene 3D structure and phase morphology are not stable and evolve during annealing. Rheological and morphological characterization were employed to track the evolution of microstructure and correlate the relationship between self-similar graphene 3D structure and phase morphology. It is revealed that the graphene content and annealing time have the same impact on the rheological and electrical properties.

DEDICATION

I dedicate this thesis to my parents and my brothers who have been constant source of love, support, and encouragement in my life.

To Farnaz who has been always there for me. I am grateful to have you in my life.

ACKNOWLEDGMENT

I would like to express my deepest appreciation to my supervisors: Professors Wood-Adams, Ahmadi and Ghasemi for their invaluable support and guidance. I am grateful to my family for their unceasing support and encouragement. Last but not least, I would like to thank all my friends and lab mates for their help.

CONTRIBUTION OF AUTHORS

Chapter 3 of this thesis,

Milad Hadaeghnia, Shervin Ahmadi, Ismaeil Ghasemi, and Paula M. Wood-Adams. "Manipulating the morphology of PA6/POE blends using graphene to achieve balanced electrical and mechanical properties." Composites Science and Technology 200 (2020): 108412.

This chaper is an article co-authored with Dr. Shervin Ahmadi, Dr. Ismaeil Ghasemi and Dr. Wood-Adams. This work was conceptualized by Ahmadi and myself. I have designed, performed the experiments and wrote the first draft of manuscript under the supervision of Wood-Adams, Ahamdi and Ghasemi. The manuscript was further revised by Wood-Adams. Sample preparation and primarily tests were conducted at the Iran Polymer and Petrochemical Institute and complementary tests were performed at Concordia University.

Chapter 4 of this thesis,

Hadaeghnia, M., Ahmadi, S., Ghasemi, I., & Wood-Adams, P. M. “Evolution of Phase Morphology, Rheology, and Electrical Conductivity of PA6/POE Blends Containing Graphene during Annealing under SAOS”. Macromolecules (2022).

This chaper is an article co-authored with Dr. Shervin Ahmadi, Dr. Ismaeil Ghasemi and Dr. Wood-Adams. This work was conceptualized by myself. I have designed, performed the experiments and wrote the first draft of manuscript under the supervision of Wood-Adams, Ahamdi and Ghasemi. The manuscript was further revised by Wood-Adams. Sample preparation were conducted at the Iran Polymer and Petrochemical Institute and complementary tests were performed at Concordia University.

Chapter 5 of this thesis,

Hadaeghnia, M., Ahmadi, S., Ghasemi, I., & Wood-Adams, P. M. “Effect of minor phase rheological properties and compatibilization on co-continuity, rheological and electrical properties of PA6/POE blends containing graphene, Journal of Rheology” (to be submitted).

This work was conceptualized by myself. I have designed, performed the experiments and wrote the first draft of manuscript under the supervision of Wood-Adams, Ahamdi and Ghasemi. The manuscript was further revised by Wood-Adams. Sample preparation were conducted at the Iran Polymer and Petrochemical Institute and complementary tests were performed at Concordia University.

TABLE OF CONTENTS

LIST OF FIGURES

LIST OF TABLES

1. INTRODUCTION

Polymer blending is a versatile and effective strategy to produce new materials with desirable properties. Most polymer pairs are incompatible, resulting in formation of a phase separated morphology. The properties of a polymer blend are governed by the intrinsic properties of the components and the blend phase morphology. The phase morphology is governed by various factors such as composition and rheological properties of the components and interfacial tension between the components. Depending on these factors, a wide range of morphologies can be formed in binary polymer blends such as droplet-matrix, fibrillar, lamellar and co-continuous morphology.

Each morphology has its unique properties which can be used in a specific application. In dispersed-matrix morphology, the properties are dominated by the matrix phase. Due to the anisotropic structure of the fibrillar morphology, they typically exhibit superior mechanical properties in the direction of the fibrils[1]. In the interpenetrated structure of the co-continuous morphology, both components significantly contribute to the properties [2].

In order to further modify the properties of polymer blends or to induce new properties such as specific magnetic, electrical and optical properties, nanoparticles are incorporated into the blends [3-5]. Due to the high specific surface area, nanoparticles have a considerable impact on the properties of the host phase. Accordingly, nanoparticles have received a great deal of attention over the past decades among which carbon black (CB), carbon nanotube (CNT) and graphene are the three most important carbon-based nanoparticles widely used as conductive nanoparticles in polymer blends.

Graphene is composed of a single atomic layer of sp^2 carbons arrange in a honeycomb structure forming a 2-dimensional sheet[6]. Outstanding mechanical, thermal and electrical properties make graphene a perfect candidate for practical applications [6]. A theoretical study by Xie et al showed that due to high surface area, the impact of graphene nanosheet on electrical conductivity of nanocomposites is more pronounced than carbon nanotube (CNT) and carbon black (Fig. 1-1)[7]. However, it is worth mentioning that the dispersion state of nanoparticles can significantly affect the induction of electrical conductivity[8]. This is particularly important in graphene-based nanocomposites due to the strong tendency of graphene sheets for restacking and aggregation.

In order for nanocomposites containing conductive filler to become electrically conductive, the conductive filler should form a continuous pathway through the material. This occurs at a critical concentration called the percolation threshold (Fig. 1-2). At this point, the electrical conductivity increases significantly with increasing filler content.

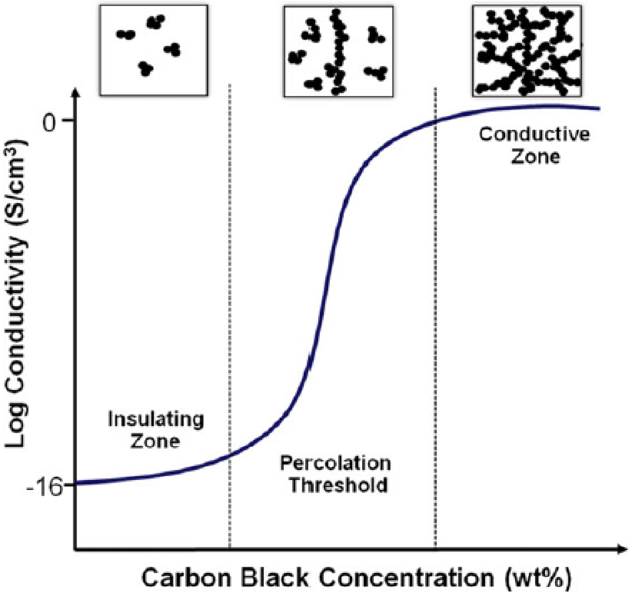

Figure 1-1. Electrical conductivity dependence of nanocomposite as a function of CB content[9].

Generally, the incorporation of a high amount of electrically conductive filler has a detrimental impact on the final mechanical properties such as ductility. Additionally, it increases the viscosity of the polymer matrix which restricts the processability of the material. Accordingly, researchers are looking for strategies to minimize the amount of particle required for the electrical percolation. This is especially of importance in nanocomposites prepared by melt mixing in which poor nanoparticle dispersion usually leads to high percolation thresholds. For instance, In the case of Polyamide 6 (PA6)/graphene nanoplatelet nanocomposites prepared by melt mixing in twin screw extruder, Mayoral et al observed a percolation threshold between 10-15wt% of graphene nanoplatelet[10]. Solvent mixing can be used to enhance the dispersion of particles and reduce the percolation threshold. Papadopoulou et al used a mixture of trifluoroacetic acid (TFA) and acetone to dissolve PA6,6 and disperse graphene nanoplatelets achieving a fine graphene nanoplatelet dispersion which resulted in high electrical conductivity (10^{-2}S/cm) at 20wt% loading[11]. Another approach to prepare PA6/ graphene nanocomposites is in-situ polymerization of ε-caprolactam monomer. Zheng et al produced PA6/ thermally reduced graphene oxide (TRG) nanocomposites by first dispersing the graphene oxide and monomers and then polymerizing theε-caprolactam at high temperature (220°C) [12]. High temperature polymerization also leads to thermal reduction of graphene oxide retaining the conductivity of the nanoparticle. This results in a low percolation threshold (0.41vol%) and high conductivity 0.028 S/cm at 1.64vol% of TRG[12]. Although nanocomposites prepared by in-situ polymerization and solvent mixing usually show a better dispersion state, melt mixing is more economical and environmentally friendly and can be easily scaled up [6] motivating researchers to reduce the percolation threshold in this processing method.

An effective strategy to reduce the percolation threshold of an electrically conductive filler is to take advantage of a double percolated structure in immiscible polymer blends. Double percolation refers to a situation where the fillers are selectively localized inside one of the components and form a percolated structure and the host phase is also continuous throughout the blend [13]. Accordingly, we can significantly reduce the percolation threshold by selective localization of nanoparticles inside one phase or at the interface of a polymer blend with a co-continuous morphology. For this reason, the co-continuous morphology has received a great deal of attention in designing electrically conductive nanocomposites. Generally, co-continuous morphologies only form within a limited range of compositions restricting the range of achievable properties. Although, studies have shown that it is possible to manipulate the morphology and achieve a co-continuous morphology over a broader range of composition by the incorporation of nanoparticles [14], the formation of phase morphology in the presence of nanoparticles is rather a complex process in which various factors play a role and far from being fully understood.

1.1. Motivations and objectives

The main goal of this study is to investigate the impact of graphene on the morphology and final properties of PA6/POE and to understand the relationship between the microstructure and final properties. I use polyamide 6 (PA6) as the major phase due to its desirable thermal and mechanical properties. PA6 is an engineering thermoplastic which is widely used in industry due to its unique properties such as high corrosion and abrasion resistance, high mechanical strength and high melting temperature[15]. On the other hand, polyamide has some drawbacks restricting its application such as notch sensitivity, low impact strength and poor dimensional stability. An effective approach to overcome these drawbacks and improve the properties of polyamide is blending the PA with polyolefins[15]. Accordingly, I use a polyolefin elastomer as the minor phase to not only improve the properties of the PA phase but also reduce the electrical percolation threshold of graphene using the double percolated structure. Besides their mechanical properties, this blend also provides a model system for developing our understanding of the physical properties of such complex materials. The challenge with blends of POE and PA6 is their very different interfacial tensions and its impact on obtaining co-continuity. The impact of nanoparticles on co-continuity of blends with high interfacial tension has been less studied due to this challenge. It will be revealed that by using graphene nanoparticles it is possible to retain the good mechanical properties of PA6 while creating a co-continuous morphology with high conductivity. Finally, this model blend allows investigating the dual effect of reactive compatibilizer and graphene particle on the phase morphology and properties.

In the first step, the effect of graphene localization on the morphology and properties of nanocomposites such as electrical, mechanical and rheological properties will be examined in two different blend compositions : (i) 60/40, a composition close to phase inversion and (ii) 80/20, asymmetric composition where PA forms the matrix phase and requires graphene to induce co-continuous morphology. In this step, I aim at clarifying the influence of the mixing sequence on the localization of graphene and factors affecting the migration of graphene platelets. Additionally, preparing the nanocomposites at two blend compositions allows us to compare the final properties and highlight the impact of graphene induced co-continuity on properties. It will be shown that formation of co-continuous morphology at lower content of POE phase results in unique electrical and mechanical properties.

In the next step, the evolution of morphology and rheological and electrical properties during annealing are investigated for the 80/20 system. Studying the impact of annealing on microstructure of electrically conductive nanocomposite blends is important both from practical and fundamental point of view. Generally, during annealing, nanoparticles rearrange which can lead to formation of a more interconnected 3D structure. In the case of electrically conductive nanoparticles, this leads to a sharp increase in conductivity which can be used as an effective approach to lower the percolation threshold. In polymer blends, the phase morphology can also change during annealing particularly in the case of blends with high interfacial tension between the components. Therefore, it is important to understand how nanoparticle rearrange in the case of such nanocomposite blends, and how this can affect the phase stability during annealing and post processing conditions. The rheological response of these materials is very sensitive to the nanoparticle 3D structure and the phase morphology. Since rheology is a powerful tool and widely used in characterizing the nanocomposites, it is important to understand the impact of these factors during rheological measurement. Accordingly, two annealing conditions were considered: (i) annealing under small amplitude oscillatory shear (SAOS) where the sample is subjected to compression force and shear, and (ii) quiescent conditions. Additionally, the correlation between the morphological evolution with rheological and electrical properties are explored.

Finally, I investigate the effect of minor phase rheological properties and compatibilizer in polyamide 6/POE/graphene nanocomposites with an asymmetric composition (80/20) on the phase morphology and rheological and electrical properties. This allows us to have better understanding regarding the mechanism of graphene induced co-continuity.

2. LITERATURE REVIEW

Due to the impact of morphology on the rheological and mechanical properties of polymer blends, many studies have been devoted to understanding the factors controlling the evolution and formation of morphology over the past decades. These investigations started with dilute binary blends consisting of two Newtonian fluid in a simple stress fields to concentrated viscoelastic polymer blends in complex flow fields. Based on these studies, in this chapter I aim at discussing the factors involving in the formation of phase morphology in polymer binary blends. I begin with the fundamental aspect of process and then the effect of nanoparticle on the morphology will be discussed. Due to the considerable effect of nanoparticle localization on the morphology, factors governing the migration and the final localization of nanoparticle are discussed; finally, the last section is devoted to the influence of electrically conductive nanoparticles on the electrical properties and relation between the microstructure and electrical properties in polymer blends.

2.1. Evolution of morphology in polymer blends during mixing

In order to get acquainted with the stages involved in the morphology formation during mixing, let us consider the mixing of two polymers A and B in an internal mixer or extruder. If we assume that polymer A has a lower melting temperature (or a lower softening temperature for amorphous polymers), the viscosity of polymer A is lower than that of B and/or the volume fraction of component A is larger than that of component B ($\varphi_A > \varphi_B$), polymer A melts before B and forms a continuous phase. At this stage we have a suspension consisting of particles of polymer B (still in the solid state) suspended in the polymer A (in the molten state)[16]. It has been shown that when the blend temperature reaches the softening temperature of polymer B, these suspended domains deform to sheet and ribbon structures due to the mechanical force applied during mixing [17]. These sheets get thinner, and holes appear on these sheets mainly due to impurities and the wave instability[17]. These holes coalesce with one another leading to the formation of lace-like structure. Then, these laces break up to elongated domains, long threads and droplets. These morphological processes are presented in Fig. 2-1, Note that all of these changes occur only within 2 minutes of mixing. Eventually, all domains break up to discrete spherical domains resulting in the formation of a droplet matrix morphology. As the mixing proceeds, the droplets become smaller until reaching an equilibrium size.

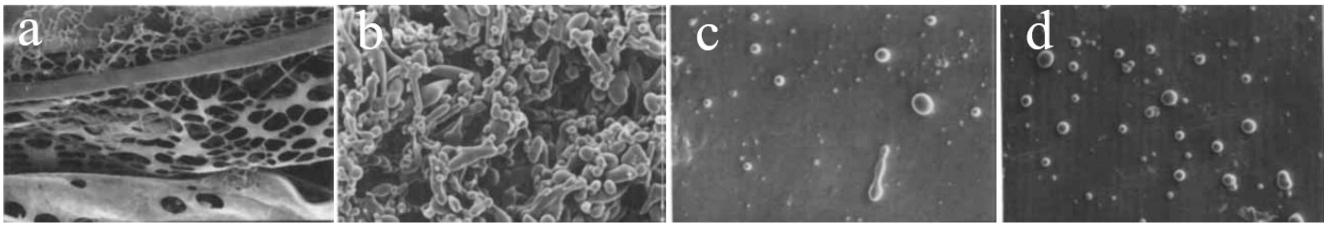

Figure 2-1 Evolution of morphology during mixing in an internal mixer. morphology after a) 1 minute, b)1.5 minute, c)2.5 minutes, d) 7 minutes [17].

Now consider a situation where polymer A has a higher melting temperature than polymer B. At the early stage of mixing, polymer B melts before polymer A and forms the continuous phase. It is well known that a component with lower viscosity has greater tendency to form the continuous phase [18, 19]. As a result, with increasing the temperature, polymer A melts and tends to form the continuous phase; therefore, at a certain stage of the mixing, there would be a transient co-continuous morphology. This morphology can be kinetically trapped by decreasing the temperature below the melting temperature of components. However, this morphology is not thermodynamically stable, and by further mixing or by annealing, phase inversion occurs and polymer B breaks up into discrete domains resulting in the formation of a dispersed morphology. These morphological evolutions are summarized in Fig. 2-2 which highlights the impact of mixing time.

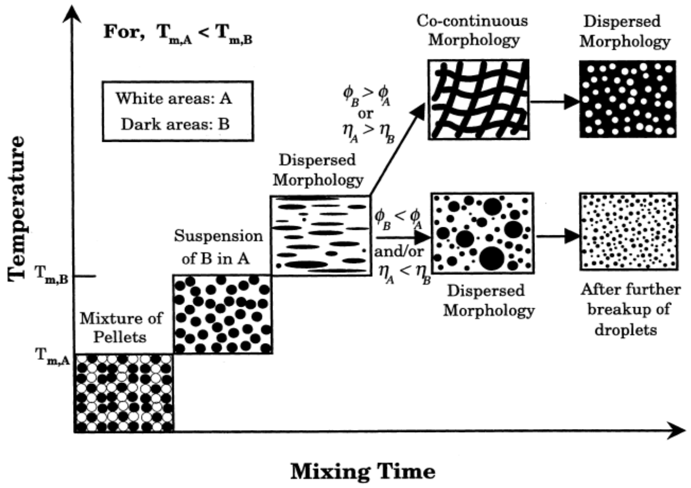

Figure 2-2. Evolution of morphology during mixing where polymer B has higher melting temperature in comparison to that of polymer A [16].

The main question is what are the relevant factors affecting the final morphology i.e. the droplet size and distribution.

The droplet deformation can be explained by two dimensionless parameters: (i) capillary number (Ca) and (ii) viscosity ratio (p) defined as follows:

$$Ca = \dot{\gamma}\eta_m R/\sigma \qquad (2\text{-}1)$$

$$p = \frac{\eta_d}{\eta_m} \qquad (2\text{-}2)$$

Here, $\dot{\gamma}$, η_m, η_d,R, σ , are shear rate, viscosity of matrix phase, viscosity of dispersed phase, radius of dispersed phase and interfacial tension, respectively. The capillary number indicates the balance between viscous and interfacial forces. Interfacial tension tends to keep the dispersed phase in a spherical shape with lower interfacial area while the viscous force deforms the droplets to an elongated shape.

Let us consider the mixing of a large spherical domain (dispersed domain) suspended in a continuous phase (matrix). At the early stage of mixing, the capillary number is large (interfacial force is negligible) leading to elongation and folding of the interface [20]. At low capillary number the droplet deforms into a stable ellipsoidal shape. However, when the capillary number exceeds a critical value (Ca_{crit}) elongated domains become unstable and eventually break up to smaller droplets. The value of Ca_{crit} depends on the viscosity ratio of components and flow type (Fig. 2-3). Studies showed that the critical capillary number is lower in elongational flow as compared to shear flow. This shows that elongational flow has greater ability to break the dispersed phase [21].

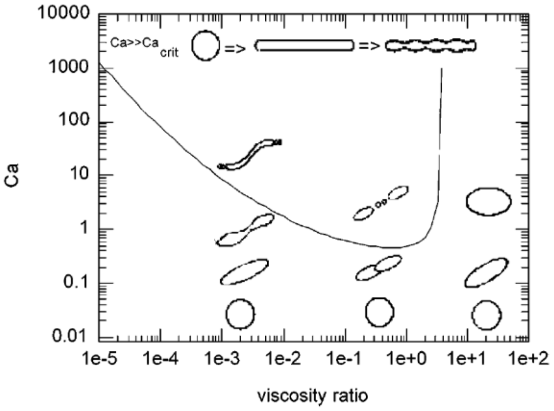

Figure 2-3. Critical capillary number in simple shear flow. The schemes below and above the line show the steady shape and break up modes, respectively [22].

However, break up is not the only factor controlling the droplet size and distribution in polymer blends. Convection during mixing causes the dispersed phase domains to collide with one another. The collision between these domains can lead to coalescence, increasing the domain size. Depending on the size of the resultant domain, it can undergo the break-up process again. Therefore, the final morphology is governed by the balance between break-up and coalescence.

In the following sections, we discuss the break-up and coalescence process and factors affecting them.

2.2. Break up

Generally, droplets can break up through 4 mechanisms depending on the capillary number and viscosity ratio [20, 22]. At capillary numbers close to Ca_{crit} , i.e. droplet is moderately elongated, the mode of breakup depends on the viscosity ratio. For viscosity ratio close to unity, break up occurs by the necking mechanism. In this mechanism, the droplet deforms to a dumbbell shape. As the droplet is stretched, the neck gets thinner and eventually breaks up to small droplets (satellite drops) between two large drops (daughter droplet) (Fig. 2-3). In the case of blends with low viscosity ratio tip-streaming takes place (Fig. 2-3). In this mechanism, small droplets release from the tips of deformed domains due to an interfacial tension gradient along the interface[23].

If the aspect ratio of the elongated domain is slightly larger than the critical value for breakup $L/R_o > (L/R_o)_{\text{critical}}$, where L and R_o are the length of the deformed domain and initial radius of droplet respectively, after the cessation of flow the ends of stretched filament retract back to rounded shapes and pinch off from the elongated domain which is termed “end pinching” mechanism[20]. Depending on the aspect ratio of the resultant filament it can again undergo the end pinching mechanism until reaching a stable size.

In the case of large capillary number where the droplet deforms to a highly elongated thread (filament) the domain breaks up through capillary-wave instability [22]. In this situation the thin filament is not stable to small perturbations caused by the interfacial tension. These sinusoidal perturbations tend to reduce the interfacial area. Threads broken up through this mechanism disintegrate into a number of large droplets with small satellite droplets between them. Generally, in the absence of coalescence, the droplets produced by this mechanism have sizes lower than the critical radius to undergo the breakup process again. This mechanism occurs for highly elongated domains both during flow and quiescence (after cessation of flow) and is the dominant break-up mechanism in polymer processing conditions.

2.2.1. Effect of nanoparticles on break up

As discussed, the breakup of dispersed domains strongly depends on the viscosity ratio. Nanoparticles significantly alter the viscosity of the host phase which subsequently affects the break-up process [24]. Kong *et al* have shown that the presence of nanoparticles inside the dispersed domain increases the critical aspect ratio for droplet break-up and slows down the relaxation of these domains[25]. Fig. 2-4 illustrates the break-up behavior of moderately elongated polyamide 6 (PA6) domains in polystyrene (PS) in quiescence condition for unfilled and filled PA6 droplet with silica nanoparticles [25]. In the case of the unfilled domain, the break up occurs with the end-pinching mechanism. However, in the case of the filled PA6, the domain does not break at the same elongational aspect ratio and retracts back to a spherical shape driven by interfacial tension. This shows that the presence of nanoparticles inside the dispersed domain increases the critical aspect ratio for break up. The authors also investigated the relaxation dynamics of the dispersed phase as a function of nanoparticle content and concluded that the incorporation of nanoparticle significantly slows down the shape relaxation of deformed domain. The shape relaxation of dispersed phase is governed by the droplet size, viscosity ratio and interfacial tension. By calculating the interfacial tension for the filled and unfilled systems, it was revealed that the increase in the relaxation time of dispersed phase is due to the viscosity ratio which had greater contribution to the total relaxation time[25].

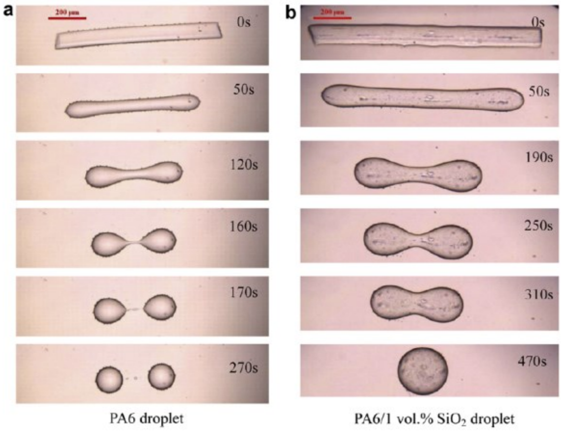

Figure 2-4. Relaxation of moderately deformed PA6 droplet in PS matrix. A) unfilled PA6 domain (aspect ratio = 10.8), b) filled PA6 domain with 1% of nano silica (aspect ratio = 11.5)[25].

Besides the impact of nanoparticle on the viscosity of dispersed phase, other factors can also enhance the stability of elongated domains. Studies have shown that interfacially adsorbed nanoparticle can reduce the interfacial tension between the polymer phases stabilizing the morphology during annealing [26-28]. The stabilization effect is more pronounced in the case of nanoparticles with high aspect ratios [29, 30]. Owing to their high aspect ratio they can cover the interfacial area at a lower particle content. Additionally, the bending stiffness of these particles can contribute to stabilization of the deformed domain against interfacial tension [29].

Since the percolation threshold for the elongated domains is significantly lower in comparison to that of the spherical domains [31], the formation of stable elongated domains during processing can promote the co-continuous morphology in a lower content of minor phase. Gubbles *et al*. showed that selective localization of carbon black in the minor phase or at the interface of the blend components extended the composition range over which co-continuity was possible [14]. This is a promising strategy to manipulate the morphology of electrically conductive nanocomposites to achieve desirable electrical and mechanical properties. In polymer blends, co-continuous morphology generally exists in the middle range of composition. Therefore, reducing the volume fraction required for continuity of the phase in which the filler is located, provides an opportunity to not only reduce the percolation threshold but also achieve a wider range of properties. However, the mechanism of nanoparticle-induced co-continuity is still an open discussion in the literature.

Wu et al investigated the effect of carbon black (CB) nanoparticles on the morphology of Acrylonitrile butadiene styrene(ABS)/ PA6 blends with droplet matrix morphology[32]. They observed that carbon black particles which are selectively located inside the PA6 dispersed phase were able to change the morphology from droplet-matrix to a co-continuous morphology. Additionally, during the annealing phase, the morphology evolved to a more perfect co-continuous morphology. They attributed this morphological change to self-networking ability of the nanoparticle. They argued that tendency of nanoparticles to form a 3-dimensional network drags the PA6 domains together leading to formation of co-continuous morphology (Fig. 2-5).

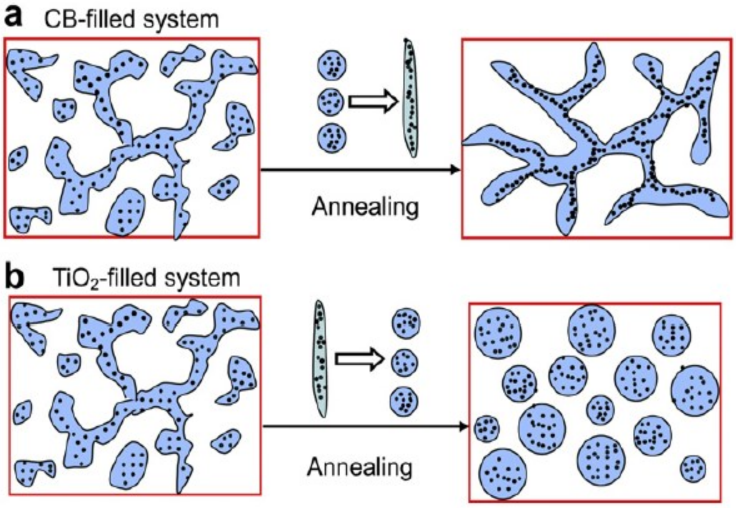

Figure 2-5. Evolution of morphology during annealing for immiscible blend containing a) CB, b) TiO2[33].

In another study, they investigate the impact of high surface energy TiO_2 nanoparticles which tend to aggregate on the phase morphology and its evolution during annealing[33]. Interestingly, they observed that TiO_2 particles cannot stabilize the morphology during annealing and the morphology formed during mixing, breaks up to discrete spherical droplets. Based on these observations, they concluded that beside the impact of nanoparticle on the rheological properties of component, networking ability of nanoparticle also plays an important role in the ability of nanoparticle to induce co-continuous morphology. Similarly, Xiu *et al* have reached to the same conclusion by investigating the impact of three CB nanoparticles with different networking ability[34]. They observed that CB nanoparticles with high networking ability induce a co-continuous morphology at significantly less content as compared to CB nanoparticle with low networking ability. However, in their review paper, Salzano *et al* argued that due to high viscosity of polymers in melt state and low thermal energy of nanoparticle, the idea that nanoparticle can drag the polymer domains together is questionable[35]. It is worth mentioning that in most studies, the presence of nanoparticles suppresses the coarsening of morphology during annealing due to the increased viscosity of the host phase[36].

Potschke *et al* has shown that bridging effect of nanoparticle can also stabilize the morphology during annealing[37]. They investigated the effect of CNT on the morphology of polycarbonate (PC)/ polyethylene (PE) blends with different compositions. They observed that the incorporation of CNT considerably broadens the range of compositions over which co-continuous morphology can be formed. Their morphological imaging revealed that due to high aspect ratio of CNT, they could bridge between the neighboring domains stabilizing the morphology (Fig. 2-6).

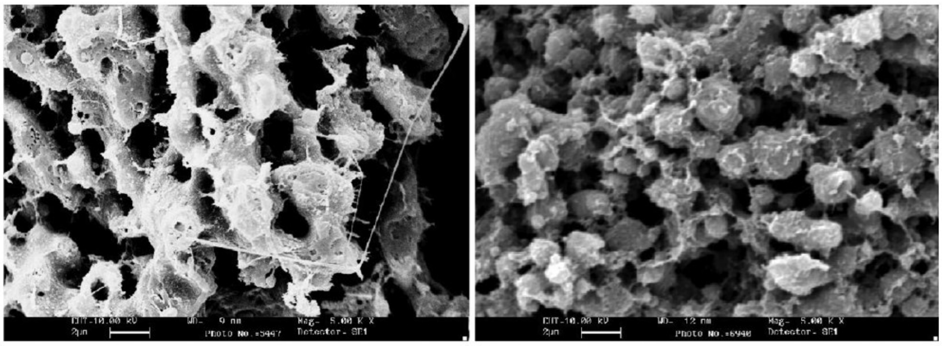

a) b)

Figure 2-6. SEM images of PC/PE a) 45/55, b) 80/20 blends containing 2% CNT. CNT particles bridge the neighboring domains. PE phase is extracted by the solvent[37].

Nuzzo *et al.* [26] studied the effect of nanoparticles with different geometry on induction of co-continuity in a blend with droplet-matrix morphology. They concluded that interfacially localized nanoparticles with higher stiffness, are more prone to induce co-continuity in a blend. They proposed a dimensionless group ($\alpha = \frac{\tau_y . P_c}{\sigma_{ij}^2}$) consisting of interfacial tension, σ_{ij}, which drives the deformed droplet towards a spherical shape, and factors that resist the relaxation of interface which are the yield stress of nanoparticle structure in the dispersed domain, τ_y, and the bending stiffness of the nanoparticles, P_c (Fig. 2-7).

However, these studies mainly focused on the stability of morphology during the annealing and they did not consider the effect of nanoparticle on evolution of morphology during mixing. In order for the dispersed phase to become continuous, the elongated domains should coalesce with one another. In the next section we will show that depending on the location of nanoparticles in the blend, the incorporation of nanoparticle may have different impact on the coalescence rate.

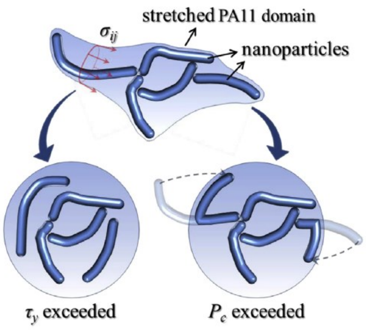

Figure 2-7. Schematic representing the relaxation of elongated domain to spherical shape[26].

2.3. Coalescence

Based on drainage theory, the coalescence process consists of 3 stages: (i) collision, (ii) drainage of film between two droplets, (iii) rupture [38].

The collision frequency of droplets during mixing depends on the number of droplets and the intensity of mixing. For randomly distributed spheres with the same size the number of collision per unit time per unit volume can be estimated by the following equation [20]:

$$\omega = \frac{8}{\pi}\dot{\gamma}\varphi \tag{2-3}$$

Where φ is the volume fraction of dispersed phase and $\dot{\gamma}$ is the shear rate. The collision time is the reciprocal of the number of collisions[39]:

$$t_{collision} = \frac{1}{\omega} = \frac{\pi}{8\dot{\gamma}\varphi} \tag{2-4}$$

When two droplets come sufficiently close, they start to interact with each other from a certain distance (h_o) leading to a reduction in the approach velocity. In order for droplets to coalesce with each other, the film between the droplets should be drained until a critical value ($h_{critical}$). At this distance, the van der Waals forces dominate, and rupture occurs. This critical distance can be estimated by the Eqn. 2-5[39] .

$$h_{critical} = \left(\frac{AR}{8\pi\sigma}\right)^{1/3} \tag{2-5}$$

Here, A is Hamaker constant and σ is interfacial tension. If the critical distance is not reached during the collision, the droplets will be convected away by the flow. The collision time in a simple shear flow is $t_{interaction} \sim \frac{1}{\dot{\gamma}}$.

The drainage time strongly depends on the interface rigidity and mobility[38]. For an unfilled blend, the rigidity of the interface depends on the viscosity ratio and interfacial tension[20]. As the viscosity ratio and interfacial tension between the components increases, the droplet behaves more like a rigid sphere. The presence of nanoparticles or surfactants at the interface can also increase the rigidity of the interface. This changes the drainage behavior [20]. Some important generalizations can be made [20]: (i) the higher the viscosity of the matrix phase, the longer the drainage time, (ii) smaller droplets are more prone to coalescence, (iii) the interfacial tension is only important in deformable interfaces, (iv) in the case of partially mobile interfaces, coalescence is more probable at low shear rate regions in the mixer where the contact force is smaller[20].

Here, we focus on the partially mobile interface which is mostly the case in polymer blends. In order to model the coalescence process, Chester assumed that the driving force for coalescence is constant, and the film formed between the deformed droplets is a flat disk with radius, a[38]. Since the pressure inside the film is in order of ($2\sigma/R$), the force, F, can be related to the geometry of deformed domain and interfacial tension (Fig. 2-8) by the following order of magnitude relation[38]:

$$F \sim \pi a^2 (\frac{2\sigma}{R}) \qquad (2\text{-}6)$$

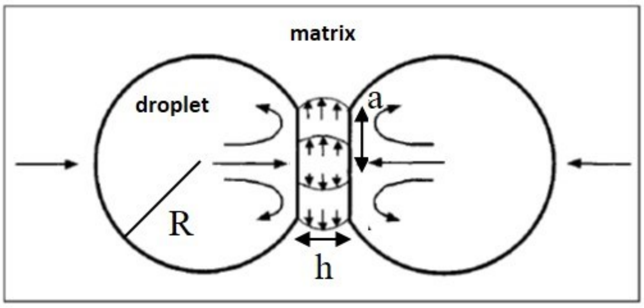

Figure 2-8. Schematic representing the simplified drainage process between two deformable droplets[40]. Figure is partially modified from reference.

Generally, the drainage rate is governed by the pressure gradient along the thin film, and the mobility of the interface. In the case of a partially mobile interface, the latter dominates the drainage rate.

Assuming that the length within which the velocity changes inside the droplets is comparable to the film radius, a, the stress at the surface, τ_d, then becomes:

$$\tau_d \sim 2\eta_d u_{int}/a \qquad (2\text{-}7)$$

Where u_{int} is the interface velocity which is assumed to be the film velocity. By applying the continuity equation, we have:

$$u_{int} = (\frac{r}{2h})(-\frac{dh}{dt}) \tag{2-8}$$

Here, r is the radial distance in the flat disk. Next, we need an expression for u_{int} to calculate the drainage rate$(-\frac{dh}{dt})$. Applying a force balance on an element of the film, we have[38]:

$$\tau_d = \left(\frac{h}{2}\right) \partial p/\partial r \tag{2-9}$$

Therefore, from Eqn. 2-7 we have

$$2\eta_d u_{int}/a \sim \left(\frac{h}{2}\right) \partial p/\partial r \tag{2-10}$$

And

$$u_{int} \sim \left(\frac{ha}{4\eta_d}\right) \partial p/\partial r \tag{2-11}$$

In order to derive *h(t)*, we substitute Eqn. 2-11 into Eqn. 2-8 giving

$$(\frac{r}{2h})(-\frac{dh}{dt}) \sim \left(\frac{ha}{4\eta_d}\right) \partial p/\partial r \tag{2-12}$$

This is integrated to give

$$\left(-\frac{dh}{dt}\right) \sim \left(\frac{h^2}{a\eta_d}\right) \Delta p \tag{2-13}$$

Since $\Delta p \sim (\frac{2\sigma}{R})$ and substituting for *a* in terms of *F* using Eqn. 2-6, we have

$$-\frac{dh}{dt} \sim \frac{2(\frac{2\pi\sigma}{R_0})^{3/2} h^2}{\pi\eta_d F^{1/2}} \tag{2-14}$$

Assuming that *F* is constant, Eqn. 2-14 integrates to:

$$t_{drain} \sim \frac{\pi\eta_d F^{1/2}}{2(\frac{2\pi\sigma}{R_0})^{3/2}} (\frac{1}{h_{crit}} - \frac{1}{h_0}) \tag{2-15}$$

In order to obtain the probability of coalescence, the time scale of the factors involved in the process should be compared. The collisions occurs only if the processing time is longer than collision time. In addition, this collision results in coalescence only if the collision time is longer than the coalescence time[39]. Accordingly, the total probability of coalescence can be calculated by the following equation:

$$P_{coalescene} = P_{collision} . P_{drainage} = exp\ (-\frac{t_{collision}}{t_{process}}) exp\ (-\frac{t_{drainage}}{t_{interaction}}) \tag{2-16}$$

In the case of a partially mobile interface (which is mostly the case in polymer blends), the probability of coalescence is:

$$P_{coalescene} = \exp\left(-\frac{\pi}{8\dot{\gamma}\varphi t_{\mathrm{process}}} - 0.077\mathrm{Ca}^{1.5}\left(\frac{R}{h_c}\right)\left(\frac{\eta_d}{\eta_m}\right)\right) \qquad (2\text{-}17)$$

This equation shows that the probability of coalescence decreases with increasing droplet size and viscosity ratio. Fig. 2-9 shows the probability of coalescence as a function of capillary number[39].

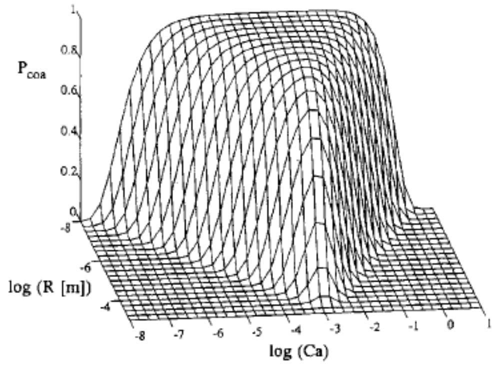

Figure 2-9. Coalescence probability as a function of radius and Capillary number for a partially mobile interface in simple shear[39].

At very low capillary numbers, coalescence cannot take place within the processing time (Fig. 2-9). At the middle range of capillary numbers, collisions lead to coalescence. However, at large capillary numbers the collision time becomes shorter than the drainage time and the coalescence probability decreases. Note that high shear rates lead to larger deformations of droplets increasing the radius of flattened area between the droplets (Eqn. 2-6) which increases the drainage time.

Eqn. 2-17 indicates that coalescence rate monotonically decreases with increasing viscosity ratio ($\frac{\eta_d}{\eta_m}$). However, experimental results have shown that viscosity ratio has a non-monotonic impact on the coalescence rate. Lyu *et al* showed that the coalescence rate becomes maximum at the viscosity ratio between 0.1-1 and decreases with a further increase in the viscosity ratio [40]. Lyu *et al* argued that at large viscosity ratios (($\frac{\eta_d}{\eta_m} > 1$) the "fountain flow" inside the droplet is weak (Fig. 2-8)[41]. Accordingly, the flow inside the droplet cannot facilitate the drainage process leading to long drainage times. On the other hand, at low viscosity ratios, the deformation of the droplet dominates the drainage process, i.e. large droplet deformation gives rise to an increase in area between the deformed droplets slowing down the drainage.

In the simple model discussed earlier, the force is constant during the collision which is only true in the case of head-on collision. It also neglects the impact of hydrodynamic interactions between the droplets. In a simple shear flow field, in the absence of hydrodynamic interactions, the streamlines will be straight. In this case collision occurs between a small droplet with diameter D_1, approaching a large droplet with diameter D_2 provided that the small droplet is located within the cylinder with diameter of D_1+D_2 (Fig. 2-10).

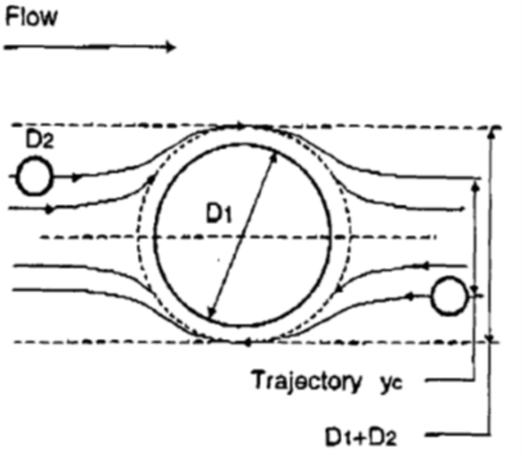

Figure 2-10. Trajectories for a small particle moving toward a large droplet[40].

However, in the presence of hydrodynamic interactions, the collision occurs only if the droplet is within a smaller cylinder with diameter of y_c. Otherwise, the small droplet will pass the big droplet decreasing the collision efficiency[40]. Accordingly, the hydrodynamic interactions not only alter the interaction force but also reduce the collision frequency especially at large diameter ratios. Wang *et al* calculated the probability of coalescence as a function of diameter ratio for different viscosity ratios of non-deformable spheres (Fig. 2-11) incorporating hydrodynamic interactions[42]. As shown in the figure, the probability of coalescence is maximum for droplets with the same diameter ($\lambda=1$) and decreases with increasing viscosity ratio. Clearly, this theory also fails to predict the non-monotonic impact of viscosity ratio on the coalescence rate observed by Lyu *et al*.

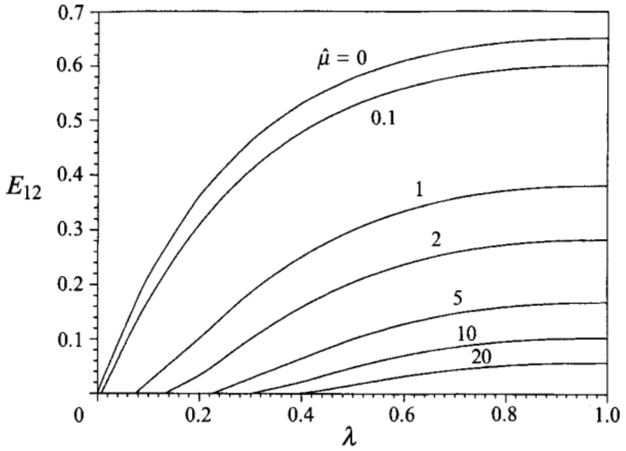

Figure 2-11. Coalescence probability (E_{12}) as a function of diameter ratio for different viscosity ratios in simple shear[42].

Mousa *et al* investigated experimentally the coalescence efficiency between two droplets in simple shear flow and compared their results with the prediction of the trajectory and drainage theories[43]. They observed a non-monotonic (decreasing-increasing) impact of "flow number" ($FI = 6\pi\eta_c R_{eqv}^3\dot{\gamma}/A$) on the coalescence efficiency which is not predicted by the theories. They attributed this behavior to the instabilities in the thin film which is not accounted for in the models.

Shardt *et al* simulated the coalescence of two droplet in simple shear flow with the focus on the evolution of thin film between the two droplets[44]. Their results show that at low capillary numbers there is only one minimum in the film thickness at the center of the film. However, at capillary numbers close to the critical capillary number, two minima form in the film thickness separated by a distance that increases with increasing capillary number[44]. This simulation shows that the evolution of shape of the film during coalescence is rather complex. Accordingly, the models assuming formation of flat disk between the domains cannot predict the coalescence process accurately.

Yoon *et al* studied the impact of viscosity ratio on the flow induced coalescence of two droplets with equal size in extensional flow experimentally using a four-roll mill (Fig. 2-12)[45]. This allowed them to investigate two types of collisions: (i) head on collisions, where the droplets are placed on the inflow axes and do not rotate during the coalescence process, and (ii) glancing collisions, where the droplets follow the stream lines and rotate relative to each other (Fig. 2-12).

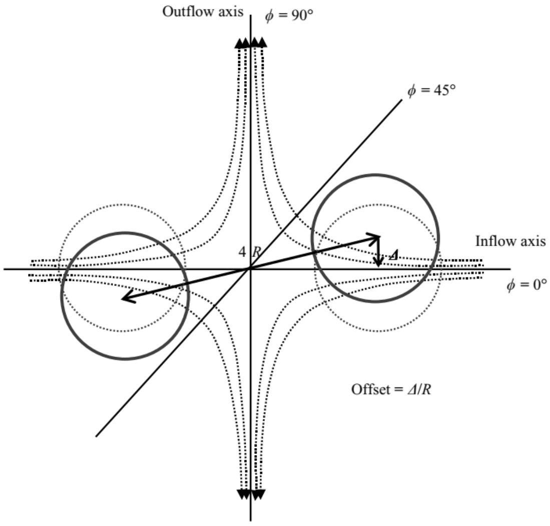

Figure 2-12. Schematic representing the flow produced by a four-roll mill[45].

Following the concept of Chester drainage theory (Eqns. 6 to 13), they model the coalescence process in the flow generated by the four roll mill considering hydrodynamic interactions[45]. They assume that the force is a function of the angle between the droplets and a weak function of viscosity ratio. In the case of head-on collisions, their experimental results were qualitatively in agreement with their “simple scaling model”[45].

However, in the case of glancing collision, they observed interesting results by changing the offset and viscosity ratio. As mentioned before, in their experiment the viscous force along the center-center line of the droplets is a function of angle (Fig. 2-12). At 45° the force changes sign from pushing the droplets together to separating the droplets. Accordingly, there is a finite time for the coalescence to occur. Interestingly, they observed that coalescence can also happen when the angle exceeds 45° (when the flow is separating the droplets) for droplets with viscosity ratio higher than p=0.19. They observed two possible ranges of coalescence angles; the coalescence either occurs as the droplets approach each other at low angles, or when the droplets are separating at higher angles[45]. They also attributed the coalescence at high angles to the evolution of film between the droplets.

In summary, it can be concluded that the evolution of the thin film between the droplets is the key point in understanding the coalescence and is far from being fully understood[46].

2.3.1. Effect of nanoparticles on coalescence

Generally, studies have shown that the presence of nanoparticles in the matrix decreases the coalescence rate of droplets. This is due to an increase in the viscosity of matrix which subsequently increases the drainage time. This effect is more pronounced when the content of nanoparticles exceeds the percolation threshold and nanoparticles form a 3-dimensional structure in the matrix[24].

The presence of nanoparticles at the interface can have different impact on the coalescence.

Vandebril *et al*. used rheological analysis to clarify the effect of interfacially localized nanoparticle on the coalescence rate of polyisobutylene (PIB)/ polydimethylsiloxane (PDMS) blends [47]. They presheared the blends at a high shear rate (higher than the critical capillary number) where the blend morphology is controlled by the break up/ coalescence equilibrium. Then, the shear rate was reduced below the critical shear rate to monitor the effect of coalescence on rheological behavior. They calculated the R_v/σ using the relaxation time of droplet calculated by the Palierne model[48]. Using R_v/σ allowed them to avoid uncertainty concerning the effect of nanoparticles on interfacial tension. As shown in Fig. 2-13a, with increasing the particle content, the coalescence rate decreases and it is completely suppressed for the blend containing 0.45vol% nanoparticle. They argued that the effect of nanoparticle on interface rigidity is responsible for this reduction in coalescence.

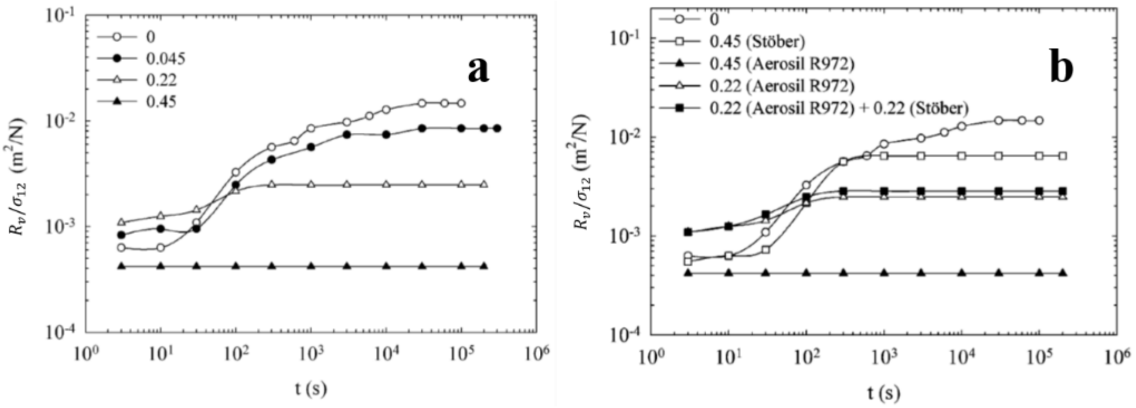

Figure 2-13. Development of R_v/σ as a function of shearing time. A) for droplet-matrix morphology containing different content of Aerosil R972, and b) for droplet-matrix morphology containing nanoparticle with different aggregate size [47]. Figure is partially modified from reference.

The authors also studied the effect of interfacial coverage on coalescence by using two nanoparticles with different aggregate sizes (Aerosil R972, Raggr =101 nm, Stober, Raggr =495 nm). Their results illustrate that the nanoparticles with the larger aggregate (lower interfacial coverage) cause considerably less reduction of coalescence in comparison to nanoparticles with high interfacial coverage. Interestingly, in the case of the blend containing both types of nanoparticles, the overall coalescence process is controlled by the Aerosil particle with smaller aggregates.

Thareja *et al.* reported that interfacially localized nanoparticles can either hinder or promote coalescence depending on whether they are preferentially wetted by the matrix or by the dispersed phase [49, 50]. In the case where the nanoparticles are preferentially wetted by the matrix phase θ<90 (Fig. 2-14), the nanoparticle can be absorbed by two neighboring droplets. In this situation nanoparticles can bridge between two droplets stabilizing the film between droplets (Fig. 2-14b). Consequently, droplets cannot coalescence nor be separated. In other words, the droplets connect together resulting in the formation of droplet clusters (Figure 16c).

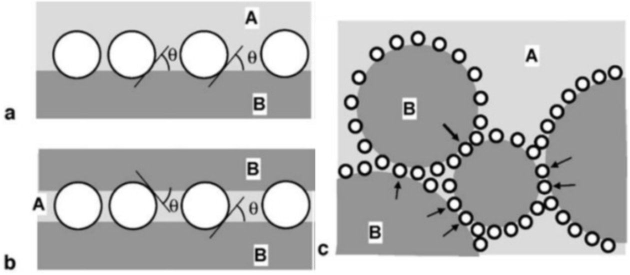

Figure 2-14. a) Nanoparticle at the interface which is preferentially wetted by component A, b) bridging of nanoparticle between two neighboring droplet. c) formation of non-coalescing droplet clusters[49].

However, if the nanoparticles are preferentially wetted by the dispersed phase, they can promote coalescence through the bridging-dewetting mechanism (Fig. 2-15)[50]. In this situation, when two droplets collide with each other, nanoparticles bridge these droplets (Fig. 2-15b). This situation is not thermodynamically favorable since the contact line exceeds the equilibrium angle. Consequently, the matrix phase dewets the nanoparticle leading to rupture of the film between the approaching domains and coalescence (Fig. 2-15 c-d).

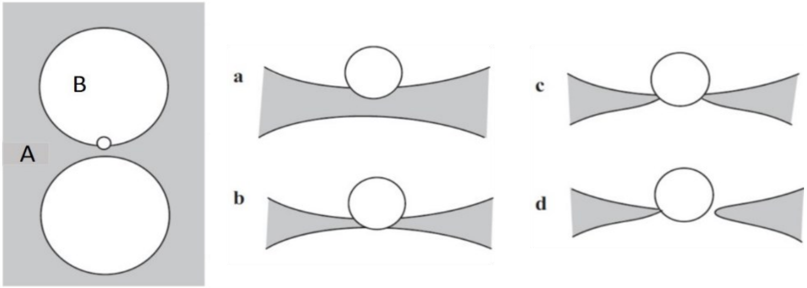

Figure 2-15. Schematic indicating the bridging dewetting mechanism[50].

It is noteworthy to mention that droplet clustering has been also observed when the interfacially localized nanoparticle is preferentially wetted by the minor phase [35, 51, 52]. In this case, droplet clustering is attributed to the enhanced van der Waals forces between the nanoparticle coated domains[52, 53].

2.4. Effect of nanoparticles on final morphology

The impact of nanoparticles on coalescence and break up has been discussed separately in some detail. To have a better picture regarding the effect of nanoparticle on the final morphology, in this section we review studies which highlights the influence of nanoparticle on the final phase morphology. Fenouilot *et al* have proposed four different mechanism by which nanoparticle can affect the morphology of polymer binary blends[24].

(i) Changing the interfacial tension,
(ii) Reducing droplet coalescence with the formation of a physical barrier around the minor phase domains,
(iii) Changing the viscosity arising from the selective localization of nanoparticle in one phase,
(iv) Formation of a nanoparticle 3D network reducing the mobility of dispersed phase,
(v) Steric hindrance effect of polymer chains adsorbing on the nanoparticle surface at the interface,

It is worth mentioning that these factors can simultaneously affect the phase morphology and usually it is not possible to separate out the individual effect. Next, we will explain these factors separately. The references are combination of studies reviewed by Fenouilot *et al* [24] and some other selected studies.

Elias *et al*. studied the effect of fumed silica with different surface chemistry on the ethylene-vinyl acetate (EVA) / polypropylene (PP) blend with droplet matrix morphology. They observed a reduction in droplet size with incorporation of nanoparticles regardless of nanoparticle surface chemistry[54]. They showed that nanoparticles significantly reduce the interfacial tension between EVA and PP from 0.75 to 0.25 mN/m [54] which is claimed to be the main reason behind the reduction of droplet size in their study. Si *et al*, investigated the effect of clay platelets on the morphology of different immiscible binary blends[28]. Their results revealed that localization of clay platelets at the interface leads to a refinement in the morphology. Interestingly, the incorporation of nanoparticle shifts the glass transition temperature of the components toward each other and at high content of clay (10%), they observed only one glass transition temperature. This shows that interfacially localized clay platelets were able to enhance the compatibility of the components. From these results it can be concluded that nanoparticles at the interface can decrease the interfacial tension between the components which may facilitate the break up process[55]. Nevertheless, it should be pointed out that the break up process also depends on the impact of nanoparticles on the elasticity of the host phase. At high nanoparticle loading, the deformability of the host phase reduces significantly.

Hong *et al* investigated the effect of clay on the morphology of polybutadiene terephthalate (PBT)/ PE. They observed a reduction in droplet size at low content of clay [56]. In blends containing low content of clay where the viscosity of host phase did not change significantly, they attributed the reduction of droplet size to the formation of a physical barrier around the droplet preventing the coalescence. Accordingly, interfacially localized nanoparticles not only reduce the interfacial tension but also prevent the coalescence rate. Both of these effects lead to refinement in the phase morphology.

As it was discussed earlier, the break up behavior of minor phase droplets is governed by the capillary number and viscosity ratio. To explain the impact of viscosity ratio on the morphology we can again refer to the study by Hong *et al* [56]. In the case of nanocomposites containing high content of clay, they observed an increase in the droplet size. This is attributed to increased viscosity of the dispersed phase due to the presence of nanoparticle inside this component. This increases the viscosity ratio subsequently suppressing the breakup.

Finally, Fenouillot et al argued that the polymer chains absorbed on the surface of nanoparticles can prevent coalescence by steric hindrance when the nanoparticle is localized at the interface. This is similar to the effect of block copolymers which form a shell around the dispersed phase and suppresses the coalescence [24]. This mechanism is only expected to be effective when both phases have strong interactions with the nanoparticle.

Clearly, the localization of nanoparticle has a determining effect on the morphology. In the next section, we discuss the migration of nanoparticles and factors affecting the localization of nanoparticles in binary blends.

2.5. Migration and localization of nanoparticle

Generally, nanoparticles tend to be localized where they reduce the free energy of the system determined by the interaction of the nanoparticles with each constituent. The particle location in the equilibrium state can be predicted by the wetting parameter defined as [57]:

$$\omega = \frac{\gamma_{P/A} - \gamma_{P/B}}{\gamma_{A/B}} \tag{2-18}$$

Here, $\gamma_{P/A}$ is interfacial tension between the particle and polymer A, $\gamma_{P/B}$ is interfacial tension between the particle and polymer B and $\gamma_{A/B}$ is the interfacial tension between the polymer phases. Table. 2-1 summarizes the predicted location of nanoparticle based on the wetting parameter.

Table 2-1. Prediction of nanoparticle localization at thermodynamic equilibrium based on the wetting parameter.

ω	Predicted location
$\omega > 1$	Component B
$\omega < -1$	Component A
$-1 < \omega < 1$	Interface

The interfacial tension between the component pairs can be calculated by the geometric mean and harmonic mean equations[58, 59]:

$$\gamma_{1/2} = \gamma_1 + \gamma_2 - 2\left(\sqrt{\gamma_1^d \gamma_2^d} + \sqrt{\gamma_1^p \gamma_2^p}\right) \tag{2-19}$$

$$\gamma_{1/2} = \gamma_1 + \gamma_2 - 4\left(\frac{\gamma_1^d \gamma_2^d}{\gamma_1^d + \gamma_2^d} + \frac{\gamma_1^p \gamma_2^p}{\gamma_1^p + \gamma_2^p}\right) \tag{2-20}$$

Here γ_i is the surface energy of component i and γ_i^d and γ_i^p are the dispersive and polar contributions to the surface energy, respectively.

The migration of nanoparticles during mixing occurs via the collision of nanoparticles with the interface of components due to mechanical forces[60]. If the nanoparticle has a better compatibility with the other component the primary chains absorbed on the nanoparticle will be replaced by the more favorable component and the nanoparticle will pass through the interface. Jalali *et al.* proposed 3 stages in nanoparticle migration (Fig. 2-16): (i) bulk migration, (ii) film drainage, (iii) migration through interface[61]. The bulk migration and film drainage processes are roughly similar to the coalescence process. However, the authors mentioned that bulk migration is not the determining step in overall migration rate.

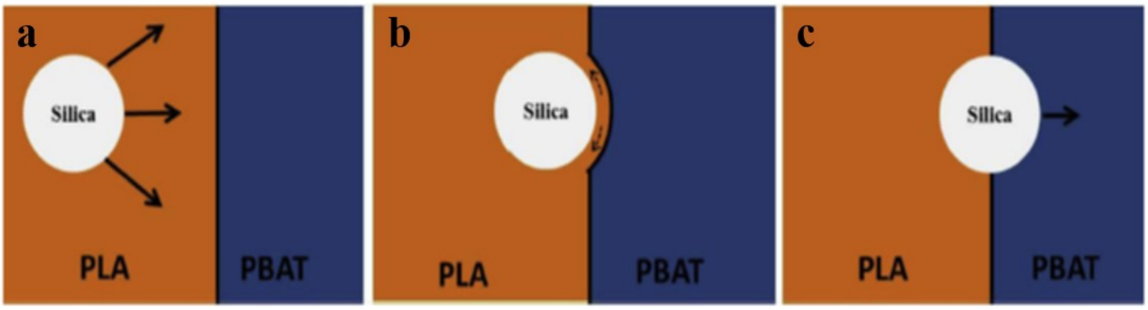

Figure 2-16. Schematic representing migration of silica nanoparticle, a)bulk migration, b) film drainage, c) migration through interface[61].

The drainage time of a film between a spherical nanoparticle and a deformable interface is $t_d \sim \frac{A^2.\eta}{F}$ [62]. Here, A is the surface area of film between nanoparticle and interface, η is the viscosity of host phase and F is the contact force. Both the viscosity of the host phase and the radius of nanoparticle increase the drainage time giving rise to a decreases in the overall migration rate. Similarly, the aggregation of nanoparticles can significantly increase the film surface area resulting in a reduction of migration rate.

Regarding migration through the interface, Jalali *et al* argued that in order for the nanoparticle to migrate through the interface it should displace the three-phase contact line of nanoparticle with the interface[62]. The energy for displacements comes from the thermodynamic affinity of nanoparticles toward the more favorable phase and mechanical forces applied on the nanoparticle surface. However, for the sake of simplicity, they only considered the thermodynamic factors at quiescent conditions. In this case, the migration rate of a nanoparticle through the interface is governed by the affinity of the nanoparticle with each component, the interfacial tension between the components and their viscosity.

Göldel *et al.* studied the migration behavior through the interface from another standpoint. Their observations revealed that nanoparticles with a high aspect ratio can effectively migrate to the more thermodynamically favorable component while spherical nanoparticles remain trapped at the interface[63]. The authors argued that the interface curvature instability is the driving force for the migration of nanoparticles from one phase to another. A higher curvature instability is expected in the case of a high aspect ratio nanoparticle perpendicular to the interface (Fig. 2-17). Therefore, for nanoparticles with high aspect ratio, the migration rate through the interface is strongly dependent on orientation of nanoparticle with respect to the interface. It is worth mentioning that this orientation also has a direct impact on the drainage time affecting the time required for nanoparticle to reach the interface.

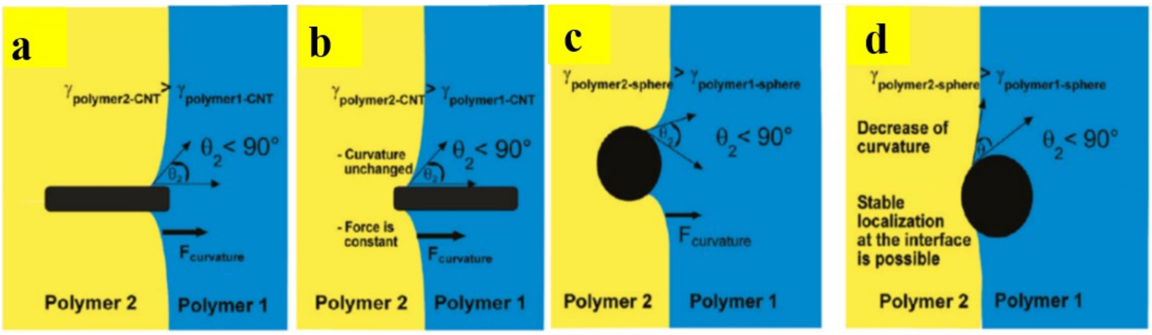

Figure 2-17. Migration of nanoparticle through interface with different geometries; a and b) high aspect ratio particle perpendicular to the interface, c and d) spherical particle[63].

Such behavior was reported by Bai *et al* in the case of graphene nanoparticles where the migration rate of graphene was controlled by the three-phase contact line[64]. Their calculation predicted that the migration rate of graphene perpendicular to the interface is 1000 times larger than that of particles in a parallel orientation. In their mixing experiments, graphene initially parallel to the interface remained at the interface over ten minutes, while any particles tilted relative to the interface migrated to the more thermodynamically favorable component.

Plattier *et al* explained the migration of nanoparticle across the interface by looking at the drag forces applied on the nanoparticle when they are at the interface. They found that when changing the molecular weight of the phases, carbon black (CB) particles localized in the phase with the higher viscosity[65]. When the viscosity of the two phases were similar, the CB particles were localized at the interface. They explained the final localization in terms of the balance between drag forces applied on the nanoparticle by each component. The drag forces is a function of viscosity of component and the surface area of nanoparticle in contact with the component which is controlled by the equilibrium contact angle (Fig. 2-18).

$$\frac{F_d}{F_m} = \frac{(1+cos\theta)}{(1-cos\theta)}\frac{\eta_d}{\eta_m} \qquad (2\text{-}21)$$

When the nanoparticle is at the interface, drag forces applied during mixing, extract the particle toward the component with higher viscosity. Nevertheless, their analysis are only based on the drag force and they did not consider the effect of normal forces induced by the viscoelastic nature of polymers.

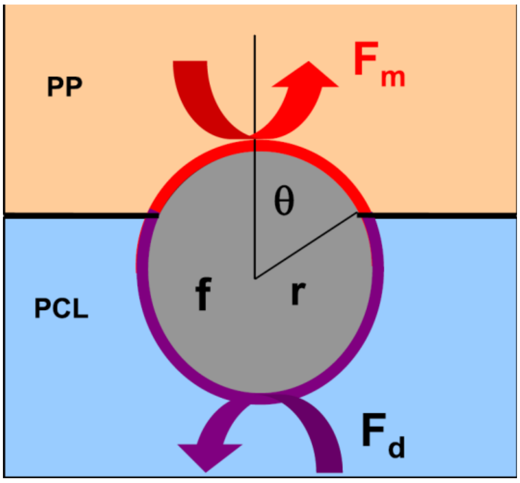

Figure 2-18. Drag forces applied on the nanoparticle at the interface[65].

The opposite behavior with CB was observed in different blend systems[66, 67]. For example, Feng *et al* studied the effect of viscosity ratio of components in a PP /Poly methyl methacrylate (PMMA) with a droplet matrix morphology[66]. Their morphological observation revealed that when the viscosity ratio was close to unity CB nanoparticles were localized inside the PMMA droplets which was in line with the prediction of wetting parameter (Fig. 2-19 a). However, with increasing PMMA viscosity, CB particles move from the PMMA phase to the interface and then the PP phase (Fig. 2-19b and c). These contradictory results show that the impact of rheological properties of components on the migration and final localization of nanoparticle is not fully understood.

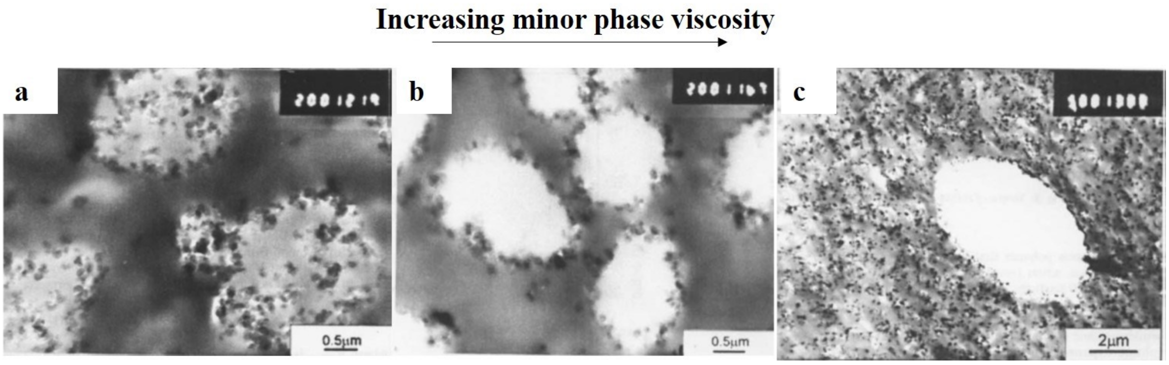

Figure 2-19. The localization of CB nanoparticle in PP/ PMMA immiscible blend with increasing the viscosity of PMMA (minor phase). The PMMA is bright phase[66].

Recently, Jaensson *et al* simulated the migration of a spherical nanoparticle at the vicinity of the interface between a viscoelastic fluid and a Newtonian fluid[68]. Their simulation demonstrated that due to the normal force built up in the viscoelastic fluid, the nanoparticle can migrate across the streamline (Fig. 2-20) indicating that the normal force can also play a role in migration of nanoparticle. They observed different migration behavior depending on the viscoelastic properties of fluid.

When the host phase was Newtonian, due to the Laplace pressure arising from the deformation of the interface, the nanoparticle moved further away from the interface (Fig.2-20a). With increasing the viscoelasticity of the material, indicated by Weissenberg number Wi= $\lambda\dot{\gamma}$ =1 where λ is the relaxation time of the polymer and $\dot{\gamma}$ is the shear rate, the normal force pushed the nanoparticle toward the interface. However, at low Wi=1, the normal force cannot overcome the Laplace pressure and the migration of nanoparticles is halted below the interface (Fig. 2-20b). At higher Weissenberg number (Wi=2) the normal force exceeds the Laplace pressure, and the nanoparticle migrates across the interface (Fig. 2-20c). Interestingly, with further increasing the Wi=3, the nanoparticle adsorbed at the interface. The authors attributed this to the shear thinning behavior of the viscoelastic material at high Wi decreasing the angular velocity of nanoparticle. They argued that angular velocity of nanoparticle facilitates the migration of nanoparticle across the interface by spinning off the interface. Accordingly, the decrease in the angular velocity hinders the migration through the interface. These results show that besides viscosity, the elasticity of components can also play a role in the migration of nanoparticles.

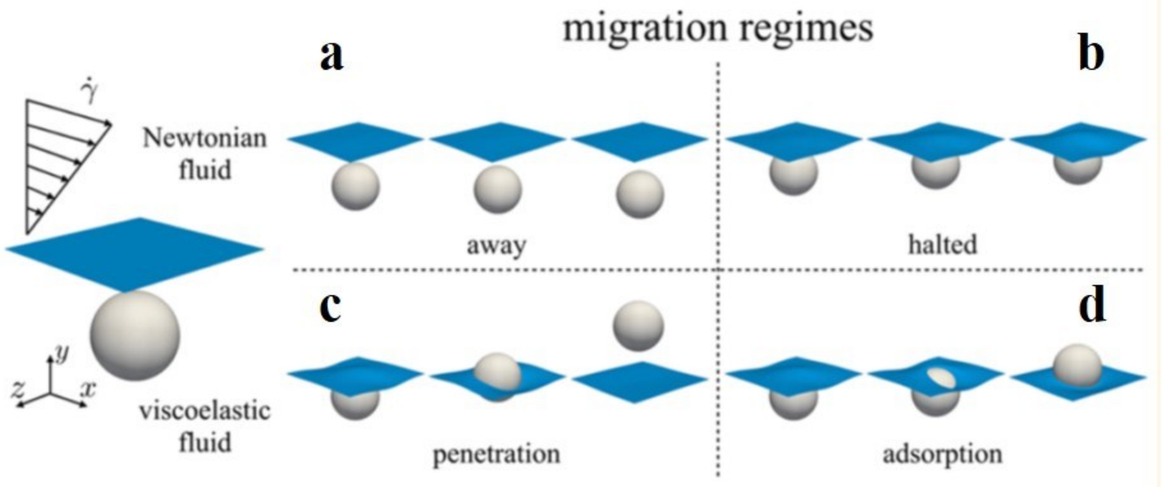

Figure 2-20. Schematic representing the migration of spherical nanoparticle across the stream line in simple shear. The nanoparticle is initially inside the viscoelastic phase[68].

2.6. Effect of morphology and nanoparticle localization on electrical properties

As discussed, the phase morphology is affected by the localization of nanoparticle in the blend. In this section we review studies which explore the relation between microstructure, localization of nanoparticle and electrical properties. We start with binary nanocomposites (polymer matrix and nanoparticles) and then blends containing nanoparticles will be discussed.

Kim *et al* investigated the influence of graphene dispersion in polyethylene (PE) matrix on the electrical conductivity by employing different mixing strategies and compatibilizers [8]. In the case of the uncompatibilized system, prepared by melt mixing, they observed poor dispersion of graphene with almost no change in electrical conductivity. However, in the case of nanocomposites prepared by solvent mixing, they observed a significant increase in electrical conductivity. Interestingly, their results showed that the "un-functionalized" system prepared by solvent mixing had a higher electrical conductivity compared to the functionalized PE which has a higher degree of exfoliation. They attributed the increase in electrical conductivity to the formation of a phase-separated morphology in which graphene-rich phase forms a continuous structure throughout the nanocomposites. Accordingly, they concluded that a good dispersion of nanoparticles does not always lead to higher electrical conductivity and the distribution of nanoparticle aggregates is also important.

Gubbles *et al* investigated the effect of CB nanoparticles on the electrical properties of PS/PE blends in a series of studies [13, 14, 69]. They observed that the electrical percolation threshold for the PE/CB nanocomposite is lower than that of the PS/CB nanocomposite. They attributed this difference to the dispersion state of CB in these blends. CB nanoparticles were better dispersed in PE due to the crystallinity of PE. The crystallization of the host phase alters the arrangement of nanoparticles facilitating their percolation. Strugova *et al* investigated the impact of cooling conditions on the electrical conductivity of PP/PS/MWCNT where the nanoparticles were localized inside the PP phase. They showed that a slow cooling rate, which allows complete crystallization of PP, results in a significant reduction in the electrical percolation threshold attributed to the volume exclusion of crystals[70].

In the next step, Gubbles *et al* demonstrated that it is possible to decrease the electrical percolation by taking benefit of the double percolation concept in PS/PE blend with a co-continuous morphology and selective dispersion of CB nanoparticle in the PE phase. Finally, they showed that the percolation threshold can be minimized with localization of the nanoparticles at the blend interface. They premixed the CB nanoparticle with PS (less favorable component) and then added with PE phase. They observed that electrical conductivity of their system increases with mixing time and goes through a maximum before decreasing at longer mixing times[69]. This maximum is the mixing time at which the nanoparticles are mostly at the interface (Fig. 2-21, plotted in terms of resistivity).

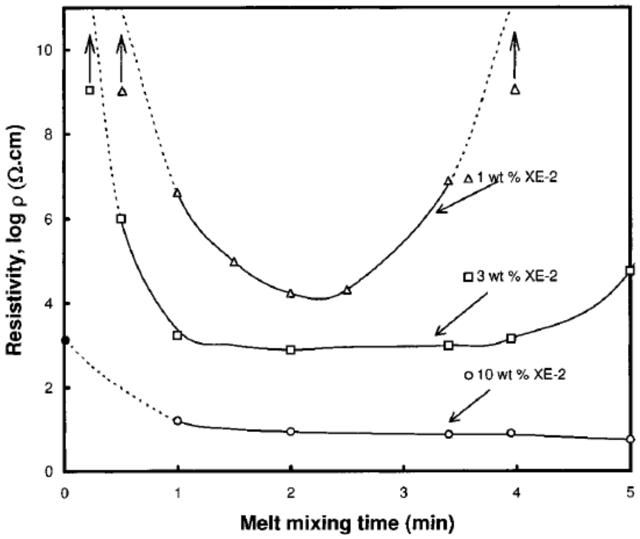

Figure 2-21. Resistivity as a function of mixing time for PS/PE (55/45) nanocomposites containing different content of CB[69].

Zaikin *et al* observed similar results in a PP/PS blend with a co-continuous morphology[71]. In this system, CB nanoparticles have the thermodynamic tendency to be localized at the interface and they observed an increase in the electrical conductivity with a plateau at long mixing times. This is consistent with the localization of nanoparticles at the interface.

Dharaiya *et al* investigated the effect of morphological evolution and migration of CB nanoparticles during the mixing of PA6/PP/CB (90/10/1) nanocomposites[72]. First, they premixed the CB nanoparticles with the PP phase to prepare a master batch. In the next step they melt blended the resultant master batch with PA in a cylindrical rotor, internal mixer. This internal mixer allowed them to calculate the cylindrical angular displacement and total deformation during mixing. Their morphological imaging at different mixing times revealed that at the early stage of mixing, the PP phase deforms and forms elongated domains, leading to formation of co-continuous morphology and a double percolated structure. Then at longer times, these elongated domains break up, leading to a loss of co-continuity and thus a decrease in electrical conductivity (Fig. 2-22 point D). At even longer mixing times, the electrical conductivity increases again with the migration of nanoparticles toward the interface and the formation of smaller droplets (Point F). Finally, complete migration of nanoparticles to the PA matrix phase leads to a decrease in electrical conductivity (Fig. 2-22 point G). These results highlight the important roles of nanoparticle localization and phase morphology on the electrical conductivity.

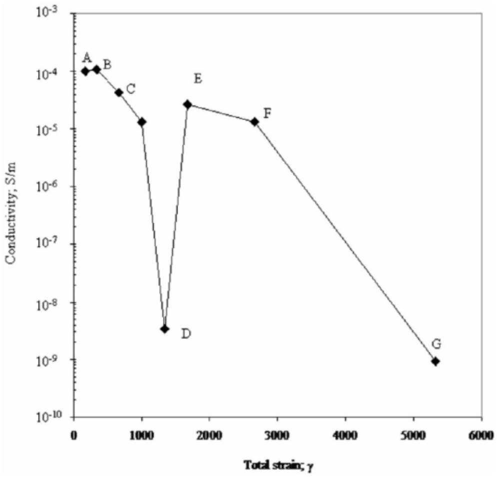

Figure 2-22. Electrical conductivity as a function of total strain during mixing for PA6/PP containing 1% CB[72].

A similar relation between the nanoparticle localization and electrical conductivity has been observed in the case of nanocomposites containing CNT and graphene. For instance, Shi *et al* investigated the impact of mixing sequences on the electrical conductivity of PLA/ polyvinyl acetate (PVA) blends containing CNT[73]. They showed that premixing the CNT with PLA leads to the migration of CNT from the PLA phase toward the PVA phase. Accordingly, it is possible to trap the nanoparticles at the interface with this mixing sequence which leads to lower electrical resistivity (Fig. 2-23).

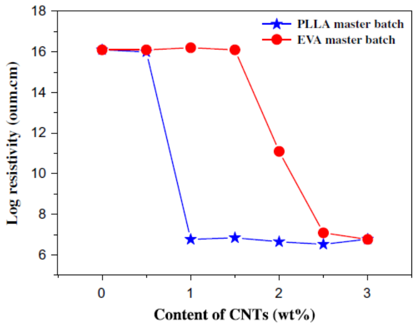

Figure 2-23. Electrical resistivity as a function of CNT content for PLLA/EVA nanocomposites prepared by different mixing orders[73].

Bai *et al* studied the effect of mixing time and migration of graphene platelets on the morphology and electrical conductivity of PLA/PS blend with a co-continuous morphology[64]. They prepared the nanocomposites with a PLA/graphene master batch. Due to greater thermodynamic affinity of graphene with PS, they migrated toward the PS phase during mixing. They track the morphology after 30 seconds, 5 minutes and 10 minutes of mixing. They observed that more interfacial area is covered with graphene at 30 seconds of mixing, leading to higher electrical conductivity.

The same authors also investigated the effect of graphene on the phase morphology and electrical conductivity of a PLA/PS blend with co-continuous morphology during annealing[3]. Similar to their previous study, they showed that graphene platelets migrate toward the interface when they premix the graphene with PLA. They showed that the migration can also occur during the annealing for graphene platelets close to the interface, stabilizing the morphology. The migration of nanoparticles and the formation of a percolated structure of graphene resulted in an increase in the storage modulus and electrical conductivity during annealing (Fig. 2-24).

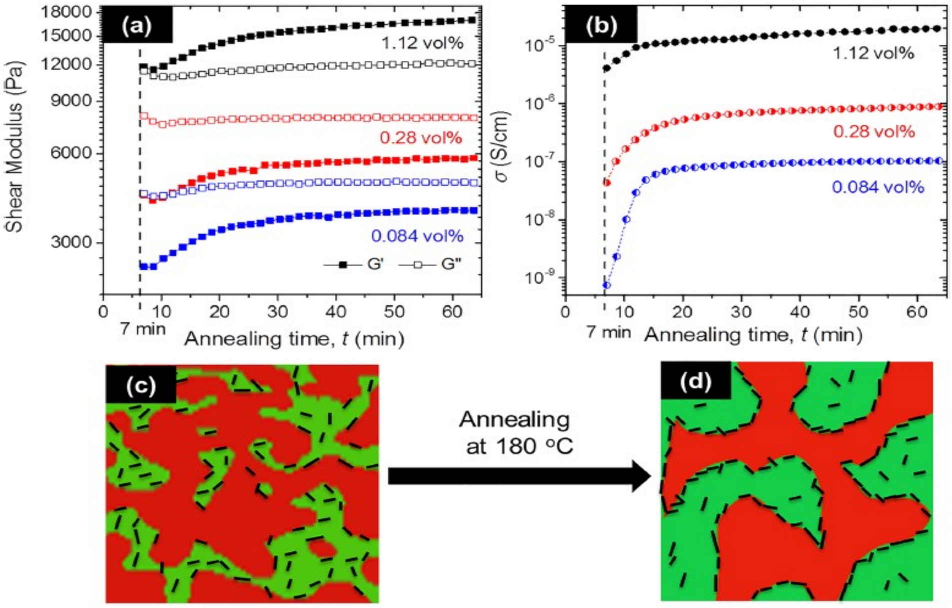

Figure 2-24. Evolution of a) storage modulus (solid symbols) and loss modulus (open symbols) symbols, b) electrical conductivity, c and d) microstructure during annealing[3].

Their results showed that electrical conductivity decreases with decreasing interface length (increasing characteristic domain size, Fig. 2-25a). Assuming that only interfacially localized particles contribute to the electrical conductivity (Fig. 2-25b-d), they were able to propose a model relating the interfacial area (characteristic length) to the electrical conductivity. These results show that there is a close relationship between the microstructure and electrical properties.

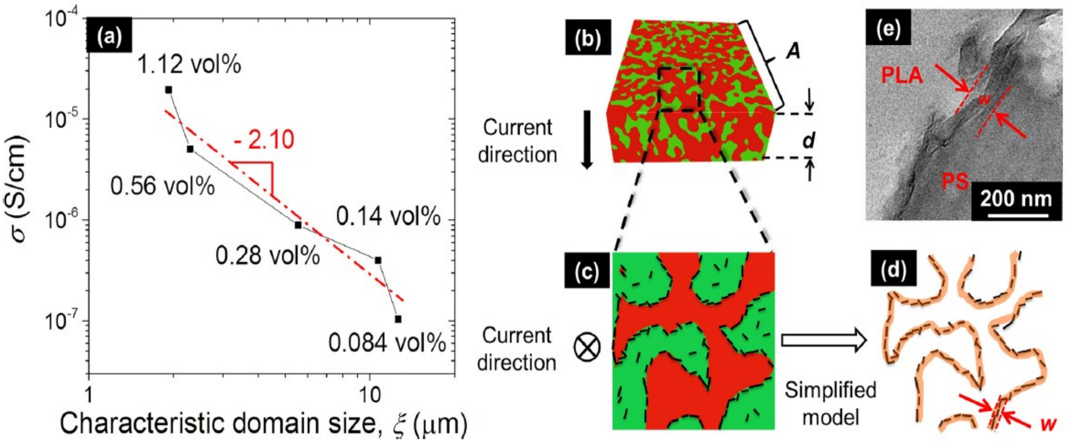

Figure 2-25. a) relationship between the electrical conductivity and characteristic length for PLA/ PS blend containing graphene with co-continuous morphology. b and c) schematic representing the sample with co-continuous morphology in vertical electric field, d) interfacially localized graphene which contribute to the electrical conductivity, e) TEM image indicating the effective interfacial region of width w[3].

Mun *et al* investigated the relationship between the microstructure and electrical conductivity of PE/PLA and PE/PP blends with co-continuous morphology prepared via different mixing sequences[74]. Changing the mixing order led to different graphene localizations and morphologies. They showed that an optimum electrical conductivity is achievable when the graphene particles can completely cover the interface at the smallest interfacial area. Again, these results highlight the relation between the phase morphology and final electrical properties.

As discussed before, another strategy to reduce the percolation threshold is inducing a co-continuous morphology at lower host phase content. Gao *et al* demonstrated that the localization of nanoparticles inside the dispersed phase changes the morphology droplet matrix morphology of poly(l-lactide) (PLLA)/poly(3-hydroxybutyrate-co-4-hydroxybutyrate) (P(3HB-co-4HB)) (80/20) to a co-continuous morphology (Fig. 2-26). This gives rise to a low electrical percolation threshold along with improved mechanical properties [75].

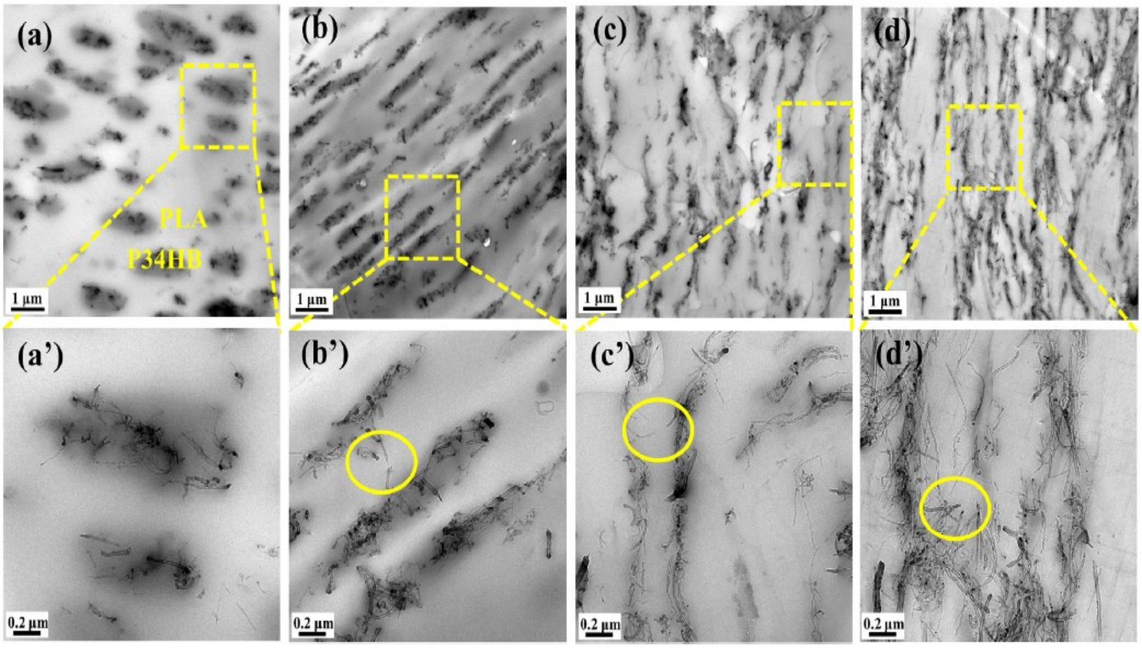

Figure 2-26. TEM images of PLA/P(3HB-co-4HB) (80/20) nanocomposites containing, a)0.5%wt, b)1%wt, c)2%wt, d)4%wt CNT[75].

Gao *et al* employed another method to manipulate the morphology and achieve fibrils with a low electrical percolation threshold[76]. They used hot stretching after extruding the components in an extruder with a slit die. First, they coated the PE phase with CNT nanoparticles and they melt mixed the CNT- coated PE particles with polycarbonate in the extruder. Due to greater thermodynamic affinity of CNT toward PC, they migrate from PE toward the interface. With this strategy, they were able to localize the CNT nanoparticles at the interface and then fibrils formed after stretching the blend in the melt state, achieving very low electrical percolation. The scheme of this process is shown in Fig. 2-27. Due to the anisotropic morphology, at high stretching ratio, the electrical conductivity along the stretch direction was roughly three times higher than that of perpendicular direction.

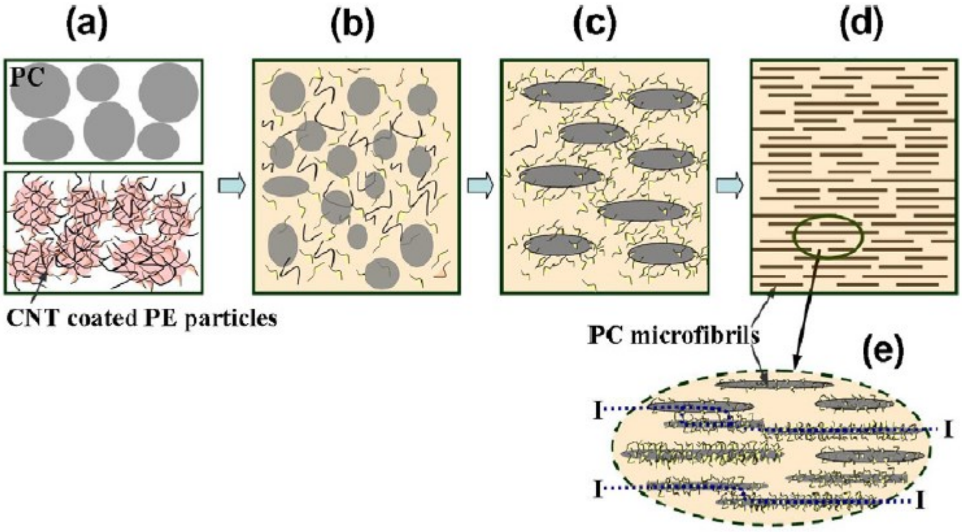

Figure 2-27. Schematic representing the formation of fibrillar morphology in PE/PC nanocomposites containing CNT. a) CNT coated PE particle, b) formation of PC droplets in PE matrix, c) migration of CNT from PE to interface, d and e) formation of PC microfibrils in PE[76].

These studies show that by employing a proper strategy for processing, including mixing sequence and time, it is possible to manipulate the morphology and nanoparticle localization to achieve desirable properties. In blends with a co-continuous morphology, the localization of nanoparticles at the interface can lead to an ultra-low electrical percolation threshold provided that nanoparticles completely cover the interface. In blends with droplet matrix morphology, depending on the localization of nanoparticles, they can induce different morphologies. They can cause refinement and produce smaller droplets or they can cause coarsening or even induce a co-continuous morphology. The induction of a co-continuous morphology occurs via the formation of elongated domains. The elongated domains can be formed during mixing by manipulating the viscosity and elasticity of dispersed phase, or they can be formed by stretching the dispersed domains after mixing. The formation of a co-continuous morphology at a minor phase content, leads to a significant decrease in the electrical percolation threshold.

As discussed, various factors play a role in the final phase morphology and properties of polymer blend nanocomposites including a complex dependency on processing. Understanding the relation between the nanoparticle network structure, phase morphology and final properties is crucial in designing new materials. This is far from being fully understood. Generally, microstructure and phase morphology are not stable and evolve when the temperature exceeds the melting temperatures of the blend components. Accordingly, besides the mixing step, post processing steps such as molding and annealing play important roles in the final properties particularly in the electrical properties. This aspect of the manufacturing of nanocomposites is less explored.

In the first part of this study, we highlight the role of graphene localization on the phase morphology, mechanical and electrical properties. Next, we focus on the evolution of microstructure and electrical properties during annealing. Rheological characterization allowed us to demonstrate the impact of nanoparticle assembly after compression on the microstructure and morphology. Finally, we show that there is a close relationship between the structural characteristics of the nanoparticle 3D network and the phase morphology.

3. Manipulating the morphology of PA6/POE blends using graphene to achieve balanced electrical and mechanical properties

3.1. Abstract

We investigate the effect of graphene localization on the morphology and properties of Polyamide 6 (PA6)/Polyolefin elastomer (POE) blends. Two systems with different compositions were studied: (i) 60/40 by weight (a composition near phase inversion) and (ii) 80/20 by weight (a highly asymmetric composition). In this study, we demonstrate that the migration behavior of graphene is strongly dependent on its dispersion state, which is determined by mixing order. We show that the neat 60/40 (PA6/POE) blend has an unstable co-continuous morphology which breaks up over time during annealing to a droplet-matrix morphology with POE being the continuous phase. The addition of 3wt% graphene leads to co-continuous morphologies independent of mixing order. In the case of 80/20 systems, preparation of nanocomposites with a POE master batch resulted in elongated POE dispersed domains which becomes a co-continuous morphology at higher level of graphene content. However, we observed a decrease in the continuity of the POE phase in the nanocomposite containing 3%wt of graphene due to a reduction of coalescence. Our rheological and electrical measurements revealed that the graphene formed a stronger percolated structure in 80/20 blend containing 3wt% of graphene in comparison to 60/40/3 nanocomposites, which resulted in lower electrical resistivity. The electrical percolation threshold in this system is 0.66wt% which demonstrates that using graphene to induce co-continuity in a highly asymmetric composition is a promising approach to design electrically conductive blends with a very low percolation threshold.

3.2. Introduction

Polymer blends are often produced in order to create materials with properties that neither of the constituents alone exhibit. In most cases, molten polymers are immiscible resulting in a phase separated morphology. Depending on the blend composition and many other factors such as processing conditions, the morphologies produced can range from dispersed phase in the form of droplet-matrix [77] and fibrillar [1] to co-continuous[78]. The properties of the blend depend on both the properties of the constituents and the phase morphology. Therefore, by manipulating the morphology for a given set of polymers we can obtain a set of new properties and behaviors.

The co-continuous morphology is promising for the design of electrically conductive blends containing particulate fillers due to the double percolation effect [57]. Double percolation refers to the situation where the conductive filler is percolated throughout the phase in which it is located and that phase is also percolated throughout the system. This decreases the electrical percolation threshold in terms of particle content [3, 79]. This approach is particularly useful when working with high surface area particles such as graphene which tend to aggregate during processing in a single polymer. This aggregation significantly increases the particle content required for electrical percolation. As well as being wasteful, this also has a detrimental effect on the processing and final properties of these blends.

The co-continuous microstructure typically is not stable and tends to breaks up into discrete domains during processing driven by interfacial tension[80]. Therefore, depending on the rheological properties and interfacial tension between the components, a co-continuous morphology normally only exists in the intermediate range of compositions, which restricts the range of obtainable properties.

A practical way to stabilize the microstructure formed during mixing is the addition of nanoparticles. Interfacially localized nanoparticles can reduce the interfacial tension between the polymer pairs [27, 28, 54]. In addition, the localization of nanoparticles inside or at the interface of dispersed domains, greatly increases the elasticity of these domains, which slows down their shape relaxation [25, 29, 30]. In this way, elongated domains formed during mixing can be stabilized by the addition of nanoparticles. Because the percolation threshold of elongated domains is much lower than that of spherical domains[31], the incorporation of nanoparticles can promote the continuity of minor phase. Accordingly, there is possibility to tailor the morphology by the incorporation of conductive nanoparticles to induce a co-continuous microstructure and achieve electrical conductivity and appropriate mechanical properties.

Gubbles *et al* revealed that selective localization of carbon black (CB) in PE minor phase or at the interface of PE (Polyethylene)/PS (polystyrene) blend extended the composition range over which co-continuity was possible [14]. Wu *et al* reported the same effect with the incorporation of carbon black (CB) in an acrylonitrile butadiene styrene (ABS)/ Polyamide 6 (PA6) blend. They showed that with decreasing content of the minor component, PA6, in the blend, more CB is required to induce co-continuity [32]. Additionally, nanoparticle localization and shape (especially platelet-like geometries) both have a significant impact on the final morphology [30]. Here we are exploring this aspect in more detail.

Different mechanisms have been proposed to explain this morphological transition to co-continuity in nanocomposite blends. This transition has been related to the self-networking ability of nanoparticles, which drives the minor phase domains to merge [32, 33]. Nuzzo *et al* [26] concluded that interfacially localized nanoparticles with higher stiffness, are more prone to induce co-continuity in a blend. They proposed a dimensionless group ($\alpha = \frac{\tau_y.P_c}{\sigma_{ij}^2}$) consisting of interfacial tension, σ_{ij}, which drives the deformed droplet towards a spherical shape, and factors that resist the relaxation of interface which are the yield stress of nanoparticle structure in the dispersed domain, τ_y, and the bending stiffness of the nanoparticles, P_c. In spite of these efforts to clarify the mechanism of nanoparticle induced co-continuty there are still important questions that remain unanswered including the role of coalescence. Although the presence of nanoparticles inside the minor phase or at the interface, increases elasticity, stabilizing elongated domains, it can also reduce the coalescence rate. Additionally, the ability of a high aspect ratio nanoparticle to stabilize the domains without piercing the interface depends on the orientation of particles relative to the interface. These issues, which are not incorporated in the model, are not fully understood and are addressed in our work.

There has been relatively little study of the effect of platelet-like nanoparticles blend co-continuity and is limited to clay based nanocomposites [2, 28, 81]. Much of the work with clay nanoparticles is focused on blend compatibilization and does not link state of dispersion, particle orientation and rheological behavior to the induction of co-continuity. Here we investigate the ability of graphene to induce co-continuity, to not only examine its effect on electrical properties but also to elucidate the mechanism of co-continuity induction with respect to rheological behavior, dispersion state and orientation of particles.

A low minor-phase content blend with a co-continuous morphology can also be desirable in terms of mechanical properties, especially in rubber-toughened polymer blends. Xiu *et al* studied the mechanical properties of 85/15 blends of polylactic acid (PLA)/ polyurethane(PU) where co-continuity was induced by SiO_2[82] and CB[83]. They concluded that the formation of a percolated minor-phase structure toughens the blend without sacrificing other mechanical properties like stiffness, tensile strength and ductility. Similarly, Gao *et al* reported an increase in the ductility of low content rubber-toughed PLA due to the co-continuous morphology induced by MWCNT (multiwall carbon nanotube). They also showed that the MWCNT content required for electrical percolation in the blend was 36% less than that required in PLA alone[75]. As expected, at the high filler loading needed to achieve good conductivity, they observed a significant decrease in the ductility of the blend.

In this study, we aim to obtain balanced mechanical and electrical properties of PA6/POE blends by manipulating the morphology with graphene. We begin by exploring the effect of mixing order on the localization of graphene in two systems: (i) a blend of intermediate composition (60/40 PA/POE) which can form at least a temporary co-continuous morphology on its own and (ii) a low POE content (20wt%) blend which requires nanoparticles to induce co-continuity. Polyolefin elastomer was selected as the second phase to toughen the overall system. The ultimate co-continuous systems produced by the incorporation of graphene into these blends offer a range of useful mechanical and electrical properties. As well as comparing the properties of these two systems, we explore the effect of particle dispersion and migration during mixing on the morphology. This aspect remains poorly understood and our work provides important fundamental understanding.

3.3. Experimental Section

3.3.1. Materials

Commercial grades of PA6 (Tecomid NB40 NL E supplied by Eurotec Co.) and POE with MFR 35 g/10min (@190°C, 2.16Kg) and (TAFMER DF 7350 supplied by Mitsui Chemicals Group) were used. The POE is ethylene-octene copolymer with density of 0.87g.cm^3. The complex viscosity dependence on the frequency of these materials is shown in Figure 3-1. Assuming the validity of Cox-Merz [84] rule: $(\eta(\dot{\gamma}) = |\eta*(\omega)|$ where $\dot{\gamma}=\omega)$, it can be concluded that PA has a higher viscosity at all shear rates in comparison to POE. The increase in the complex viscosity of PA6 at low frequency is due to the presence of very high molecular weight chains with long relaxation times.

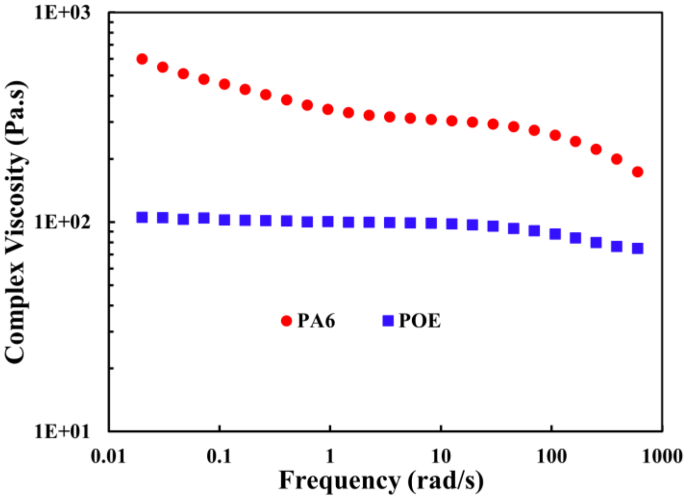

Figure 3-1. Frequency dependence of complex viscosity for blend components (240ºC).

The graphene (N002-PDR) was purchased from Angstron Materials, USA. This graphene is composed of microsheets of 1-3 monolayer sheets in thickness with the following characteristics: thickness 0.35-2 nm, lateral dimension 4 μm (average aspect ratio of about 4000) and surface area 400-800 m^2/g. The composition of atoms by weight percent are as follows: carbon>95%, hydrogen<2%, nitrogen<0.5%, oxygen<2%.

3.3.2. Preparation of Nanocomposites

PA nanocomposites were prepared by melt mixing in a Brabender internal mixer at 60 rpm and 240°C. This temperature was chosen to be higher than the melting points of both POE (55°C) and PA6 (220°C). Prior to compounding, PA6 and graphene were dried at 80℃ for 24 hours under vacuum. Three different compounding sequences were used:

Simultaneous mixing: the polymer components were melt mixed for 1 minute while graphene was added and then compounded for an additional 7 minutes.

POE master batch: POE and graphene were melt mixed for 8 minutes to prepare a 15wt% graphene master batch. The POE master batch was then melt mixed with neat POE and PA6 for 7 minutes.

PA6 master batch: PA6 and graphene were melt mixed for 8 minutes to prepare 15%wt graphene master batch. The PA6 master batch was then melt mixed with POE and neat PA6 for 7 minutes. Note that the mixing times were chosen specifically so that the overall system was mixed together was 7 minutes. This means that the time for the nanoparticles to disperse in the blend during mixing is always the same.

Final specimens were prepared by compression molding at 240 ℃ under 50 MPa for 5 minutes. The characteristics of all systems studied here are presented in Table 3-1.

Table 3-1. Experimental blends and nanocomposites

Sample code	**Composition (PA/POE/Graphene)** wt%/wt%/phr	**Compounding sequence**
60-40	60/40/0	---
60-40-3-O	60/40/3	POE Master batch
60-40-3-A	60/40/3	PA Master batch
60-40-3	60/40/3	Simultaneous mixing

80-20-1-A	80/20/1	PA master batch
80-20-1	80/20/1	Simultaneous mixing
80-20	80/20	---
80-20-0.5-O	80/20/0.5	POE Master batch
80-20-1-O	80/20/1	POE Master batch
80-20-1.5-O	80/20/1.5	POE Master batch
80-20-3-O	80/20/3	POE Master batch

3.4. Characterization

3.4.1. Contact angle measurements

Contact angle measurements were conducted using the KRUS G10 drop shape analyzer in sessile drop mode at room temperature with water and diiodomethane to determine the surface energy of each component. Compression-molded sheets of PA6 and POE, and a compressed disk of graphene were used as substrates. The mean value of five repeats is reported.

Surface tension of components were calculated using the Owens and Wendt equation[58].

$$\frac{\gamma_l\,(\,cos\theta+1)}{2\,(\gamma_l^d)^{1/2}} = (\gamma_s^d)^{1/2} + \frac{(\gamma_l^p)^{1/2}}{(\gamma_l^d)^{1/2}}\,(\gamma_s^p)^{1/2} \tag{3-1}$$

Here, θ is the contact angle between the solid surface and the liquid, γ_l and $\gamma_s$is the surface tension of liquid and solid, and d and p indicates the dispersive and polar contributions of surface energy.

3.4.2. FE-SEM: Field Emission Scanning Electron Microscopy

Specimens were cryo-fractured in liquid nitrogen and etched with n-heptane at 80 ℃ to remove the POE phase. The fracture surface was coated by gold and imaged with a MIRA 3 (7 kV), TESCAN system. The FESEM micrographs were manually analyzed to obtain the average droplet size in the droplet-matrix morphology (at least 300 droplets were analyzed) and characteristic domain size (ξ) of co-continuous morphologies (at least 3 FESEM images were analyzed) using image J software. The characteristic domain size is defined as:

$$\xi = \frac{A_{FESEM}}{L_{interface}} \qquad (3\text{-}2)$$

Here, A_{FESEM} and $L_{interface}$ are the area of FESEM image and the interfacial length, respectively.

3.4.3. TEM: Transmission electron microscopy

Specimens were cryo-microtomed with a Leica Microsystems EM UC7/FC7 Cryo-ultramicrotome into sections of 100 nm thickness at -120°C in liquid nitrogen. TEM analysis was carried out with a FEI Tecnai 12 BioTwin instrument operating at 120 KV.

3.4.4. Rheology

All rheological measurements were carried out on compression molded samples of 1.2 mm thickness and 25mm diameter. Rheological analyses were done at 240 ℃ under nitrogen atmosphere with a stress controlled-stress MCR 502 rheometer with parallel plate geometry at 1mm gap at a strain amplitude 1%. This was confirmed to be within the linear viscoelastic regime using system 80-20-3-O. Frequency sweep measurements were performed from high frequency to low frequency covering the range from 600-0.02 rad/s. The rearrangement of graphene nano platelets during the frequency sweep test increases the elasticity of nanocomposites over the timespan of the experiment. Based on our time sweep experiments (not shown here), most of the changes occur over the first 20 minutes of the experiments meaning that the 5 lowest frequency data points are at an approximate state of equilibrium. Therefore our discussion of these data is focused on the low frequency plateau which is expected to be the most accurate portion.

3.4.5. DMA: Dynamic mechanical analysis

DMA tests were carried out with a Q800 (TA instrument) under single cantilever bending mode at 1Hz and a strain amplitude of 1%. Samples were heated at 5 $℃/min$ from -100 to 150 ℃ and storage modulus and tanδ were measured as a function of temperature. Reported data are the average of at least 2 measurements from different specimens.

3.4.6. DSC: Differential Scanning Calorimetry

Thermal analysis was performed with a TA MDSC Q200. About 8mg of material was heated to 240 ℃ and held for 3 minutes to erase the thermal history, cooled down to 0 ℃ and again heated to 240 ℃ under nitrogen atmosphere. The heating and cooling rate were $10℃/min$ and

5 $°C/min$, respectively. The degree of PA crystallinity is calculated using the following equation:

$$X_c(\%) = \frac{\Delta H_m}{\Delta H_m^0 \times \varphi_{PA6}} \times 100 \tag{3-3}$$

Here, ΔH_m and ΔH_m^0 are the melting enthalpy of PA6 in the blend and melting enthalpy of 100% crystalline PA6 (190.8 J/g [85]) , respectively and φ_{PA6} is the weight fraction of PA6.

3.4.7. Electrical Conductivity

The electrical properties of samples with high volume resistivity ($> 10^9 \mathrm{Ohm.cm}$) were measured with a 4339B Agilent High resistance meter. The tests were carried out on rectangular specimens of 2mm thickness. The electrical properties of samples with low volume resistivity ($< 10^9 \mathrm{Ohm.cm}$) were measured with a 610C Keiyhley resistance meter. The specimens were disks with a diameter of 25 mm and a thickness of 2mm. Reported data are the average of at least 3 measurements from different specimens.

3.5. Results and discussion

3.5.1. Morphological Analysis

3.5.1.1. Graphene localization

Nanoparticle localization is a very important factor determining many aspects of structure and properties of polymer blends [24, 55]. We used thermodynamic analysis to predict the expected location of graphene in our system as described in the supporting information. This analysis predicts that at thermodynamic equilibrium, graphene is located at the interface with a greater affinity toward the PA phase (Table S7-3). However, nanoparticles may not reach to their equilibrium position during the timeframe of processing due to kinetic factors.

TEM observation was performed to determine the location of graphene in these blends (Figure 3-2). In the case of the 60-40-3-O blend, graphene is mainly located inside the POE domains, and a small portion of graphene are localized at the interface (Figure 3-2a). This also occurs in the 80/20 systems produced by POE master batch (Figure 3-2d and 3-2e). The thickness of multilayer graphene at the interface roughly ranges from 4 to 8 nm, which corresponds to 6 to 12 graphene layers. In the case of 60-40-3-A blend (Figure 3-2b), however, graphene is embedded inside the PA phase. The dispersion of graphene is better in this blend due to the higher viscosity of PA in comparison to that of POE and the greater affinity of graphene to this phase. In the blend prepared by simultaneous mixing (Figure 3-2c), we observe graphene particles consisting of 6 to 12 layers, which are primarily located at the interface and within the POE domain. Graphene is concentrated inside POE because of the significant difference in melting temperatures of POE (~55°C) and PA (~220°C). Therefore, at the early stage of mixing POE melts before the PA phase and interacts intimately with the graphene.

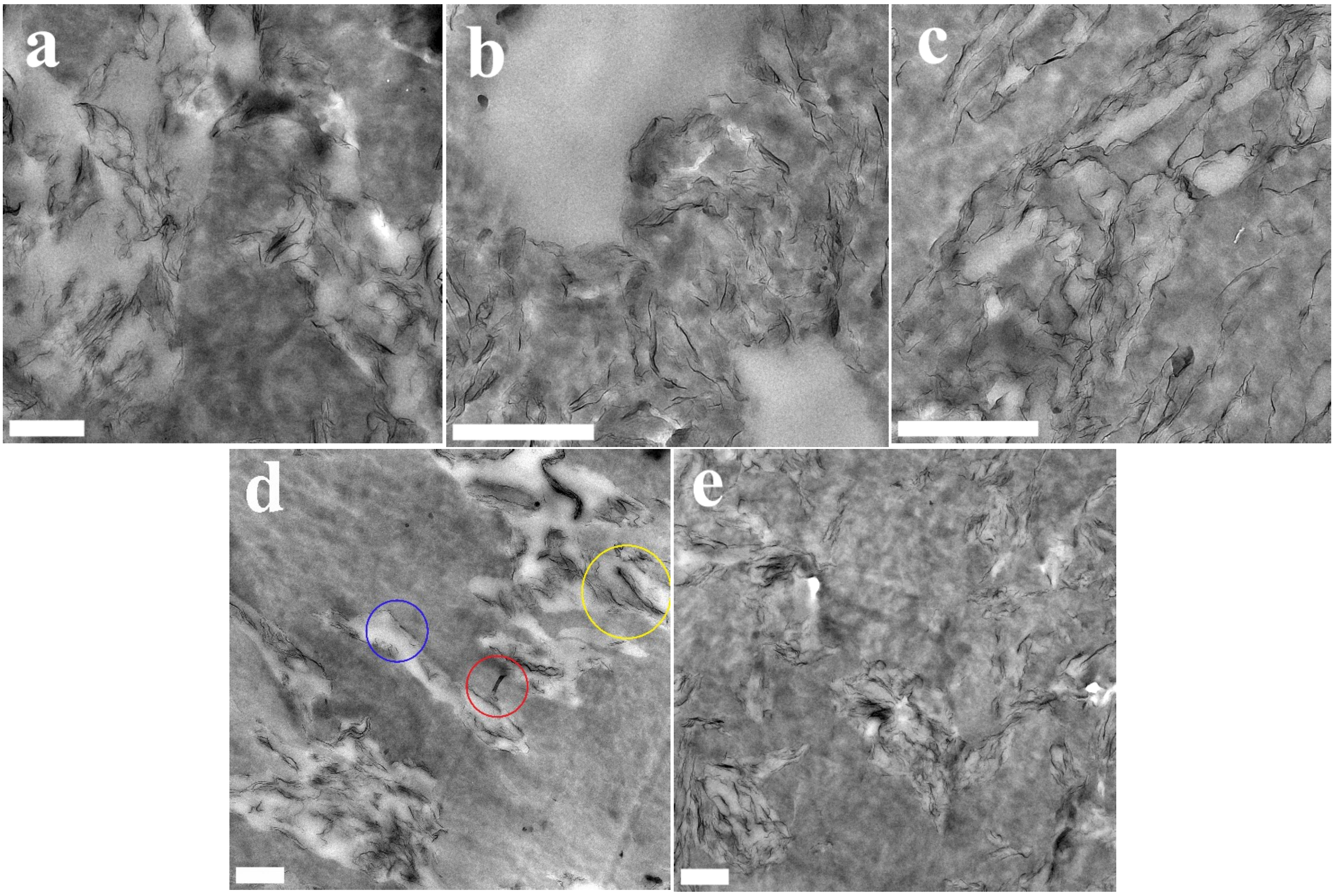

Figure 3-2. TEM images of a) 60-40-3-O, b) 60-40-3-A, c) 60-40-3, d) 80-20-1.5-O, e) 80-20-3-O. White and grey domains are POE and PA, respectively and graphene particles are black. In (d) the blue circle highlights a multilayer graphene particle with thickness 4-8 nm parallel to the interface, the red, dotted circle highlights a large aggregate bridging two nearby POE domains and the yellow, dashed circle indicates large aggregates present in the POE phase. (Scale-bars correspond to 1μm.)

In the case of the 80-20-1.5-O blend (Figure 3-2d), we see one large aggregate that is located in the PA phase perpendicular to the interfaces of two nearby POE domains and forming a bridge between them. This aggregate was able to penetrate into the PA phase due to the high surface curvature instability in this situation. This concept was termed the slim-fast mechanism by Göldel and his coworkers[63]. Similarly, in the case of 80-20-3-O blend, graphene is mainly localized in POE domains. However, a small portion of graphene is within the PA phase often bridging between two discrete POE domains. More graphene is observed in the PA phase in this blend in comparison to the blend containing 1.5wt% of graphene.

In summary, our observations illustrate that well-dispersed graphene which is initially wetted by POE chains can migrate to the interface, while graphene which is wetted by the PA phase, remains inside the PA phase. We note that similar observations with respect to the order of mixing are made with the 80/20/1 systems (Figure 3-3f-h).

Clearly, factors other than the wetting parameter are influencing the graphene localization in the case of the POE and PA master batch mixing processes. One possible explanation for the localization of graphene inside the components in the blend prepared by POE and PA master batch could be differences in the state of graphene dispersion. During the preparation of the concentrated master batch (15wt%) we can expect formation of graphene aggregates. This affects the dispersion state of graphene in the final nanocomposites.

Jalali *et al* described the process involved in the migration of silica particles in a polymer blend during mixing [61]. They suggested that in order for the particle to reach the interface the film between the particle and the interface must first be drained [61] and there should be sufficient time for the primary chains absorbed on the nanoparticle surface to be replaced by chains of the other component [24]. If the film draining time is longer than the time the nanoparticle remains in contact with the interface, it is convected away by the shear flow before it can reach the interface. In the case of a platelet-like particle, the surface area between the interface and particle varies depending on the angle between the nanoparticle surface and the interface. A very slow drainage can be expected when the approaching platelet is parallel to the interface and the fastest drainage occurs when the platelet is perpendicular to the surface. Stacking of multiple platelets increases the drainage time in all orientations and can therefore make it impossible (or simply less likely) for the nanoparticles to reach the interface. In addition, the stacking of multiple platelets results in a higher bending stiffness [86] reducing its ability to conform to the interface. Consequently, these stacked platelet particles are prevented from localizing at the interface via viscous and bending forces. The effect of the state of dispersion on graphene localization can be clearly seen in the TEM image of 60-40-3-O and 80-20-1.5-O blend (Figure 3-2a and Figure 3-2d). Large multi-platelet aggregates of graphene can be observed in the POE domains while graphene particles consisting of 6 to 12 layers are located along and parallel to the interface. This is also obvious in the blend prepared by simultaneous mixing where the graphene particles almost cover the interfacial area (Figure 3-2c). In the case of blend prepared by master batch of PA, although better dispersion is observed in this nanocomposite, we can expect a large activation energy for replacing the absorbed PA chains with POE chains due to the better thermodynamic compatibility of graphene with PA. In addition, the higher viscosity of PA can also retard the migration of graphene towards the interface. Therefore, the graphene initially wetted by the PA phase cannot interact with the POE phase and remains inside the PA phase.

3.5.1.2. Blend morphology

In this section we first consider the effect of graphene localization on the morphology of 60/40/3 and 80/20/1 (PA6/POE/graphene) blends prepared by the three different mixing orders (Figure 3-3). Then the effect of graphene content on the morphology of 80/20 systems prepared by master batch of POE is examined (Figure 3-5).

The morphology of the neat blend 60-40 (Figure 3-3a) is neither fully co-continuous nor droplet matrix. This microstructure is transient, changing during compression molding. This image represents the morphology after 5 minutes of compression molding; after an additional 10 minutes, the morphology becomes more like droplet-matrix (Figure S7.1).

It is well known that in immiscible blends, the lower viscosity component has a greater tendency to become the continuous phase [18, 19]. Our PA has a substantially higher viscosity than our POE (Figure 3-1) affecting the final morphology which exists as a dispersed phase at 60% and only flips to the continuous phase at 70% (Figure S7-2). This shows that due to high interfacial tension and the difference between the two viscosities, this blend has a narrow composition range over which co-continuity is possible. The morphology of the 80/20 neat blend is also droplet-matrix with PA being the continuous phase (Figure 3-3e). The graphene particles change this behavior substantially. The localization of nanoparticles in one component has two consequences: (i) increasing the viscosity of the host phase which reduces the ability of that component to form the continuous phase, and (ii) increasing the elasticity of the host phase which reduces the tendency for break-up in flow. As we have shown, the localization of graphene depends on the mixing order.

The 60-40-3-O blend exhibits a typical co-continuous morphology (Figure 3-3b) due to the localization of graphene in the POE phase which reduces the likelihood of the POE being a sole continuous phase and stabilizes the morphology as explained previously. In the case of 80-20-1-O (Figure 3-3f), highly elongated POE domains can be observed. The nanoparticles in the POE reduce droplet breakup during mixing and slows or prevents shape relaxation during annealing allowing the elongated domains to remain deformed.

Similarly, in the case of 60-40-3-A where the graphene is localized in the PA phase we see elongated PA domains that have merged forming a connected morphology but not a typical co-continuous morphology (Figure 3-3c). Although the nanoparticles increase the viscosity of the

PA phase, which already prefers to form a dispersed phase, the impact of the nanoparticles on the breakup of the elongated domains dominates thus allowing the formation of the connected morphology. The system 80-20-1-A, exhibits a droplet-matrix morphology (Figure 3-3g) where the average droplet diameter is smaller than that of the neat blend, due to the presence of graphene in the PA phase, which acts as a barrier reducing coalescence[35]. Here the droplets are not elongated because the nanoparticles are in the continuous phase (PA). The droplet sizes were evaluated using image analysis and are presented in Figure 3-4.

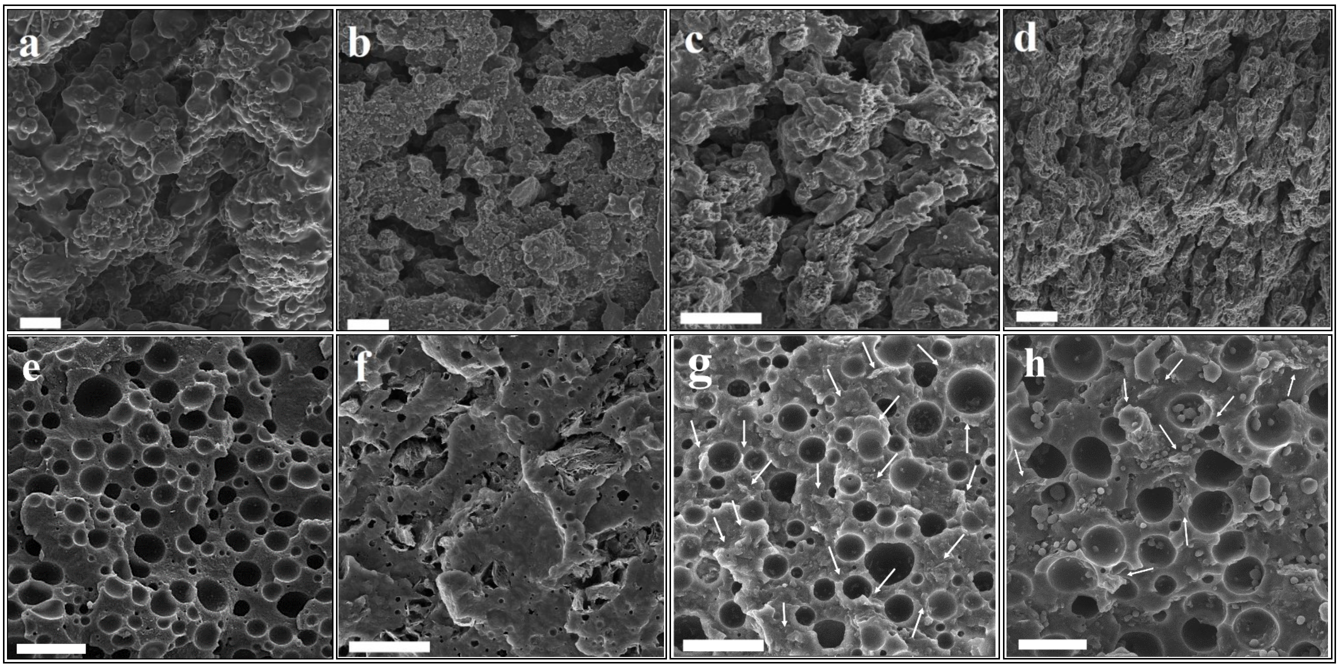

Figure 3-3. FESEM micrographs of a) 60-40, b) 60-40-3-O, c) 60-40-3-A, d) 60-40-3, e) 80-20, f) 80-20-1-O, g) 80-20-1-A, h) 80-20-1. Arrows indicate graphene particles inside the PA phase and at the interface. (Scale-bars correspond to 25 μm for 60-40 systems and 10 μm for 80-20 systems.)

In the case of 60-40-3 blend prepared by simultaneous mixing (Figure 3-3d), a fine co-continuous morphology can be observed. Table 3-2 shows the characteristic domain size, ξ, of the 60/40 systems prepared by different mixing order.

Table 3-2. Characteristic domain size of 60/40 systems containing 3%wt graphene.

sample	**ξ (μm)**
60-40-3	1.95
60-40-3-O	7.84
60-40-3-A	4.34

The 60-40-3 blend, has the lowest ξ, indicating larger interfacial area in this blend. The localization of graphene at the interface in this blend acts as a physical barrier and suppresses coalescence. We can also expect a more stable morphology in this blend during compression molding since the particles at the interface slow shape relaxation (in comparison to graphene inside either phase)[64]. Interestingly, in the 80-20-1 blend prepared by simultaneous mixing (Figure 3-3h), we observe coarsening in the droplet-matrix morphology; the average droplet diameter is larger than that of the neat blend. The graphene in the POE is expected to reduce droplet breakup during mixing, resulting in larger droplets [87]. In blends produced by this mixing procedure, less graphene can be observed in the PA matrix in comparison to the 80-20-1-A (Figure 3-3g and 3-3h). It is shown in TEM images that in the simultaneous mixing graphene that is originally wetted by POE migrates to the interface and graphene initially wetted by PA remains there.

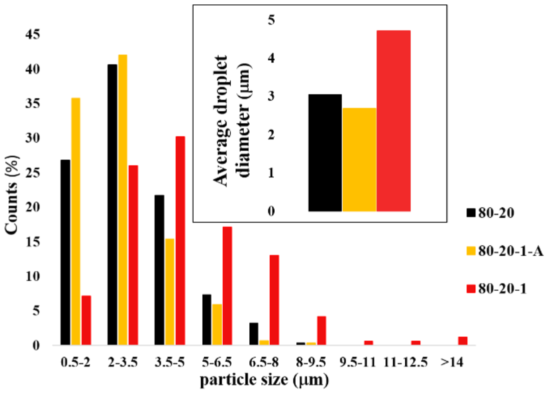

Figure 3-4. Droplet size distribution as determined from analysis of FE-SEM images. Inset shows average droplet diameter for each blend.

Our results show that a wide range of morphologies can be obtained by varying the localization of graphene in the blend. The addition of graphene in the 60/40 system results in a stable co-continuous morphology that can be used for designing electrically conductive blends based on the double percolation effect. However, the main drawback with this composition is the low room temperature modulus of the blend, motivating further investigation on the possibility of inducing a co-continuous morphology at lower POE content. As we have shown, 80-20-1-O blend prepared by POE master batch shows elongated dispersed domains, which indicates that this mixing order can be a promising method to induce co-continuity in the 80/20 composition.

In this regard, we next consider the effect of graphene content on the morphology of our (80/20) blends prepared by POE master batch (Figure 3-5). In the blend containing 0.5%wt graphene (Figure 3-5a), the incorporation of graphene leads to large, elongated droplets. We note that no graphene can be observed in the matrix, indicating that the particles remained in the POE phase during the final mixing. At higher levels of graphene (1% and 1.5 %wt), the elongated domains are merged together and the morphology transitions into co-continuity (Figure 3-5b and 3-5c). At a higher graphene content, 3 %wt, we observe a refinement of the morphology (Figure 3-5d).

Since in the FESEM images for the blends containing high level of graphene domains are not clearly differentiable, a closer view is offered by TEM (Figure 3-2d and 3-2e). The graphene network visible in Figure 3-2e connecting the POE domains with bridge-like structures. Note that, most of the particles are oriented parallel to the interface. These particles contribute to the stabilization of morphology while particles with orientated at an angle relative to the interface penetrate to the PA phase and preserve the 3D structure of graphene in the blend. It seems that the saturation of POE domains with graphene significantly suppresses coalescence, resulting in a reduction in POE domain size. Therefore, it can be concluded that at 3wt% graphene, the co-continuity of POE phase starts to decrease.

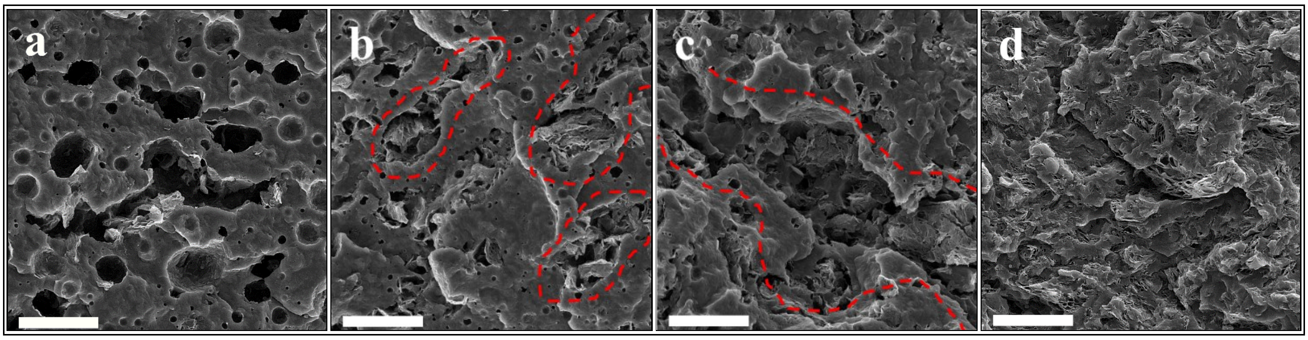

Figure 3-5. FESEM micrographs of a) 80-20-0.5-O, b) 80-20-1-O, c) 80/20-1.5-O, d) 80-20-3-O. Red dashed lines encircle POE domains. (Scale-bars correspond to 10μm).

3.5.2. Rheological and electrical properties

Figure 3-6 shows the melt state linear viscoelastic storage modulus of 80-20 systems prepared by POE master batch and 60-40 systems prepared by different mixing order as a function of frequency with nanoparticle content as a parameter. The corresponding loss modulus are presented in the supporting information (Figure S7-3). In the case of the neat blends, we observe viscous behavior (G”>G’), consistent with droplet matrix morphology for the 80/20 blend and solid-like behavior for the 60/40 blend. Based on our FESEM study we found that this blend has a morphology between droplet-matrix and co-continuous. This rheological behavior generally occurs in blends with co-continuous morphology or in nanocomposites, which have a percolated structure.

All of the nanocomposites exhibit solid-like behavior with a low frequency plateau in the modulus, which shows the formation of percolated graphene structure in this blend. Nuzzo *et al* also observed such solid-like rheological behavior with a polymer blend containing carbon nanotubes when the morphology was not fully co-continuous [26]. The low frequency modulus increases with graphene content, indicating the formation of a stronger percolated structure of particles and co-continuous blend.

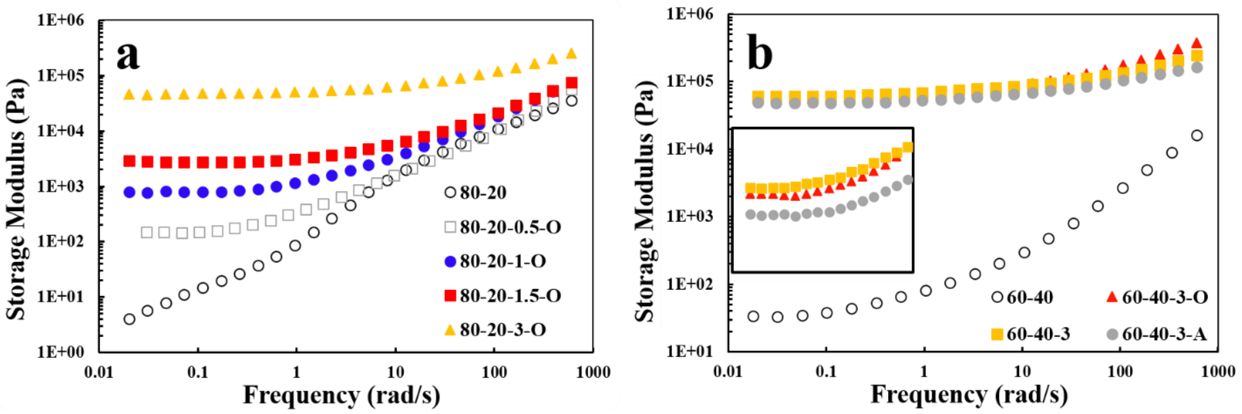

Figure 3-6. Melt state storage modulus of a) 80/20 (PA6/POE) blends prepared by POE master batch, and b) 60/40 blend prepared by different mixing orders.

Comparing the storage modulus of the 60/40/3 systems prepared by different mixing order (Figure 3-6b inset), we can observe that 60-40-3 blend (prepared by simultaneous mixing) has a higher storage modulus. This is due to the localization of a larger fraction of the graphene at the interface which leads to a stronger graphene network [64, 74]. The 60-40-3-O nanocomposite has the next highest storage modulus followed by the 60-40-3-A nanocomposite. This is due to the percolation of graphene inside the minor phase, in this case, POE. Similarly, the 80-20-3-O system has a higher storage modulus plateau in comparison to all 60/40/3 systems. Note that in the 80-20-3-O system the graphene is concentrated in the POE minor phase which occupies a smaller volume than in the 60/40 systems. A similar trend is observed with electrical conductivity.

Figure 3-7 shows the electrical resistivity of the 80/20 blends prepared by POE master batch as a function of graphene content and the 60/40/3 (PA/POE/graphene) blends prepared by different mixing orders. The results clearly show that the electrical resistivity of the blend decreases with increasing graphene content, indicating the formation of a continuous pathway of graphene throughout the blend. For all systems, the electrical conductivity follows the same trends as that of the storage modulus for the same structural reasons.

The percolation threshold can be estimated by fitting the measured electrical conductivity with the conductive filler concentration using the classical percolation model[88].

$$\sigma = \sigma_0 \, (\varphi - \varphi_c)^t \tag{3-4}$$

Here, σ is the measured electrical conductivity, σ_0 is a scaling factor (indicating the intrinsic conductivity of filler), φ is the particle concentration, φ_c is the percolation threshold and t is the critical exponent. Figure 3-7 inset shows the best fit to the experimental data which shows that percolation threshold in this system is 0.66 wt% and the critical exponent is 8.49. Based on the percolation model, the exponent t indicates the dimensionality of the filler network which has value around 1.1-1.3 for two dimensional networks and 1.6- 2 for a three dimensional network in single phase conductive systems [89]. It has been shown that multi-phase percolated systems deviate from the percolation model and generally have higher values of t. The tunneling effect, which is due to the non-random dispersion state of nanoparticles increases the value of t [90, 91]. In our system, this t value is also increased by the presence of aggregates.

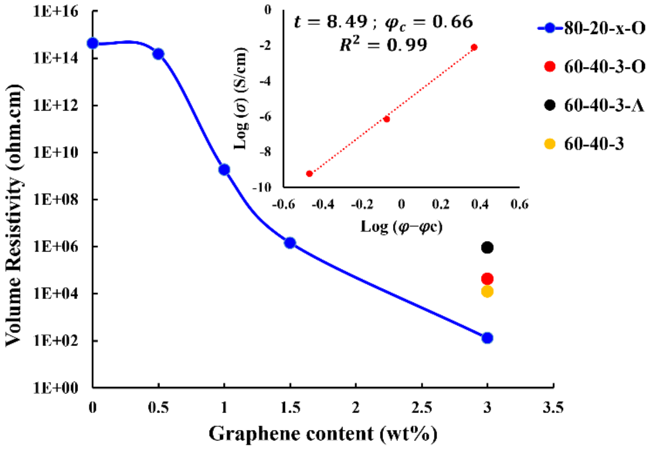

Figure 3-7. Volume resistivity of 80/20 (PA6/POE) blends prepared by POE master batch as a function of graphene content and 60/40/3 blends prepared by different mixing sequences. Inset shows log conductivity (σ) versus log ($\phi - \phi_c$) and the fit of percolation model (Eq. 8) to the experimental data.

In summary, our electrical properties and rheological behavior show that the percolation of graphene inside the component with lower volume fraction results in a stronger graphene 3D network. In the case of the 80-20 system, an increase in the low frequency storage modulus plateau and electrical conductivity with graphene content indicate an increase in the continuity of the POE phase and the connectivity of the graphene. Note that, although in the 80-20-3-O blend we observed a reduction in the continuity of POE, the bridging effect of graphene preserves the graphene network structure leading to an increase in electrical conductivity.

3.5.3. Crystallization behavior

Next, the effect of morphology and graphene on the crystallization of PA are examined. Here we focus only on the crystallinity of PA, because the POE shows very low degree of crystallinity. The crystallization and melting enthalpy of all blends are summarized in Table 3-3 and Figure 3-8. The complementary DSC curves and data are presented in the supporting information (Figure S7-4, S7-5 and Table S7-4). We observe a reduction in PA crystallinity upon the addition of POE along with a further decrease when a co-continuous morphology is attained (60-40-3-O). Co-continuity in blends has previously been shown to decrease crystallinity [92]. The reduction in crystallization in an immiscible blend has been shown to increase with interfacial area [93] because of the energy required by the crystallizable portion to "reject, occlude or deform" the con-crystallizable portion. In the case of a co-continuous structure, these energies are all increased as compared to a dispersed phase morphology. We also note that the PA/POE interface does not act as a nucleator for PA as evidenced by the lack of a change in the crystallization temperature with the addition of POE.

In the (60-40-3-O) blend, the graphene cannot nucleate the crystallization of PA due to its selective localization inside the POE phase. Accordingly, we do not observe any significant change in the crystallization temperature in comparison to that of the neat 60-40 blend.

Another interesting phenomenon observed with the neat 60/40 blend is fractionated crystallization of PA indicated by a small crystallization peak at around 112°C (Figure 3-8a). Fractionated crystallization occurs in droplet-matrix morphology where the number of isolated droplets is larger than the number of heterogeneities in the dispersed phase polymer [94, 95]. As a result, some droplets have no heterogeneities at all and crystallization proceeds by homogeneous nucleation which requires a higher degree of super-cooling than does heterogeneous crystallization. This particular system is the only one that exhibits fractionated crystallization.

Table 3-3. . Crystallization and melting enthalpy of different systems.

Sample	ΔH_{m1} (J. g $^{-1}$)	ΔH_{m} (J. g $^{-1}$)	ΔH_{c1} (J. g $^{-1}$)	$\Delta H_{c2,3}$ (J. g $^{-1}$)
PA	---	89.3	---	87.7
60-40	1.36	48.9	0.7898	48.1

60-40-3-O	---	44.9	---	42.2
60-40-3	---	57.5	---	49.9
60-40-3-A	---	53.4	---	49.3
80-20	---	64.8	---	63.2
80-20-0.5-O	---	64.1	---	61.1
80-20-1-O	---	63.4	---	61.4
80-20-1.5-O	---	62.4	---	60
80-20-3-O	---	56.1	---	56.3

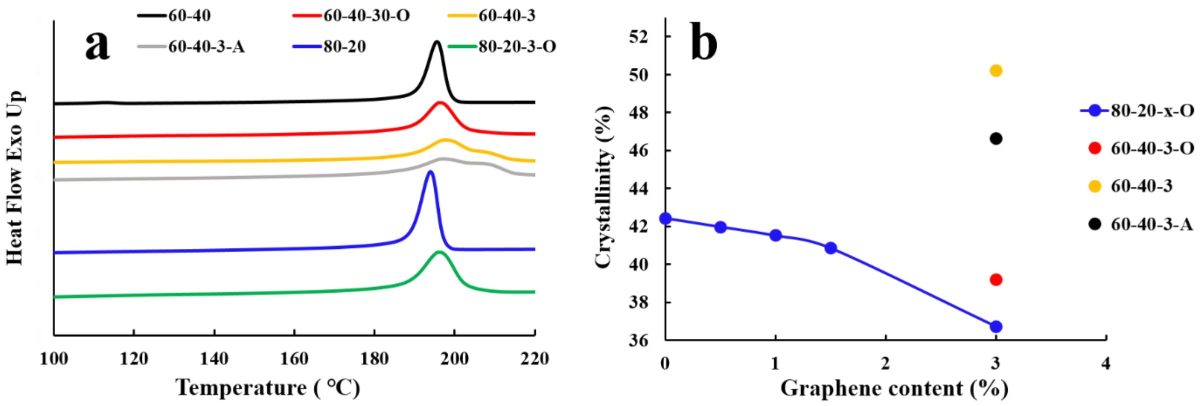

Figure 3-8. DSC cooling curve (5°C/min), and b) Crystallinity of 80/20 (PA6/POE) blends prepared by POE master batch as a function of graphene content and 60/40/3 blends prepared by different mixing sequences.

In the blends prepared by PA master batch and simultaneous mixing, a high-temperature shoulder appears in the crystallization peak of PA (Figure 3-8a). This high-temperature shoulder is a result of the nucleating effect of the graphene, which is located in the PA phase and at the interface of the two components. Owing to the nucleating effect of graphene, 60-40-3 and 60-40-3-A blends have higher degree of crystallinity in comparison to that of the neat 60-40 blend. These results support our conclusions from the morphological study, which indicated that in these blends graphene was localized in PA and at the interface.

For the 80/20 blends prepared by master batch of POE, the crystallinity of PA phase gradually decreases with increasing graphene content likely due to increasing interfacial area and perhaps increased elasticity of the POE domains which can reduce the spherulite growth rate (Figure 3-8b)[93].

In summary, in the case of blends prepared by POE master batch where the graphene is located inside the POE phase, we observe a reduction in PA crystallinity with increasing the continuity of POE phase and interfacial area. On the other hand, graphene acts as a nucleating agent when it is located inside the PA phase increasing the crystallinity of PA.

3.5.4. Thermomechanical behavior

The thermomechanical behavior of our materials represented by the storage modulus (in bending) as a function of temperature is shown in Figure 3-9. We observe two main drops in storage modulus at around -30 and 74°C, corresponding to the glass transition temperatures of POE and PA, respectively. Generally, the solid-state storage modulus of nanocomposites is governed by three factors: (i) morphology of blend, (ii) the inter-connected structure of the nanoparticles, and (iii) crystallinity. The storage modulus of blends with droplet matrix morphology is primarily determined by the matrix. In the case of a co-continuous morphology both components significantly affect the storage modulus. In the case of the neat 60-40 blend, the storage modulus approaches zero at temperatures higher than the melting temperature of POE (~55°C) indicating that POE is the major phase in this blend, which is consistent with the imaging (Figure 3-3a).

In the case of the nanocomposites, due to the reinforcing effect, the glassy storage modulus ($T<T_g$ POE) increases with the incorporation of graphene. At intermediate temperatures (T_g POE $<T<T_g$ PA) the storage modulus exhibits a plateau (Figure 3-9a). This reveals that PA can resist stress over this temperature range, indicating the formation of a co-continuous morphology. Although the crystallinity of PA in 60-40-30-O blend is lower than that of 60-40-3-A blend, it has a higher storage modulus at intermediate temperatures. This increase in the storage modulus comes from increased continuity of the PA phase and the strength of the inter-connected graphene structure (note that a similar trend was observed in the melt-state rheological behavior).

Similar to 60/40 systems, the reinforcement effect of graphene can be observed in the case of 80/20 blends prepared by POE master batch (Figure 3-9b). Interestingly, the storage modulus plateau in the intermediate temperature range is almost the same for these blends. The storage modulus of different systems at room temperature are presented in Figure 3-9c. It can be observed that a wide range of properties is achievable by the incorporation of graphene and changing the mixing order.

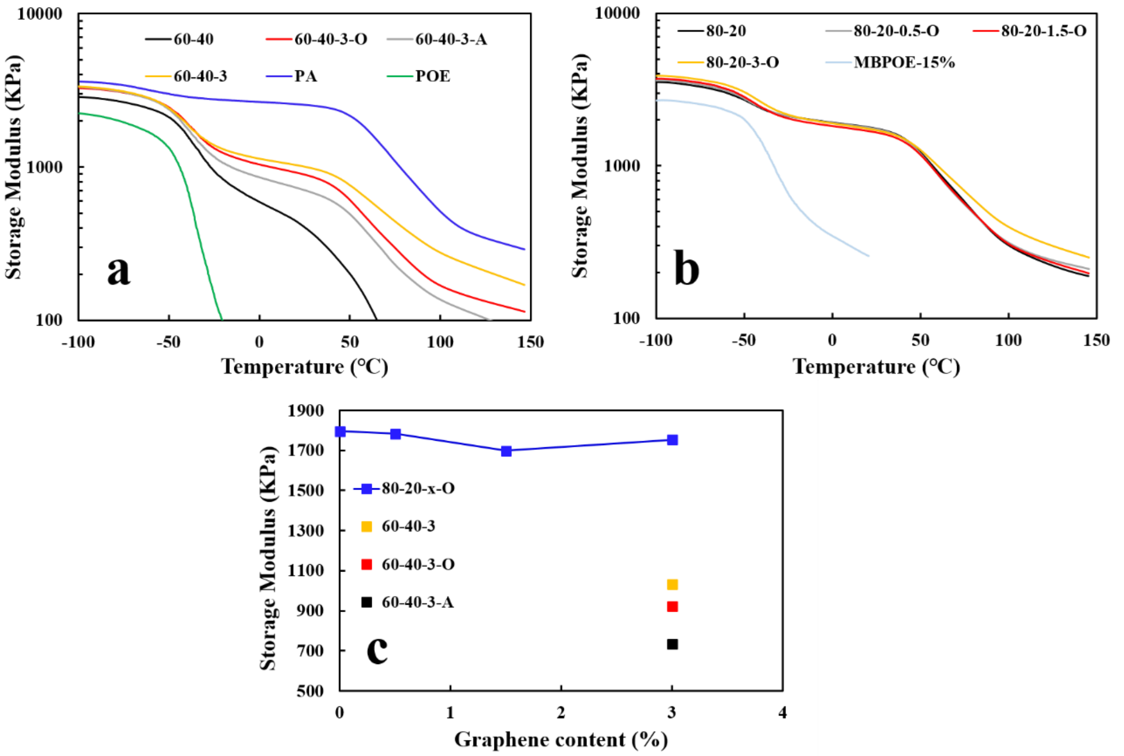

Figure 3-9. Temperature dependence of solid state storage modulus for a) 60/40 (PA6/POE) blends prepared by different mixing sequences, and b)80/20 (PA6/POE) blends prepared by master batch of POE, and c) Storage Modulus at 20℃ as a function of graphene content for different systems.

3.6. Conclusion

Our results highlight the role of graphene localization on the morphology of PA6/POE blends. We reveal that the localization of graphene strongly depends on the dispersion state, which is governed by the mixing order. In the case of blends prepared by master batch, graphene mostly remains inside the initial premixed component. However, in the case of simultaneous mixing, a higher portion of graphene is localized at the interface due to improved dispersion. This provides important new guidelines for the formulation of polymer blend systems incorporating nanoparticles, particularly plate-like nanoparticles.

We have also shown that a wide range of morphologies and properties can be achieved by varying the mixing order. The morphology is determined by the impact of graphene on the viscosity and elasticity of its host phase. The presence of graphene inside the minor phase increases the elasticity of that phase allowing the formation of stable elongated domains, which results in co-continuous morphologies. These morphological changes influence the thermomechanical properties of these systems resulting in a wide range of room temperature stiffness.

We have further shown that beside the rheology of the minor phase, the role of coalescence should be considered as an important factor in nanoparticle induced co-continuity since a reduction in coalescence rate reduces continuity. Additionally, the penetration of graphene to the PA phase preserves the graphene 3-D network structure even if continuity is reduced, which cannot occur in the case of nanocomposites containing spherical nanoparticle.

Finally, we have shown that the percolation of graphene inside the minor component leads to higher electrical conductivity. Therefore, by inducing a co-continuous morphology at low volume fraction of minor phase, we can achieve a very low percolation threshold. This can be especially important in graphene-based nanocomposites prepared by melt mixing which generally show large percolation thresholds.

4. Evolution of phase morphology, rheology and electrical conductivity of PA6/POE blends containing graphene during annealing under SAOS

4.1. Abstract

The evolution of rheological response, phase morphology and electrical properties of PA6/POE blends (80/20) with graphene primarily localized inside the POE minor phase and at the interface are investigated during annealing under small amplitude oscillatory shear (SAOS). Analysis of the dynamic viscoelastic response of these nanocomposites revealed that it is primarily governed by the graphene 3-dimensional structure, which evolves during the rheological measurement. Comparing isochronal frequency sweeps with frequency sweeps close to the equilibrium condition illustrates that graphene content and the evolution of its 3D structure have the same impact on rheological and electrical properties. Interestingly, regardless of different blend morphology, the linear and non-linear viscoelastic behavior follow the fractal scaling theory indicating that the 3-dimensional graphene structure is self-similar.

With increasing graphene content, the phase morphology changes from typical droplet-matrix morphology to droplet clusters and co-continuous morphology. The stability of the blend morphology when annealing under SAOS (0.1 rad/s) depends on the balance between the rate of coalescence and shape relaxation. Interestingly, our morphological observation for nanocomposites containing 0.5 and 1% of graphene shows that while the presence of graphene slows down the shape relaxation, it increases the coalescence rate within the first 30 minutes of annealing as compared to the neat blend. The increased coalescence rate comes from the normal force applied during sample loading along with a slow shape relaxation and graphene bridging between neighboring domains.

4.2. Introduction

Phase morphology plays an important role in the final macroscopic properties of polymer blends. The morphology in polymer blends is mainly governed by the constituent composition, rheological properties (viscosity and elasticity) and interfacial tension between the components. The morphology formed during mixing is usually not in the equilibrium state and evolves during the post-processing steps. However, fine morphologies formed during mixing are usually most desirable[35]. An effective strategy to stabilize both droplet-matrix and co-continuous morphologies is the addition of nanoparticles. In the case of interfacially adsorbed nanoparticles, this stabilization effect arises primarily from a combination of reduced interfacial tension and enhanced interface elasticity [2, 87]. When nanoparticles are localized inside the bulk component the main factor is the increased viscosity of the host phase[36]. The stabilization efficiency of nanoparticles is governed by factors such as localization, geometry and self-assembly of nanoparticles.

In the case of organoclay platelets, Khatua et al observed enhanced blend morphology stabilization when well-exfoliated particles were within the matrix [96], while its presence in the dispersed phase had little effect. The morphology stabilizing effect is most pronounced when nanoparticles are localized at the interface. For example, Trifkovic et al showed that a very low content (1 wt%) of interfacially absorbed clay particles almost completely suppresses the coarsening of a co-continuous morphology [78]. At lower particle contents coarsening continued until the interface was covered by the clay particles, indicating that interfacial jamming is the main mechanism of stability. The same jamming-related morphology stabilizing effect has been observed in the case of interfacially absorbed graphene particles [3, 64].

It is well-known that nanoparticles are mobile and the 3-dimensional network of the nanoparticles also evolves during the annealing process. This has been observed even for non-Brownian particles such as clay and graphene in high viscous molten polymer matrixes, and attributed to the interaction between the particles and flocs [97]. There is some evidence that the self-assembly pattern of nanoparticles can also affect the stability of phase morphology [32, 33]. Wu et al observed increased dispersed phase continuity during annealing when carbon black (CB) particles were inside the dispersed phase[32], despite the particle-induced increased viscosity. The authors attributed this to the tendency of CB particles to form a 3-dimensional network which forces the dispersed domains to merge with one another. In sharp contrast, titanium oxide (TiO2) nanoparticles have the tendency to form compact clusters and are thus not able to stabilize co-continuous morphologies [33].

Nanoparticles can induce various morphologies in binary blends such as irregular dispersed domain shapes, droplet clusters[53] or co-continuous morphology[14, 26]. These morphologies are usually observed when the nanoparticles are localized inside the dispersed domains or at the interface[98]. This is the consequence of a complex interplay of the effect of nanoparticles on breakup, coalescence and stability of domains[24]. Co-continuous morphology is of importance particularly in electrically conductive blends allowing one to significantly reduce the percolation threshold of a conductive filler[75, 99] We have previously shown that graphene platelets were able to promote co-continuous morphology when they were localized at the interface and inside the minor phase[99]. It is possible here to manipulate the morphology with graphene particles and achieve unique electrical and mechanical properties at low minor phase content.

In this study, we investigate the evolution of phase morphology and microstructure during annealing using a rheometrical approach while also characterizing the electrical conductivity. In order to allow a direct comparison between rheological and morphological evolution, we imaged sections of the specimens used in the rheological testing. This allows us to take into account the effect of compression and shearing forces generated during specimen loading in the rheometer on the morphology which are absent in annealing under quiescent conditions. Finally, the graphene 3D network close to the equilibrium condition was characterized using the fractal approach.

4.3. Experimental section

4.3.1. Materials

A commercial grade of PA6 Tecomid NB40 NL E supplied by Eurotec Co. was used as the major component. POE (TAFMER DF 7350) supplied by Mitsui Chemicals Group was used as the minor phase (MFR 35 g/10min @190°C, 2.16Kg). The graphene (N002-PDR) was supplied by Angstron Materials. This graphene consists of nanoplatelets of 1 to 3 monolayers.

4.3.2. Preparation of Nanocomposites

PA6/POE blends with fixed weight composition of 80/20 were prepared by melt mixing in a Brabender internal mixer at 60 rpm and 240℃. Prior to compounding, PA6 and graphene were dried at 80℃ for 24 hours under vacuum. In order to prepare the nanocomposites, first a master batch of POE with 15%wt of graphene were prepared through melt mixing in internal mixer for 8 minutes. The POE master batch was then melt mixed with neat POE and PA6 for 7 minutes. Similarly, in the case of the neat blend, the POE and PA6 were melt mixed for 7 minutes at 60 rpm. Accordingly, the time for formation of blend phase morphology is the same for the neat blend and nanocomposites.

The specimens for rheological measurement were compression molded in the form of discs with diameter of 25mm and thickness of 2mm at 240 ℃ under 50 MPa for 5 minutes. The characteristics of samples are summarized in Table. 4-1.

Table 4-1. Experimental blend and nanocomposites.

Sample code	Composition (PA6/POE/Graphene) wt phr	Composition (PA6/POE/Graphene) vol%
80-20	80/20	76/24
80-20-0.5	80/20/0.5	75.76/24/0.24
80-20-1	80/20/1	75.54/23.98/0.48
80-20-1.5	80/20/1.5	75.35/23.93/0.72
80-20-3	80/20/3	74.81/23.75/1.44

Since the PA component is expected to undergo post condensation and degradation during the mixing and rheological measurement, we melt mixed PA6 in the internal mixer at the above processing conditions for 7 minutes and then performed rheological characterization (results in Fig. S7-6). Although it undergoes thermal degradation during the mixing step, the storage modulus during the time sweep measurement is more stable. Because the impact of nanoparticles on the material functions (increase by 800% for the lowest graphene content) is significantly larger than that of degradation during rheological measurements, degradation is unlikely to affect our conclusions, especially in the case of nanocomposites.

4.3.3. Rheology

Rheological tests were performed with an MCR 502 rotational rheometer at 240ºC under dry nitrogen atmosphere, with a parallel plate configuration (25mm) at a 1 mm gap. The linear viscoelastic region was evaluated by strain sweep tests for each sample. The time sweep and sequential frequency sweep measurements were conducted in the linear viscoelastic region as follows. The specimens were loaded, and the gap reduced to 2.1mm (slightly higher than the thickness of specimens). At this point the specimens were held for 3 minutes at 240 ºC to melt before reducing the gap to 1.025mm, specimens were then carefully trimmed, and the gap reduced to 1mm (measurement position) at 4 minutes after loading the sample. The specimens were then annealed for a further 4 minutes before starting the SAOS. Note that the lowering speed of the plate was the same for all specimens except for the 80-20-3 sample. In this case, due to its high viscosity, the force required to press the sample at the same rate exceeds the normal force limit (15 N/m^2) of the instrument, requiring slightly longer squeezing time.

Specimens for morphological imaging were removed from the rheometer at 3 different stages: (i) after trimming and lowering the gap to 1mm and (this process takes 4 minutes), (ii) after 30 minutes of time sweep (34 minutes after loading and pressing the sample), (iii) after 2 hours of time sweep (124 minutes after loading and pressing the sample). These specimens were cooled under nitrogen in the rheometer at a rate of ~ 7 °C/min. Accordingly, it takes about 6 minutes for the temperature to reach the crystallization temperature of the PA component (~195°C) which is expected to freeze the phase morphology.

In order to examine the impact of compression force in the rheometer, specimens were also annealed under quiescent conditions at the same temperature. For this purpose, the samples were placed in the rheometer, at 240 ºC for 4 minutes (corresponding to time=0 in the SAOS experiment) and 38 minutes (corresponding to time = 30 minutes of SAOS plus 4 minutes to reach thermal equilibrium) and were cooled with the same cooling rate ~ 7 °C/min. Note that the thermal and mechanical history for all the materials were the same before loading the samples in the rheometer.

Linear viscoelastic measurements close to the equilibrium condition were conducted from low to high frequency (0.02-600 rad/s) after a 2-hour time sweep at 0.1 rad/s. Similarly, the strain sweep experiments were carried out after a time sweep experiment where the storage modulus reached almost a steady value. All the rheological data is the average of 3 repeats.

For the sequential frequency sweeps, 10 sweeps were performed from 0.093 to 600 rad/s. The isochronal frequency sweeps were then determined by interpolation using the Akima cubic spline method[100].

4.3.4. SEM: Scanning Electron Microscopy

SEM observations were conducted with a S-3400N, Hitachi system operating in variable pressure mode at 15 kV on the cross sections of discs removed from the rheometer as explained above. Prior to SEM observation, samples were cryo-fractured in liquid nitrogen and then the POE phase was extracted with xylene at 120°C for 4 hours.

The SEM micrographs were analyzed using ImageJ [101] with a manual assist when needed. At least 6 SEM images (1000-1500 domains) from different locations with magnification of 1000x were analyzed for each condition/time. Based on optical microscopy images (not shown here), the area covered at this magnification is approximately 2-3 times larger than the largest unit of the fractal-like structures of the nanocomposites. The morphology was analyzed in terms of three parameters:

The first being the characteristic domain size (ξ) defined as:

$$\xi = \frac{A_{SEM}}{L_{interface}} \tag{4-1}$$

where, A_{SEM} and $L_{interface}$ are the area of SEM image and the interfacial length, respectively. The second being the number of discrete domains per unit area (N) defined as:

$$N = \frac{Number\ of\ domains}{A_{SEM}} \tag{4-2}$$

Finally, the circularity is defined as:

$$C = \frac{4\pi\,(area)}{(Perimeter)^2} \tag{4-3}$$

4.3.5. TEM: Transmission of electron microscopy

The localization of graphene was studied by a FEI Tecnai 12 BioTwin TEM at an acceleration voltage of 120 kV on the cross sections of discs removed from the rheometer as explained above. The specimens were cryo-microtomed with a Leica Microsystems EM UC7/FC7 Cryo-ultramicrotome into sections of 100 nm thickness at -120°C with liquid nitrogen cooling system. The imaging can be performed without any further staining, due to the difference between crystallinity and density of the polymer components giving rise to the phase contrast (the darker phase is PA6). The phase assignment is consistent with the volume fraction of components and the dispersed phase morphology.

4.3.6. Solvent extraction of PA6 phase

In order to investigate the 3-dimensional continuity of the POE phase, compression molded specimens were cut into 10mm×15mm×2mm sheets and soaked in 30ml of formic acid for two days at room temperature to dissolve the PA6 major phase. The solvent was replaced after 24 hours. The phase morphology of samples, which were self-supporting after extraction, was considered co-continuous.

4.3.7. AC conductivity

The dielectric properties were measured using a Novocontrol broadband dielectric spectrometer in the frequency range of $10^{-1}\times10^{5}$ Hz under an excitation voltage of $3V_{RMS}$ with parallel brass plated electrodes. The measurements were performed on disc shape specimens (dia=25mm) with a thickness of 2mm (for samples before annealing under SAOS) and 1mm (for samples after annealing under SAOS).

4.4. Result and discussion

4.4.1. Morphological evolution

Fig. 4-1 summarizes the morphological evolution for the neat blend and the nanocomposites during a time sweep in the rheometer at 0.1 rad/s along with the SEM micrographs of blends after 2 hours. Since the domains in blends containing graphene are highly irregular in shape, we characterize the morphology with two parameters: (i) characteristic length (ξ) and (ii) number of discrete domains per 1000μm^2 (N). The former conveys information about the interfacial area which is governed by both domain coalescence and shape relaxation, both increasing ξ, and the latter is governed by coalescence, decreasing N. We note that N is sensitive to the continuity of the POE phase.

Additionally, the distribution of domain circularity (C) for the blends after 2 hours of annealing under SAOS is presented in Fig. 4-2. Note that the distribution of circularity does not change significantly during the annealing under SAOS. The distribution of domain circularity for time=0 is provided in the supporting information, Fig. S7- 9.

Due to the concentration of graphene inside the POE domains, it was not possible to accurately characterize the phase morphology of the nanocomposites containing 3%wt of graphene.

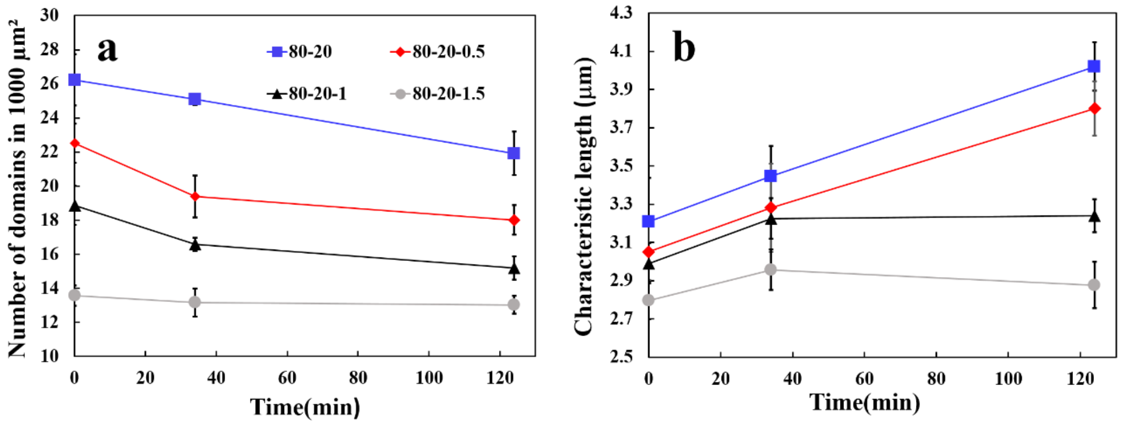

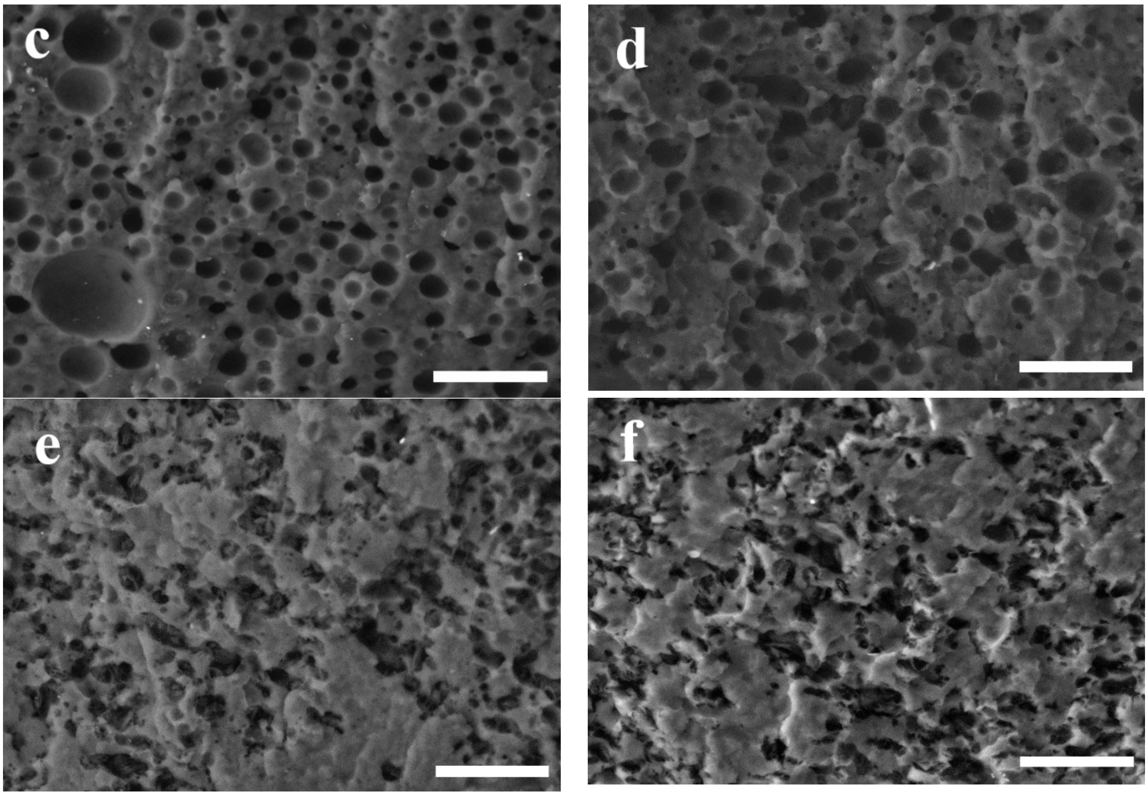

Figure 4-1. Changes in N (a) and ξ (b) during SAOS at 240ºC and 0.1 rad/s within the LVE (Lines are to guide the eye). SEM images of phase morphology after 2 hours of SAOS for: 80-20 (c), 80-20-0.5 (d), 80-20-1 (e), 80-20-1.5 (f). The POE phase is extracted. The scale bars correspond to 25µm.

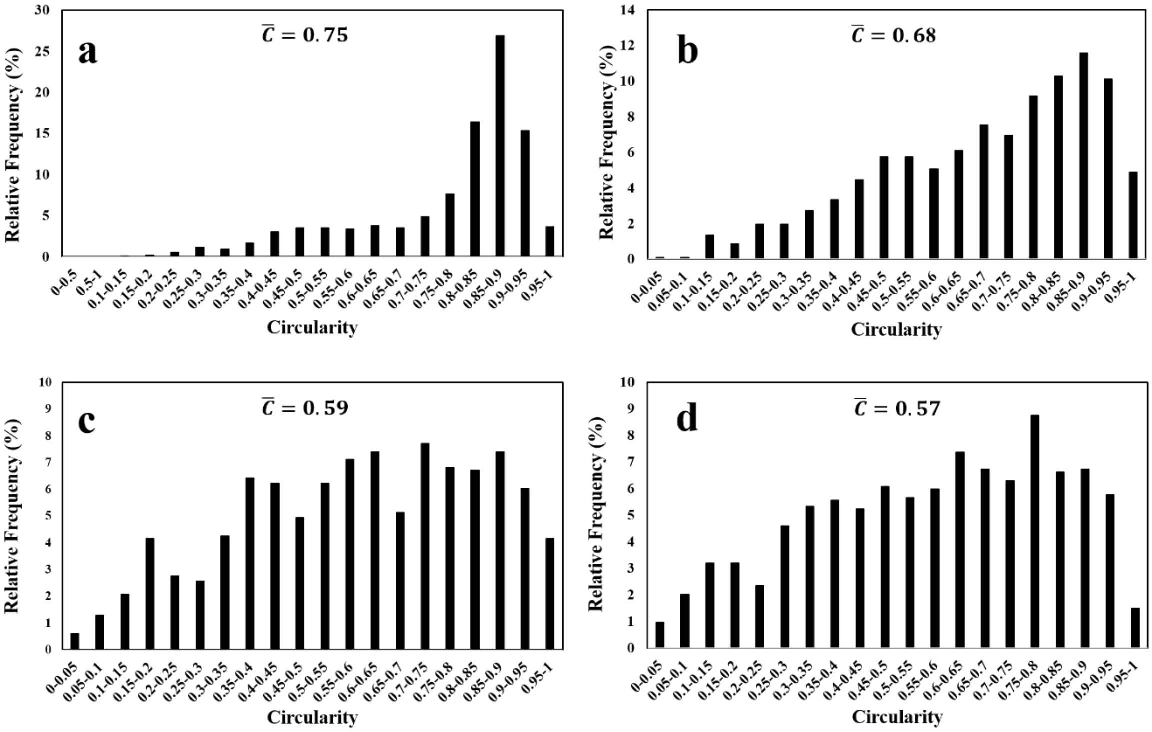

Figure 4-2. Distribution of domain circularity after 2 hours annealing under SAOS for: a) 80-20, b) 80-20-0.5, c) 80-20-1 and d) 80-20-1.5.

Before examining the effect of annealing under SAOS for each sample, first we summarize the general consequences of the presence of graphene. Note that the graphene is localized inside the POE phase and at the interface (Fig. 4-3). The localization of graphene at the interface is in line with the prediction from the wetting parameter at the equilibrium condition [99]. It is also worth noting that the interfacial tension between the graphene and PA6 is lower than that of POE/graphene indicating that graphene tends to be preferentially wetted by the PA6[99].

With increasing graphene content: (i) the number of discrete domains decreases indicating the formation of more interconnected morphology; (ii) more elongated domains are formed (Fig. 4-2) giving rise to a decrease in characteristic length corresponding to an increase in interfacial area; (iii) the stability of phase morphology is enhanced; and (iv) the distribution of domains becomes non-homogeneous.

Generally during annealing under SAOS, the number of domains decreases and the characteristic length increases except for 1.5 wt% graphene where we observe stable morphology. As noted, we were unable to view the morphology of the 3 wt% nanocomposite, nevertheless we expect that its morphology is stable during annealing under SAOS like the 80-20-1.5 nanocomposite. In the following, we start by describing the behavior of the neat blend and then we consider the morphologies, at the initial state and after 30 and 120 min of annealing in detail.

The neat blend exhibits a typical droplet matrix morphology with POE being the dispersed phase. Note that the droplets in the neat blend at time=0 (after lowering the gap in the rheometer but before applying SAOS, Fig. S7-7a) are almost spherical indicating the fast shape relaxation of the POE domains due to high interfacial tension between the components. During annealing under SAOS, the dispersed domains coalesce with one another to reduce the interfacial area leading to a linear decrease in N and an increase in the characteristic length.

With respect to the initial state, at time=0 (Fig. S7-7), in the case of nanocomposites the morphology consists of elongated and irregular domains resulting in a lower ξ as compared to the neat blend. The number of elongated domains increases with particle content. We note that in the system with the lowest graphene content (80-20-0.5) the domains appear to be clusters of smaller droplets while in the other nanocomposites this is not the case. At the higher graphene contents, we see smaller irregular domains which are partially coalesced with one another or connected with very thin, stable necks (Fig. 4-3-d and e). The size of the POE domains increases with graphene content (up to 1.5%) and thus N decreases. (Fig. S7-7e). Note that we previously observed a refinement in the morphology at 3%wt of graphene (TEM image of this nanocomposite can be found elsewhere [99], Fig. 4-2-e). These domains are also connected with graphene bridges. Same reduction in domain size is also observed by Kong et al [102] above a critical ratio of nanoparticle to minor phase concentration in the case of nanosilica filled polystyrene/ polypropylene blends. Finally, the circularity distribution (Fig. S7-9) broadens with increasing particle content. We note that the average circularity ($\bar{C}$) represents the breadth of the distribution with values closer to one indicating a narrower distribution.

During annealing under SAOS, the morphological evolution depends on domain coalescence and shape relaxation increasing the characteristic length. We can separate out the contribution of coalescence by tracking the parameter “N”. Note that although we use the general term “coalescence”, the droplets containing graphene do not fully merge with each other during annealing, instead they mostly form droplet clusters due to the localization of graphene at the interface (Fig. 4-3).

Now we consider the evolution in morphology in the first 30 minutes of annealing under SAOS. From Fig. 4-1-a we observe a non-monotonic impact of graphene on the coalescence rate, as inferred from the slope of the N vs time curve, with the highest rate at 0.5wt% of graphene.

This is interesting because with the addition of nanoparticle the number of discrete domains decreases which should increase the distance between the neighboring domains reducing the coalescence rate. To understand this behavior, we annealed specimens of the neat blend and nanocomposites containing 0.5 and 1%wt graphene at the same temperature but under quiescent conditions (without compressing the sample in the rheometer and applying SAOS). We observe considerable differences in terms of phase morphology and its evolution with these two mechanical histories (Figures S7-8 and S7-9 for quiescent conditions). By comparing the morphological analyses for the two mechanical histories, we summarize the impact of sample compression in the rheometer (Table. 4-2). After sample compression (i) the domains become elongated corresponding to a decrease in average circularity (Fig. S7-9); (ii) the number of discrete domains, N, decreases significantly, i.e. the normal force induces coalescence between the domains; and (iii) in spite of a larger number of discrete domains, the rate of coalescence during annealing is lower under quiescent conditions as compared to that of the blends after compressing the sample.

Table 4-2. Summary of morphology at time = 0 under both quiescent and SAOS conditions.

sample	N at time=0		Average circularity index at time=0	
	SAOS	quiescent	SAOS	quiescent
80-20	26.23	34.03	0.74	0.83
80-20-0.5	22.51	35.33	0.67	0.80
80-20-1	18.87	24.86	0.62	0.71

Under quiescent conditions, the coalescence rate is controlled by the distance between the neighboring domain (number of domains at a same volume fraction), the viscosity of the dispersed domain and van der Waals forces between the domains. In the case of the neat blend and the 80-20-0.5 nanocomposite with almost same initial number of domains, the coalescence rate is higher in the neat blend. For spherical domains with same radius (R), the van der waals force can be estimated by Eqn. 4-4 [103]:

$$F_w = \frac{AR}{12H^2} \tag{4-4}$$

Here, A is Hamaker constant and H is the distance between the domains. Our analysis showed that the Hamaker constant for the bare POE and graphene coated POE domains are essentially the same (see supporting information). Accordingly, the lower coalescence rate in the 80-20-0.5 nanocomposites is probably due to the higher effective viscosity of POE domains. In the case of the 80-20-1 nanocomposite, both the lower number of neighboring domains and the increased viscosity results in a decreased coalescence rate.

These results show that the larger coalescence rate in annealing under SAOS, comes from the normal force which is not relaxed before the SAOS is applied. The presence of nanoparticles at the interface (Fig. 4-3) slows down the shape relaxation of the domains which were deformed during the lowering of the gap. This elongation decreases the distance between neighboring domains in some regions allowing [104] van der Waals forces to dominate. Additionally, the presence of nanoparticles at the interface is expected to increase the rigidity of the interface thus facilitating coalescence by decreasing the drainage time. When the domains contact each other, graphene particles at the interface bridge the domains (Fig. 4-3) significantly increasing the contact time. This gives rise to the formation of a non-homogeneous distribution of POE domains with a fractal-like structure. We note that Nagarkar and Valenkar observed the same bridging phenomenon in the case of “interfacially active” silica particles in polyethylene oxide (PEO)/polyisobutylene (PIB) blends with a droplet matrix morphology [105].

Next, we consider the evolution in morphology in the second phase of annealing under SAOS from 30 to 120 min. The relevant SEM images are presented in Fig S.7-7. During this time, the number of discrete domains remains essentially constant in all the nanocomposites (Fig. 4-1). Accordingly, the change in the characteristic length observed for 80-20-0.5 primarily comes from the shape relaxation. This is expected because at higher graphene contents (1% and 1.5%wt), the interfacial area is covered by graphene (Fig. 4-3d and e) effectively suppressing shape relaxation. From this, we conclude that in between 0.5 and 1 wt% there is a critical graphene content needed to fully stabilize the shape relaxation at long times. Note that although the slope of the characteristic length over time is almost the same for the neat blend and the 80-20-0.5 nanocomposite, the underlying phenomena are different. In the case of the neat blend, the increase in the ξ is due to coalescence, not shape relaxation.

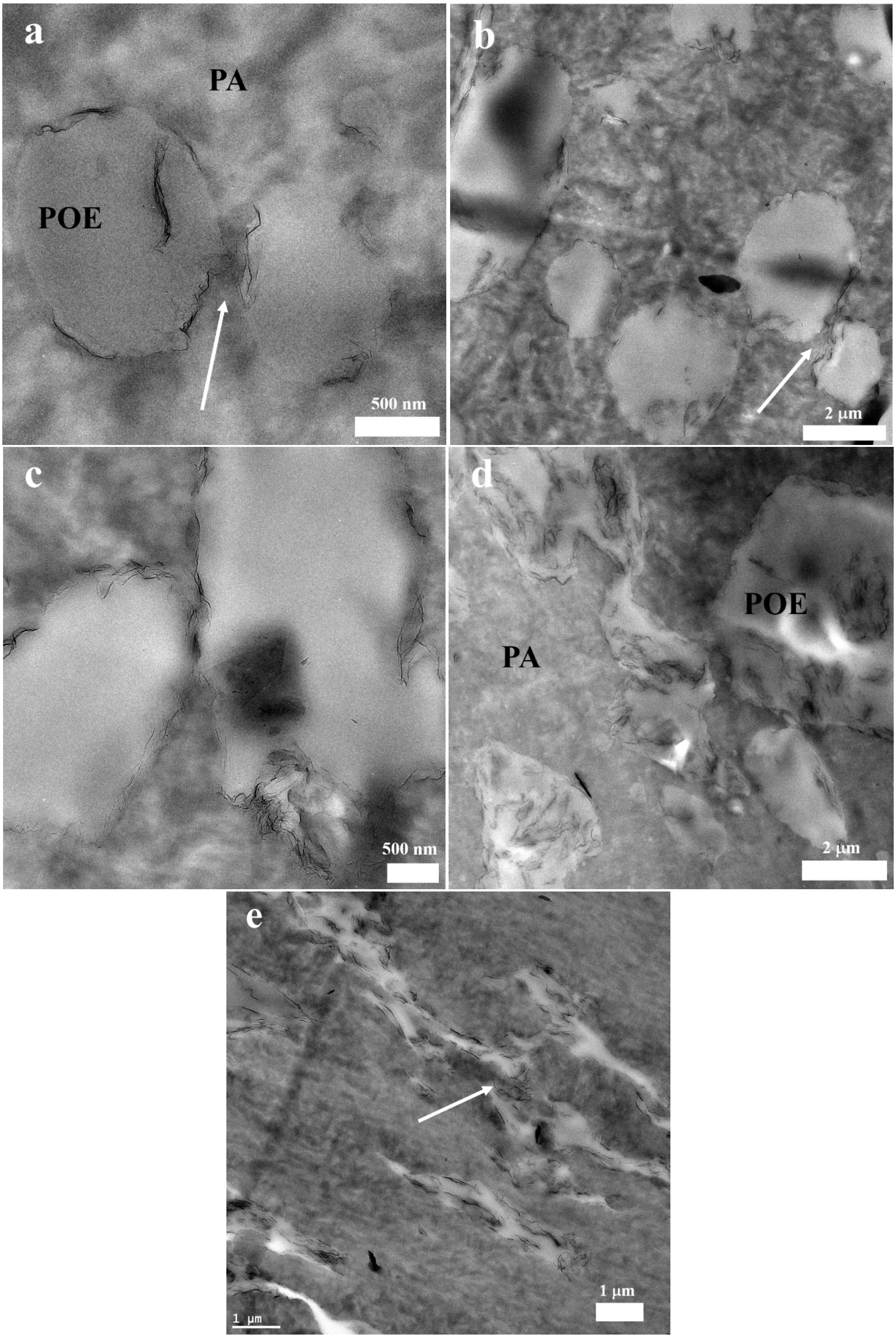
a
PA
POE
500 nm
b
2 μm
c
500 nm
d
POE
PA
2 μm
e
1 μm
1 μm

Figure 4-3. TEM images of nanocomposites annealed under SAOS for: 80-20-0.5 at time=0 (a), 80-20-0.5 at time=34min (b), 80-20-0.5 at time=2 hours (c), 80-20-1 at time=2 hours (d), 80-20-1.5 at time=0 (e). The white arrows indicate graphene bridging between neighboring domains.

In order to evaluate the 3D continuity of the POE phase in our materials, solvent extraction was performed using samples that were not annealed. The neat blend and the 80-20-0.5 system disintegrated in the solvent, indicating a discontinuous morphology. The samples containing more than 1 wt% graphene remained self-supporting after 2 days, thus indicating continuity of POE phase (Fig. S7-10). Solvent extraction was also performed on the 80-20-0.5 system after two hours of annealing under SAOS. Interestingly, this sample was self-supporting, confirming the development of a co-continuous morphology during annealing under SAOS.

In Fig. 4-4, we present a mechanism for microstructural development during annealing under SAOS based on our observations of morphological evolution. The presence of graphene at the interface and inside the POE phase increases the lifetime of domain elongation during compression molding and annealing. At 3% of graphene, however, the formation of a stiff graphene structure inside the POE domains reduces the deformability of the domain and also decreases the coalescence rate. We believe that the graphene bridging between domains along with long shape relaxation times are the main factors promoting the interconnectivity of the POE phase.

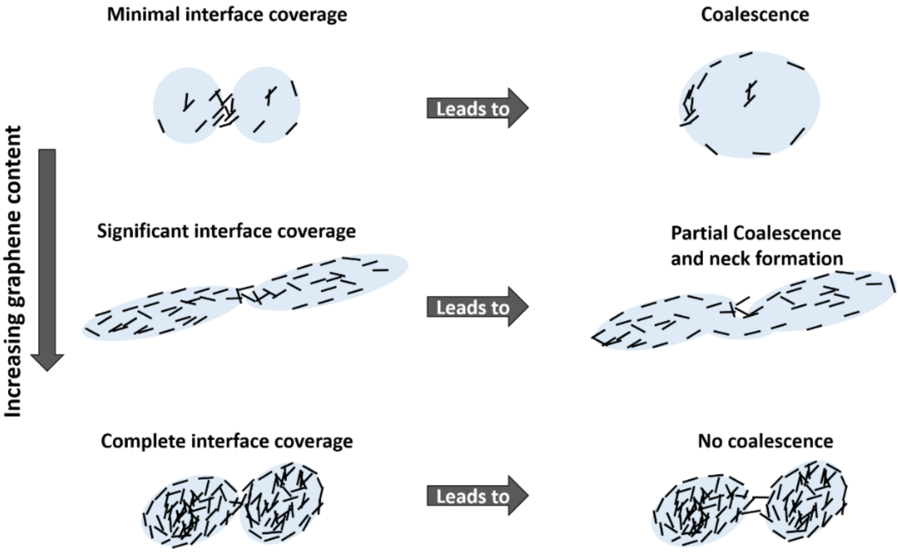

Figure 4-4. Schematic representing the morphological evolution of nanocomposites after compression of samples in the rheometer and under SAOS with increasing graphene content.

4.4.2. Rheological evolution

Next, we consider the evolution of the dynamic properties during the time sweeps (Fig. 4-5). In order to better compare the different systems, the storage modulus (G'(t)) is normalized with the storage modulus point at time 1min (G'(1)) shown in Fig. 4-5-b.

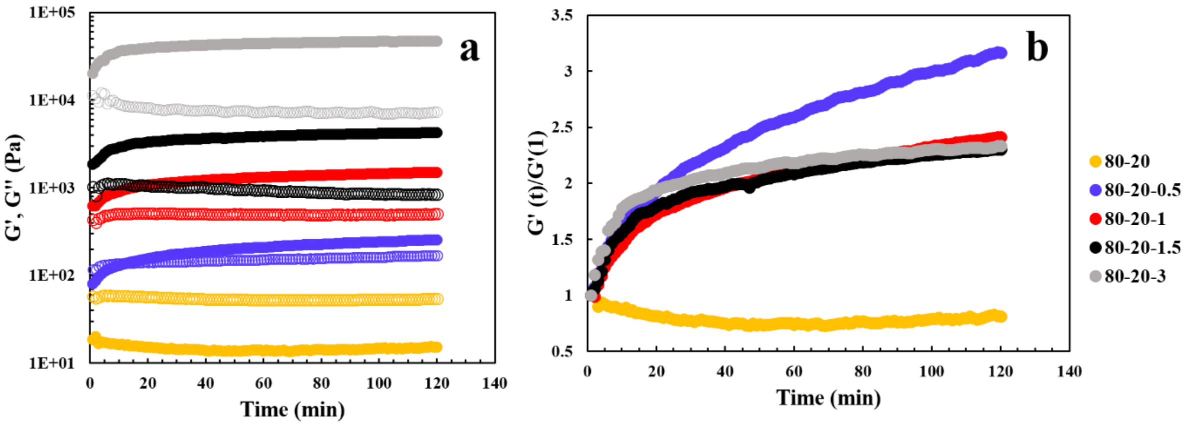

Figure 4-5. Evolution of viscoelastic response of samples during annealing at 0.1 rad/s. (a) Original dynamic modulus data and (b) normalized storage modulus. The filled and unfilled symbols in (a) are storage and loss modulus, respectively.

In the case of neat blend (Fig. 4-5b), the storage modulus decreases during annealing and attains an equilibrium value after approximately 60 minutes.

In the case of nanocomposites (Fig. 4-5b), the storage modulus increases during annealing under SAOS. A sharp increase can be observed in the first 30 minutes of annealing followed by a slower, linear increase at longer times except for 80-20-0.5.

This behavior is also observed in binary systems (one polymer plus nanoparticle) particularly above the rheological percolation threshold and is attributed to the rearrangement of nanoparticles[106, 107]. In ternary systems (polymer blends with nanoparticles), morphological evolution can also have an impact on the storage modulus [108]. In the case of a co-continuous morphology with graphene at the interface, Bai et al showed that the coarsening of morphology leads to the formation of a stiffer 3D structure of graphene giving rise to an increase in elasticity[3].

Our TEM imaging shows that during the annealing the interfacially localized graphene, remains at the interface (Fig. 4-3). This can be explained by comparing the thermal energy with the energy required for removing one graphene sheet from the interface to components (See supporting information).

Considering that the interfacially absorbed nanoparticles remain at the interface at least when they are not close to other domains, the continuous increase in the storage modulus for the 80-20-0.5 system is consistent with the formation of droplet clusters and the rearrangement of graphene at bridge points. For this system, it takes approximately 15 minutes for the storage modulus to cross the loss modulus (Figure 4-5a), which is the sign of formation of percolated structure of graphene. The materials with higher graphene contents are already in this state from the beginning of the time sweep.

With increasing graphene content, the linear increase in storage modulus starts at an earlier time and its slope decreases (Fig 4-5b). This is due to: (i) increased morphology stability (consistent with stable characteristic length Fig. 4-1b) and (ii) a slowing of the graphene reorganization. The latter behavior is usually observed in colloidal gels and is known as the "cage effect".

4.4.3. Dynamic viscoelastic behavior

Fig. 4-6 displays the frequency sweep results performed immediately after 2 hours of annealing under SAOS (0.1 rad/s) where the nanocomposites are close to the equilibrium condition and their viscoelastic functions do not change with time.

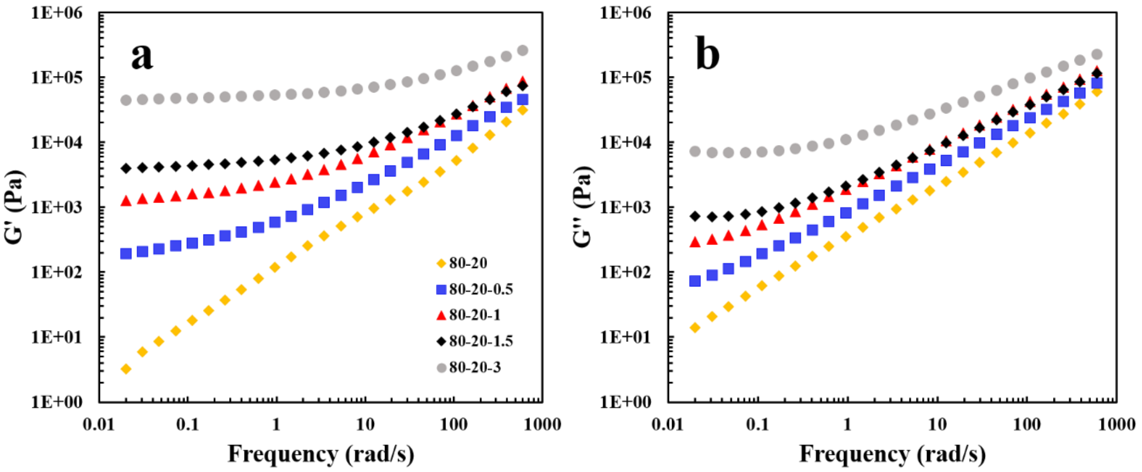

Figure 4-6. Frequency dependence of: storage modulus (a) and loss modulus (b) for different blends.

While the neat blend is predominantly viscous, we observe a strong solid-like behavior in the case of the nanocomposites. We propose that this indicates that the viscoelastic response of the nanocomposites is governed by the percolated graphene structure. This can be tested via the two-phase model; if it applies then interfacial elasticity has a negligible effect and the low-frequency plateau is governed by a percolated graphene structure.

In the two-phase model, the linear viscoelastic behavior of percolated nanocomposites is divided into the viscoelastic response of the polymer(s), at high frequencies, and the elastic behavior of percolated-nanoparticle structure, at low frequencies [109]. This model is shown by the dashed lines in Fig. 4-7a.

With the two-phase model, it is possible to achieve master curves for storage and loss moduli with two shift factors: (i) a vertical shift factor, $b(\varphi)$, indicating the dependence of the stiffness of the nanoparticle network on nanoparticle volume fraction, and (ii) a horizontal shift factor, $a(\varphi)$, accounting for the frequency below which the viscoelastic response is dominated by the nanoparticle network.

Here, we followed the procedure proposed by Fillipone et al to build the master curve [110, 111] (Fig. 4-7). Note that we used the frequency sweep response of the neat 80-20 sample with the same thermal history (after 2 hours of annealing) as the basis for the estimating the shift factors (detailed steps are provided in the supporting information, Fig.S7-12). In spite of having different blend morphologies/interfacial areas, the storage and loss modulus of all of the nanocomposites superpose onto master curves (Fig. 4-7). In Fig. 4-8, we observe the same power law correlation between the two shift factors and graphene content. Accordingly, the shift factors have a linear relation $b(\varphi)= 656.75\ a(\varphi)$.

According to the two-phase model, at $\omega/a_{\varphi} \sim 1$ the contribution of the graphene 3D network and the polymer constituents to the viscoelastic response are equal. Interestingly, the storage modulus of all the nanocomposites superpose best in this region indicating that the mechanism by which graphene slows the dynamics is independent of phase morphology or graphene content. This is consistent with previous observations for binary systems of polystyrene containing different nanoparticles (spheres, platelets and nanotubes)[110].

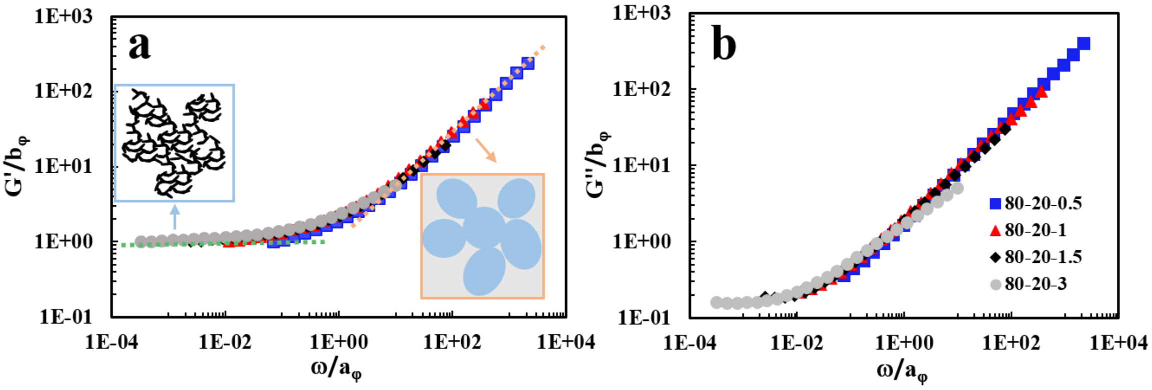

Figure 4-7. Master curves of a) G’ and b) G” produced with two shift factors.

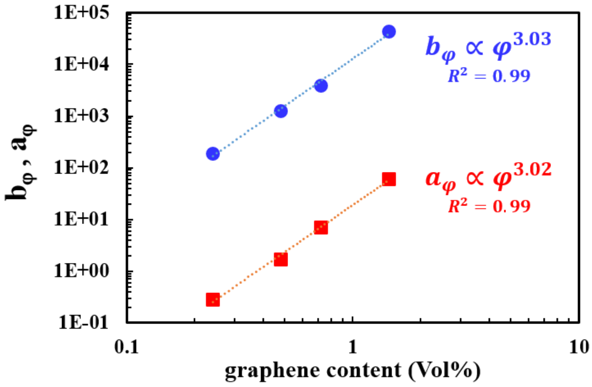

graphene content (vol%/ phr)	a_φ	b_φ= G′at 0.02 rad/s
0.24/0.5	0. 29	192.5
0.48/1	1.7	1280
0.72/1.5	7	3923
1.44/3	62	44675

Figure 4-8. The relation between the vertical (b_φ) and horizontal (a_φ) shift factors and graphene content. The table shows the values for different systems.

Next, we investigate the effect of evolution of microstructure on the viscoelastic response over wide range of frequencies. As explained previously, morphological evolution, i.e. coalescence and shape relaxation, and rearrangement of graphene gives rise to the formation of a stiffer graphene 3D structure increasing the storage modulus. We performed a series of sequential frequency sweeps (starting once the sample is loaded and thermal equilibrium is reached) and then interpolate to calculate the isochronal frequency sweep response [100]. Additionally, from the isochronal frequency curves, we can look at the time dependency of the properties at various frequencies.

First, we study the impact of the evolution of the graphene 3D structure on the storage modulus at different frequencies over time. Fig. 4-9a shows the results for 80-20-0.5 sample (see Fig. S7-13. in the supporting information for the other systems). We performed regular time sweep experiments at constant frequencies of 0.1 and 10 rad/s (Fig. 4-9b) to look at the effect of the thermomechanical history in the rheometer (i.e. sequential frequency sweeps vs time sweeps) at a single frequency in the LVE regime. The evolution of the storage modulus at 0.1 rad/s in the sequential frequency sweeps (SFS) is within the standard deviation of the time sweep results (at 0.1 rad/s) due to sample-to-sample variation (Fig 4-9b). At 10 rad/s, however, the storage modulus in time sweep test is larger than that at the same frequency and time in the sequential frequency sweeps. Note that in the sequential frequency sweeps for approximately 90% of duration of the test, the sample is subjected to a frequency lower than 10 rad/s. Accordingly, we conclude that higher frequencies accelerate the rearrangement of graphene towards the equilibrium which may be due to enhanced diffusion as our group has observed previously in polymeric systems[112, 113]

The evolution over time of storage modulus in the sequential frequency sweeps (Fig 4-9a) is in line with the two-phase model picture that the elastic contribution of the percolated nanoparticle structure decreases with increasing frequency. Note that this occurs because the storage modulus of the polymer melts increases with frequency while the elastic response of the percolated graphene structure is independent of frequency. Accordingly, the change in the stiffness of the graphene 3D structure has a larger relative impact at lower frequencies.

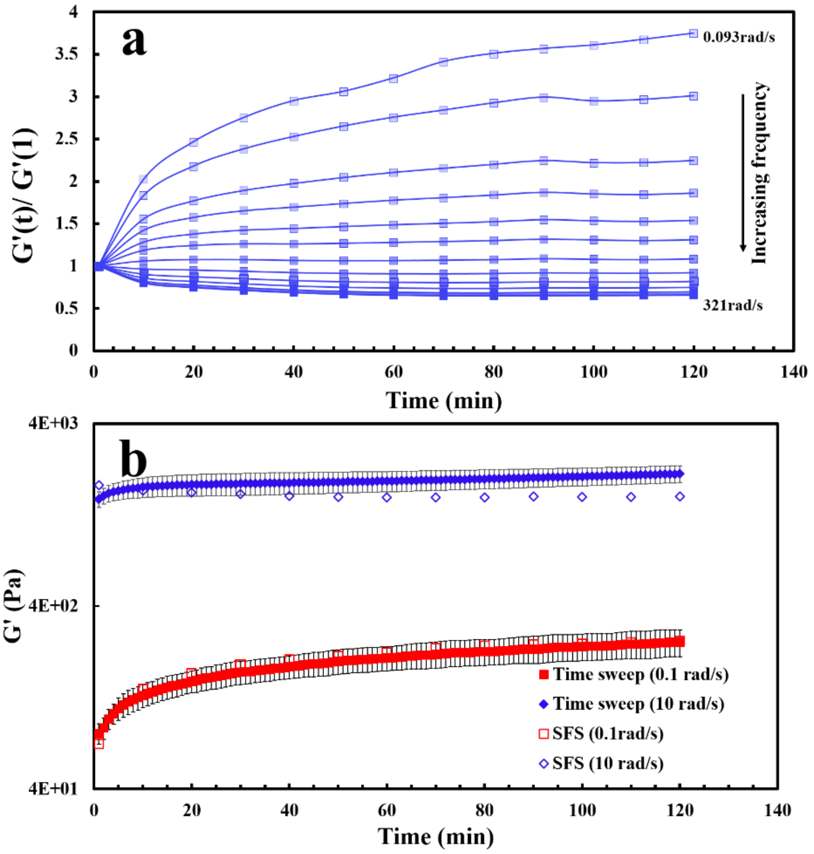

Figure 4-9. a) The evolution of normalized storage modulus over time at different frequencies calculated by interpolation of SFS results, b) Comparison between the

evolution of storage modulus during time sweep at constant frequency and SFS at 0.1 and 10 rad/s, for the 80-20-0.5 nanocomposite.

Next, we investigate the impact of graphene rearrangement on the isochronal frequency sweeps (Fig. 4-10). We note that over time, the low-frequency storage modulus increases, and the plateau broadens towards the higher frequencies. Similar to applying the two-phase model at different graphene contents, the storage modulus superposes onto a master curve by applying vertical and horizontal shift factors at different times (Fig. 4-11a). Using the same shift factors, it is possible to achieve a master curve for the loss modulus (Fig. 4-11b).

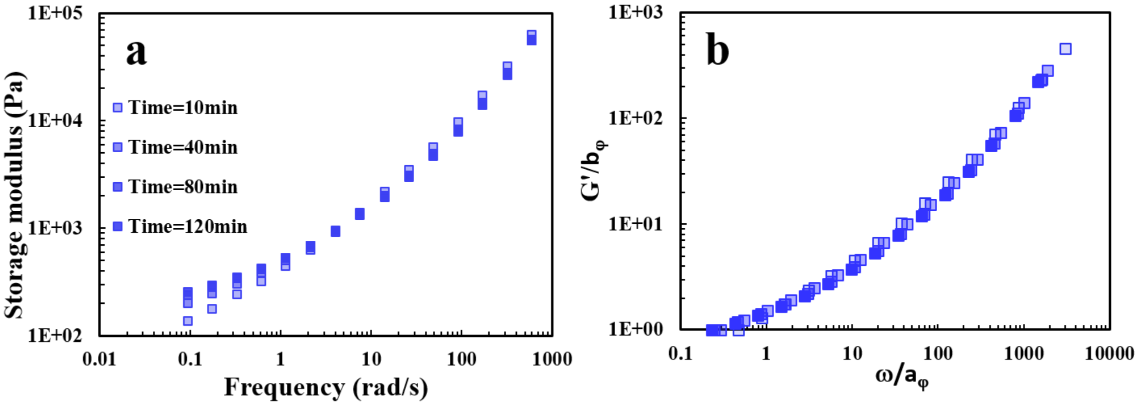

Figure 4-10. a) Isochronal frequency sweeps at different times, b) isochronal frequency sweep shifted both vertically and horizontally, for 80-20-0.5 nanocomposites.

The vertical and horizontal shift factors for isochronal frequency sweeps for different systems at different times are plotted in Fig. 4-11c. The coefficient of proportionality is slightly different from that in Fig. 4-8 for the close to equilibrium condition. We note that this coefficient of proportionality is dependent on the choice of reference storage modulus value for b_{φ}. In both cases, we use the value at the lowest experimental frequency; 0.02 rad/s in the case of the equilibrium condition and 0.0935 rad/s for the isochronal frequency sweeps. Interestingly, the restructuring during annealing under SAOS and graphene content at equilibrium have the same impact on the frequency sweep behavior: both increasing the stiffness of graphene 3D structure and broadening the frequency range over which the elastic response of graphene 3D structure is dominant. Clearly, in both situations we are observing the effect of interconnectivity of the graphene 3D structure.

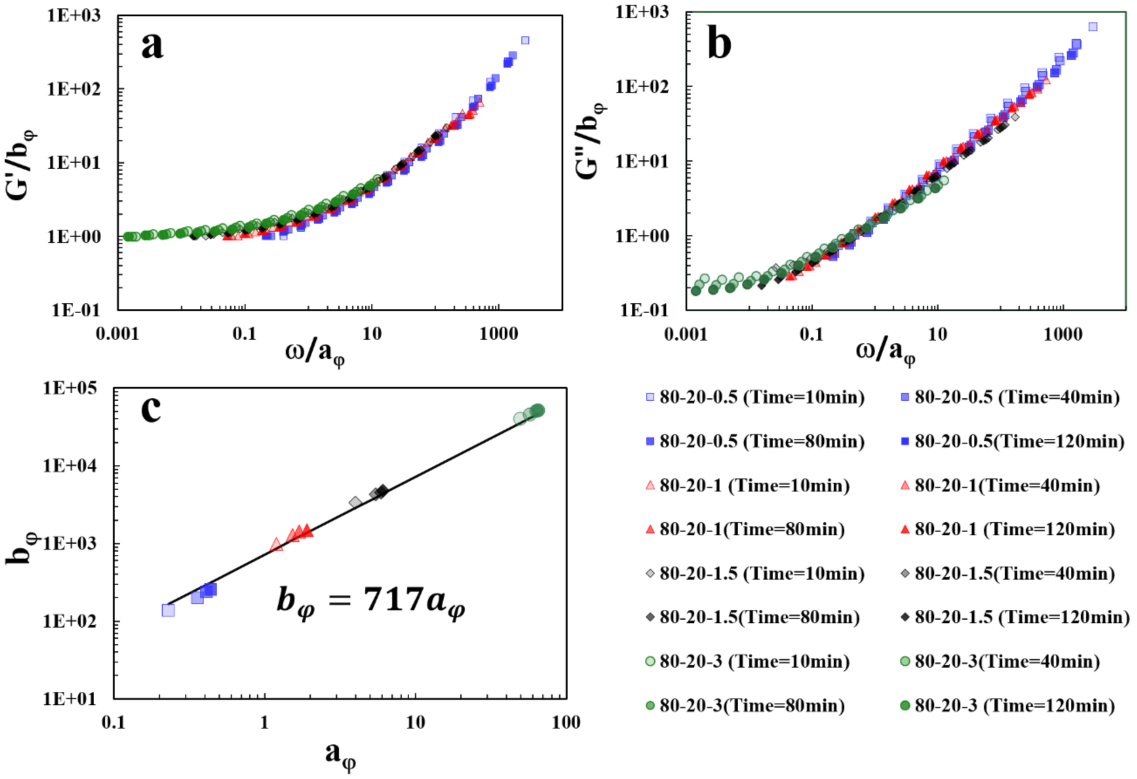

Figure 4-11. Master curves for a) G' and b) G" produced by applying shift factors on isochronal frequency sweep results at different times and graphene concentrations. c) relation between the horizontal and vertical shift factors.

4.4.4. Scaling behavior

Since we have evidence that the rheological response of our materials is dominated by the 3-dimensional structure of graphene, we next characterize the structure using the scaling theory developed by Shih et al[114]. Here we are focusing on the rheological response close to the equilibrium condition (after 2 hours of annealing under SAOS).

This scaling model relates the gel structure of colloidal particles to the fractal dimension of the flocs. According to this model, the limit of linearity in the viscoelastic behavior, γ_c, and the elastic constant, G'_0, scales with the content of filler in a power law fashion. Shih et al showed that the elastic constant of the flocs decreases with increasing floc size. Accordingly, they defined two regimes: At low nanoparticle content, in the “strong-link regime”, the floc exists as a big tenuous structure and the link between the flocs (inter-floc links) are stronger than the links inside the flocs (intra-floc links). Since the properties of the macroscopic structure are governed by the weakest factor, i.e. the intra floc links, the limit of linearity decreases with particle volume fraction. At high nanoparticle content in the “weak-link regime”, the elastic properties are dominated by the inter-floc links, which are weaker than the intra-floc links, and the limit of linearity increases with the volume fraction.

The viscoelastic response of our nanocomposites follows the strong-link regime scaling theory (Fig. 4-12) indicating that the elastic properties are governed by intra-floc links. In order to have a better comparison in this figure, the storage modulus is normalized by the modulus at strain= 0.01%. Here the limit of linearity was chosen based on the strain at which the G' (γ) at 1 rad/s decreases to 90% of its initial value. For the elastic constant, G_0', we use the value of the storage modulus at the frequency of 0.02 rad/s and γ_0 within the LVE domain (note that $G_0' \sim b_\varphi$, Fig. 4-8).

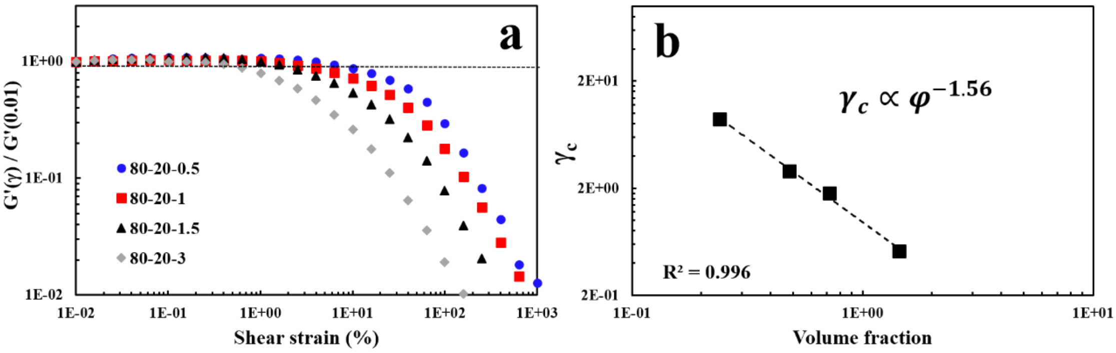

Figure 4-12. Application of scaling theory of Shih et al: normalized storage modulus as a function of strain (a), scaling behavior of critical strain (b).

In the strong-link regime, the fractal dimension of the flocs (d_f) and that of the effective backbone of the flocs (x) can be calculated by combining the following scaling relations[114]:

$$\gamma_c \propto \varphi^n \propto \varphi^{-(1+x)/(3-d_f)} \quad (4\text{-}5)$$

$$G_0' \propto \varphi^v \propto \varphi^{(3+x)/(3-d_f)} \quad (4\text{-}6)$$

Applying equations 4-5 and 4-6, we get 1.64 and 1.12 for d_f and x, respectively. The effective backbone of a floc consists of particles inside the floc, excluding the dangling ends or loops which do not contribute to stress bearing. Note that according to this theory, x should be greater than 1, indicating a continuous network of flocs, but less than d_f.

Generally, the value of d_f is considered as a measure of dispersion, i.e. better dispersion results in a lower d_f or a more open structure. Clearly, d_f is dependent on the affinity of nanoparticle with host phase. In our case due to the strong tendency of graphene to agglomerate, we expect a high value of d_f (i.e. a compact structure). However, the value of $d_f = 1.64$ is lower than the values reported for nanocomposites containing platelet particles (Table 4-3). During mixing, typically nanoparticle agglomerates breakup and restructure forming denser structures with higher fractal dimension which are more stable to the applied shear. We believe that the low fractal dimension found here, is due to the localization of graphene at the co-continuous blend interface preventing the restructuring of graphene to denser agglomerates both during mixing and annealing as compared to binary systems.

Table 4-3. The fractal dimensions of nanocomposites containing particles with platelet geometry.

Material system	Phase morphology/ Nanoparticle location in the blend	Estimated fractal dimensions by rheology		reference
		d_f	x	
PA6/POE/TRG	Co-continuous/interface	1.64	1.12	This study
PS/PMMA/clay	Droplet matrix/Interface	2.19	1.3	[111]
PLA/ TRG	n/a	2.2	2.07	[115]
PLA/GNP	n/a	2.34	---	[116]
PS/clay	n/a	2.17	1.3	[111]
PP-g-MA/clay	n/a	1.9	0.6	[117]
PEN/FGS*	n/a	2.04	1.9	[118]

*Functionalized graphite sheet.

The scaling behavior of systems reveal that in spite of different morphologies, i.e. droplet clusters in the case of 80-20-0.5 nanocomposites and interconnected elongated domains at higher content of graphene, the graphene 3- dimensional structure follows the scaling theory indicating that the structure of graphene consists of self-similar patterns that grow with increasing graphene content independent of blend phase morphology. This is consistent with the non-homogeneous distribution of POE domains (host phase for graphene) in the case of nanocomposites. At low graphene contents, although graphene cannot effectively stabilize the morphology, they rearrange during thermal annealing under SAOS primarily due to the compression driving force to attain their ultimate structure. At higher graphene contents, they can stabilize the blend morphology where the assembly of irregular and elongated disperse-phase domains is affected by the self-assembly of graphene. Accordingly, the phase morphology and the nanoparticles have a mutual impact on each other. Although the host phase or the interface provides the scaffold for the nanoparticles, they tend to achieve their desired structure by influencing the morphology.

4.4.5. AC conductivity

Fig. 4-13 shows the real component of the alternating-current (AC) conductivity, $\sigma'(\omega)$, for samples before and after 2 hours of annealing under SAOS. According to the universal dielectric response model (Eqn. 4-7), the AC conductivity is the sum of the low frequency conductivity plateau, $\sigma(0)$, and a frequency dependent term [119].

$$\sigma_{AC}(\omega) = \sigma(0) + A\omega^{s} \tag{4-7}$$

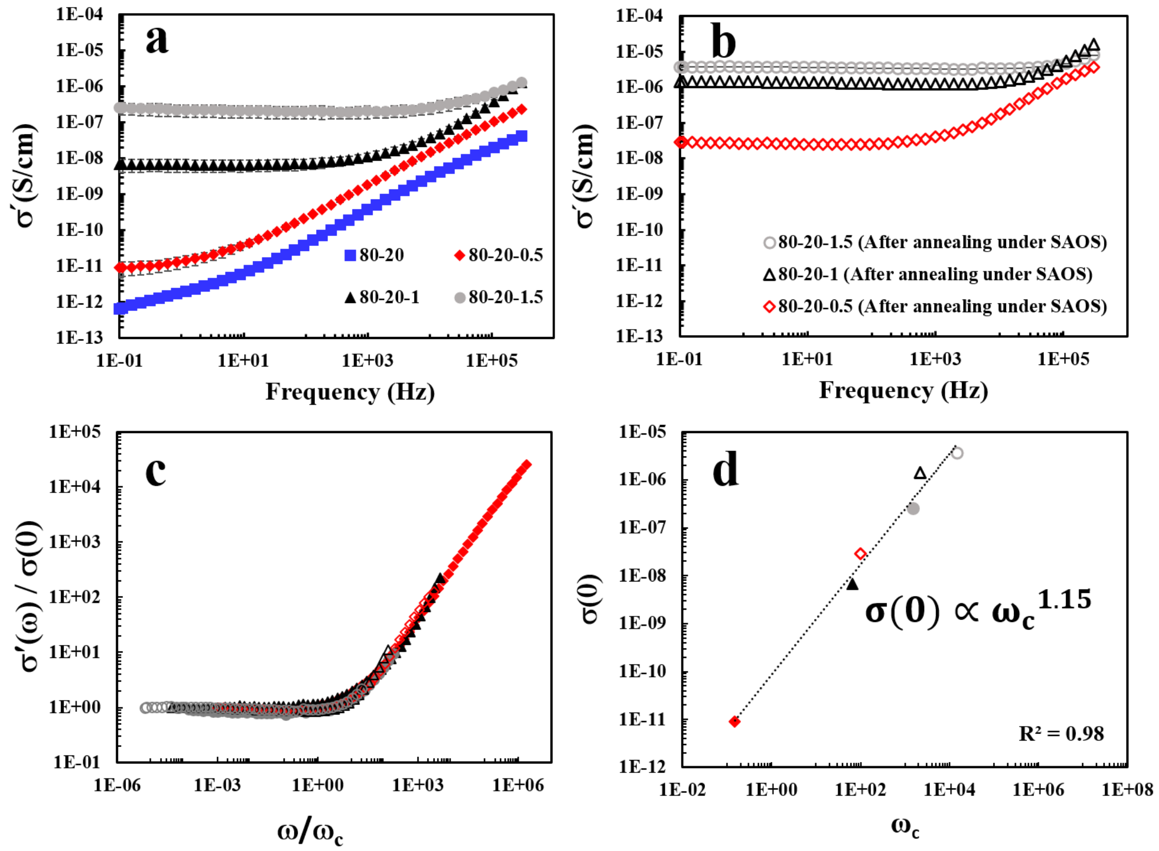

Figure 4-13. AC conductivity for nanocomposites a) real component (σ’) before annealing, b) σ’ after annealing under SAOS, c) master curve of σ’ for nanocomposites with different graphene contents and thermo-mechanical history, d) correlation between the critical frequency and $\sigma(0)$.

Here, A and s are constants which depend on temperature. Kilbride et al related the critical frequency, ω_c at which the transition between the plateau region to the frequency dependent region occurs, to the correlation length of the nanoparticle 3D structure [120]. The correlation length,ζ, decreases with increasing number of connections in the structure. They argued that at ω_c, charge carriers travel a distance on the order of the correlation length providing a link between the transition frequency and the structure of 3D network.

With increasing graphene content, $\sigma(0)$ increases and the plateau broadens toward higher frequencies (Fig. 4-13a). Annealing has the same impact on electrical conductivity (Fig. 4-13b), indicating that the rearrangement of graphene leads to the formation of new contacts between the particles and thus a decrease in the correlation length of percolated structure [120]. In the case of the 80-20-0.5 system, $\sigma(0)$ increases by approximately 4 orders during annealing, indicating a significant decrease in the graphene percolation threshold. The increase in $\sigma(0)$ and ω_c during annealing decreases with graphene content. This occurs because the rearrangement of graphene is hindered due to morphological stability and the compact graphene structure at higher graphene content. We note that these behaviors are similar to those observed in the viscoelastic response.

Interestingly, also like the rheological response, it is possible to achieve a master curve for AC conductivity of all the nanocomposite systems (with different graphene content and thermo-mechanical history) by applying vertical,$\sigma(0)$, and horizontal, ω_c, shift factors (Fig. 4-13c). Here, the horizontal shift factor, ω_c, was estimated as the frequency at which the AC conductivity reaches 1.1 $\sigma(0)$ [120]. Fig. 4-13d, shows the power law correlation between $\sigma(0)$ and (ω_c) which is observed in other carbon-based nanocomposites such as those containing CNT[121]. We note that the AC conductivity of our samples are measured in the solid state, nevertheless due to the very low crystallinity of the POE phase, we expect that solidification does not significantly alter the arrangement of graphene.

4.5. Conclusion

Morphological evolution and its correlation with the rheological response and electrical conductivity of PA6/POE (80/20) blends containing different contents of graphene were investigated during annealing under SAOS and quiescent conditions. It has been shown that the compression force applied on the specimens before applying the SAOS elongates the minor phase domains and decreases the number of discrete domains in the system. This compression force promotes coalescence during the first 30 minutes of annealing under SAOS. This is more pronounced in the case of nanocomposites due to the slow shape relaxation and graphene bridging. Graphene bridging eventually leads to the development of a fractal-like structure for the POE phase (host phase for graphene).

Our results show that there is a considerable difference between the phase morphology and its evolution in the rheometer where the sample is subjected to a compression force during sample loading followed by SAOS and quiescent conditions, especially for nanocomposites. Accordingly, the effect of sample loading in the rheometer should be taken into account to have an accurate correlation between phase morphology and rheological response.

Morphological evolution and graphene rearrangement in the rheometer give rise to an increase in elasticity over time. This slows with increasing graphene content. Interestingly, the evolution of elasticity under SAOS is also dependent on the frequency applied during the test even in the LVE region.

Applying the two-phase model revealed that the LVE response of the nanocomposites close to the equilibrium condition is primarily governed by the 3D network of graphene. Analysis of isochronal frequency sweeps illustrates that the restructuring during annealing has the same impact on the viscoelastic response of nanocomposites as graphene content. The same behavior is observed in the AC conductivity allowing us to construct a master curve for different nanocomposites with different graphene content and thermo-mechanical history. These observations indicate self-similarity in the graphene structure. We note that this important result has only previously been observed in binary polymer nanocomposites. Our results demonstrate that such a master curve can be produced for ternary systems as long as the nanoparticle 3D structure has a larger impact on the viscoelastic response that the interfacial tension between the two polymers.

The linear and non-linear viscoelastic response of our material obeys the fractal scaling theory, confirming that the graphene 3D structure consists of self-similar flocs which grow with increasing graphene content independent of phase morphology. We have found a relatively small fractal dimension (1.64) for the graphene flocs which stems from the localization of graphene at the blend interface.

5. Effect of minor phase rheological properties and compatibilization on co-continuity, rheological and electrical properties of PA6/POE blends containing graphene

5.1. Abstract

We investigate the effect of minor phase rheological properties and compatibilizer on the phase morphology and graphene 3D structure in polyamide-6 (PA6)/ polyolefin elastomer (POE) blends. Two different POEs were used as the minor phase (i) a high viscosity POE with a strong shear thinning behavior and (ii) a low viscosity POE with almost Newtonian behavior. It is revealed that in blends containing the low viscosity POE, graphene is better dispersed facilitating its localization at the interface. In the blend containing high viscosity POE with poor graphene dispersion, large graphene aggregates are observed inside the POE phase and less interfacial coverage. Interestingly, graphene induces a co-continuous morphology and electrical and rheological percolation in both systems although at a lower graphene content for the low viscosity system. The LV system exhibits a more interconnected morphology while in the HV system we observe a compact fractal-like POE structure with a lower degree of interconnectivity. Fractal analysis of the graphene 3D network (based on the rheological characterization) is correlated with the higher degree of connectivity of graphene 3D structure in the LV system. The 2D fractal dimension of the POE domains (host phase for graphene) is in line with the fractal dimension of the graphene flocs indicating that the graphene flocs influence the blend morphology. The addition of compatibilizer to the HV system, results in a lower degree of connectivity of the POE domains subsequently leading to a lower electrical conductivity as compared to the uncompatibilized system.

5.2. Introduction

Co-continuous morphology has received great attention in designing electrically conductive nanocomposites due to the double percolation concept allowing one to considerably reduce the percolation threshold of conductive filler in polymer blends[3, 79] However, co-continuity occurs only over a narrow range of composition, which limits the achievable properties. It is possible to stabilize the morphology and achieve co-continuity over a wider range of composition by the addition of nanoparticles [14, 32, 87]. The impact of nanoparticles on the blend morphology is governed by factors such as their location in the blend, geometry and networking ability [26, 33, 35, 37, 75].

Generally, nanoparticles tend to be localized where they minimize the free energy of the system determined by the interaction of the nanoparticles with each constituent. Kinetic factors such as particle geometry[63], shear force[122], viscosity ratio[65] and elasticity of components [68], may prevent the nanoparticles from reaching the preferred location during the timeframe of processing. The localization of nanoparticles significantly affects the ultimate morphology of the blend by influencing domain break up, coalescence and shape stability.

The morphology of blends with a droplet-matrix morphology is governed by the rate of droplet break-up and coalescence. Generally, an increase in the viscosity of the matrix decreases the rate of coalescence especially when nanoparticles form a network in the matrix. In addition, nanoparticles can reduce the coalescence rate due to steric hindrance. Both effects result in the refinement of morphology which is more pronounced in the case of nanoparticles with platelet-like geometry[96].

The impact of nanoparticles localized inside the dispersed phase or at the interface on the morphology is more complicated since they may influence the breakup and coalescence rate differently. During mixing, the dispersed phase domains elongate due to the flow field leading to an increase in the interfacial area, which is thermodynamically unfavorable. These elongated domains, may break up via the Rayleigh instability or retract back to a spherical shape. The presence of nanoparticles inside the dispersed phase domain increases the critical aspect ratio for droplet breakup and slows down the relaxation of these domains thus preserving their elongated shape[25]. It has been shown that interfacially adsorbed nanoparticles can stabilize the morphology more effectively in comparison to nanoparticles which are located inside the dispersed phase domains due to an increase in interface elasticity [30]. In addition, interfacially adsorbed nanoparticles also reduce the interfacial tension between the polymer phases [26, 28, 54] decreasing the driving force that tends to retract the elongated domains back to a spherical shape. Both factors result in an increase in shape stability.

Li et al proposed potential mechanisms for the formation of co-continuous morphology in binary blends by comparing the thread and droplet lifetime during mixing[123]. They argued that in the case of more stable threads where the thread lifetime is longer than the droplet lifetime, co-continuity is formed by “thread-thread coalescence” decreasing the onset of co-continuity of minor phase as compared with “droplet-droplet coalescence”[123]. Additionally, they revealed that co-continuity is possible over a wider composition window in the case of thread-thread coalescence. Accordingly, the localization of nanoparticles in the dispersed phase or at the interface can reduce the required minor phase volume fraction for co-continuity by increasing the lifetime of elongated domains during processing provided that the elongated domains coalesce with one another to form a continuous structure.

The impact of nanoparticles on the coalescence rate is less well understood. Nanoparticles at the interface can have a shielding effect reducing the coalescence rate[24, 56]. On the other hand, there is some evidence that nanoparticle bridging between the domains promotes coalescence by increasing the contact time between the domains[105]. This usually happens when the nanoparticle has greater thermodynamic affinity towards the matrix.

We have previously shown that graphene can induce a co-continuous morphology in PA6/POE blends with asymmetric composition (80/20). In this study, we investigate the effect of the rheological properties of the minor phase and compatibilizer on graphene-induced co-continuity and electrical properties. Although there is a relatively good understanding about the impact of rheological properties of minor phase on the phase morphology of binary polymer blends, this effect has not been explored in binary blends containing nanoparticles. In addition, we examine the correlation between the morphology and graphene 3D structure by the fractal analysis. We find that the fractal dimension of the nanoparticles can give us information about the phase morphology.

5.3. Experimental section

5.3.1. Materials

A commercial grade of PA6 (Tecomid NB40 NL E supplied by Eurotec Co.) was used as the matrix. Two POE resins with different melt flow indexes were used: (1) a low viscosity POE with MFR 35 g/10min (190°C, 2.16Kg) (TAFMER DF 7350 supplied by Mitsui Chemicals Group) and (2) a high viscosity POE with MFR 5 g/10min (190°C, 2.16Kg) (LC 670 supplied by LG Chem Co). A commercial grade of polyolefin elastomer- graft- maleic anhydride, POE-g-MA, (EML 325 supplied by Karangin Co.) was used as a compatibilizer in certain systems. The graphene (N002-PDR, Angstron Materials) consists of nanoplatelets of 1 to 3 monolayers. The nanoplatelets have thicknesses ranging from 0.25 to 2 nm and diameters ranges from 200-4000nm[64].

5.3.2. Preparation of Nanocomposites

PA6 nanocomposites were prepared by melt mixing in a Brabender internal mixer at 60 rpm and 240°C. Prior to compounding, PA6 and graphene were dried at 80°C for 24 hours under vacuum. All the blends were prepared by POE/graphene master batch as follows: POE and graphene were melt mixed for 8 minutes to prepare a master batch containing 15wt% graphene. The POE master batch was then melt mixed with neat POE and PA6 for 7 minutes. In the case of compatiblized blends, the required content of POE-g-MA is added in the second mixing step along with the blend components. Note that in the compatibilized systems the POE content (including that in the POE-g-MA) was maintained at 20%wt. Specimens for all tests were prepared by compression molding at 240℃ under 50 MPa for 5 minutes. The characteristics of our systems are summarized in Table. 5-1.

Table 5-1. Experimental blends and nanocomposites.

Sample code	PA6 content	POE content	POE-g-MA content	Graphene content wt phr	Graphene content Vol%
80-20-HV	80	20	---	---	---
80-20-0.5-HV	80	20	---	0.5	0.24
80-20-1-HV	80	20	---	1	0.48
80-20-1.5-HV	80	20	---	1.5	0.72
80-20-3-HV	80	20	---	3	1.44
80-20-HV (3%GMA)	80	17	3	---	---
80-20-HV (5%GMA)	80	15	5	---	---
80-20-1.5-HV (3%GMA)	80	17	3	1.5	0.72
80-20-1.5-HV (5%GMA)	80	15	5	1.5	0.72

The same procedure was previously used to prepare equivalent uncompatibilized blend and nanocomposites with POE having lower viscosity [99] and the phase morphology and properties of these systems are compared in this study. We use the term “high viscosity system (HV)” for the blend containing high viscosity POE and “low viscosity system (LV)” for the blends containing low viscosity POE. Fig. 5-1 shows the linear viscoelastic response of the blend components as a function of frequency.

The complex viscosity of POE-LV is roughly independent of frequency with a low storage modulus, i.e. it is essentially Newtonian. Assuming the validity of the Cox-Merz rule ($\eta(\dot{\gamma}) = |\eta*(\omega)|$ where $\dot{\gamma}=\omega$), we can say that viscosity of the POE-HV exhibits significant shear-thinning at high shear rates. Similarly, the POE-g-MA displays shear thinning behavior. In contrast to LV and HV POE, there is no Newtonian behavior over the experimental frequency range. The estimated shear rate at 60 rpm in internal mixing is calculated based on the geometry of mixer and shown in Fig 5-1. It is worth noting that the complex flow in internal mixer is not pure shear.

Since the PA component is expected to undergo post condensation and degradation during the mixing and rheological measurements, we included rheological characterization of PA6 that had been processed in the internal mixer at the above conditions for 7 minutes (PA6-processed) in Fig. 5-1. The viscoelastic response of PA6 before processing is provided in the supporting information. Note that while PA6 undergoes thermal degradation during the mixing step (Fig 5-1a and b), the LVE properties are more stable during the time sweep measurement (Fig. S7-14c). Accordingly, PA6 degradation is unlikely to affect our conclusions especially in the case of nanocomposites.

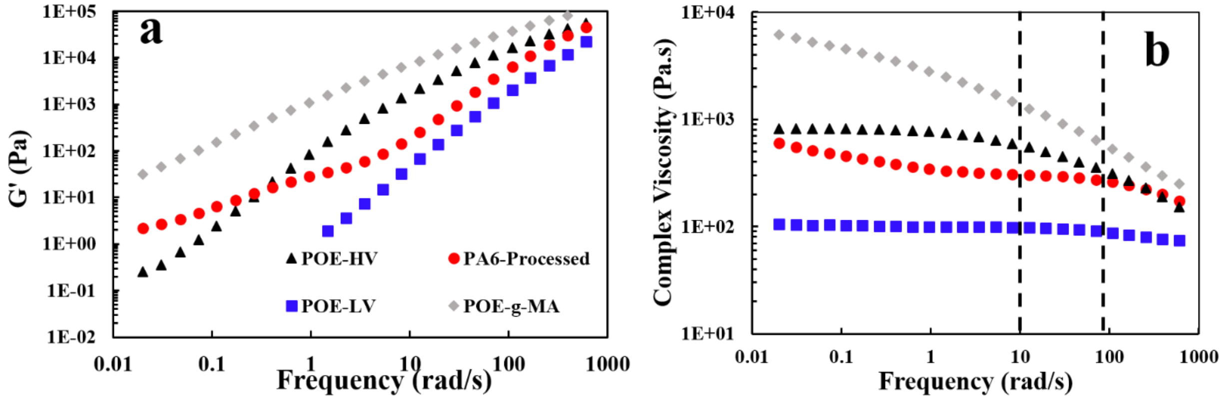

Figure 5-1. Linear viscoelastic properties of the pure components at 240 °C. The dotted line indicates the equivalent minimum and maximum processing shear rate.

5.3.3. FE-SEM: Field Emission Scanning Electron Microscopy

Phase morphology was characterized with a S-3400N, Hitachi system operating at 15 kV. Prior to SEM observation, compression molded samples were cryo-fractured in liquid nitrogen. Then the POE phase was extracted by xylene at 120℃ for 4 hours. The SEM micrographs were analyzed using ImageJ [101] with a manual assist when needed. At least 5 SEM images (1000-2000 domains) from different locations with magnification of 1000x were analyzed for each point. The morphology was analyzed in terms of three parameters:

The first being the characteristic length (ξ) defined as:

$$\xi = \frac{A_{SEM}}{L_{interface}} \qquad (5\text{-}1)$$

where, A_{SEM} and $L_{interface}$ are the area of SEM image and the total interfacial length, respectively. The characteristic length, which is inversely related to interfacial length, decreases with the formation of elongated domains and increases with the coalescence of domains.

The second being the number of discrete domains per 1000 unit area (N) which is sensitive to the continuity of the dispersed phase, defined as:

$$N = 1000 * \frac{Number\ of\ domains}{A_{SEM}} \qquad (5\text{-}2)$$

Finally, the circularity of a domain is defined as:

$$C = \frac{4\pi\,(area)}{(Perimeter)^2} \qquad (5\text{-}3)$$

5.3.4. TEM: Transmission electron microscopy

The localization of graphene was studied by a FEI Tecnai 12 BioTwin instrument at an acceleration voltage of 120 kV. Compression molded samples were cryo-microtomed with a

Leica Microsystems EM UC7/FC7 Cryo-ultramicrotome into sections of 100 nm thickness at -120°C with liquid nitrogen cooling system.

5.3.5. Optical Microscopy

Observations were performed on the cryo-microtomed section (cross section) of specimens by Zeiss Axioplan fluorescence microscope mounted with a Lumenera Infinity 3-1C 1.4 megapixel color cooled CCD camera.

5.3.6. Solvent extraction

In order to investigate the 3 dimensional continuity of the POE phase, compression molded specimens were cut into 10mm x 15mm x 2mm sheets and were placed in 30 mL of formic acid for two days at room temperature to dissolve the PA6 major phase. The solvent was replaced after 24 hours. Blends which were self-supporting after extraction of the PA6 phase were considered to be co-continuous. For blends which collapsed or broke apart in the formic acid, fresh specimens were subjected to POE phase extraction with xylene at 120°C. The solvent is replaced every 8 hours and the weight of the dried sample is monitored until reaching a constant weight. The continuity of POE phase is then calculated by Eqn. 5-4.

$$continuity\ of\ POE\% = \frac{m_i - m_f}{m_i * w_{POE}} \times 100 \tag{5-4}$$

Here, w_{POE} is the weight fraction of POE in samples (20%) and m_i and m_f are the weight of samples before and after of POE extraction, respectively. Reported data are average of 3 repeats.

5.3.7. Rheology

Rheological tests were performed with an MCR 502 rotational rheometer at 240ºC under nitrogen, with parallel plates geometry at a 1 mm gap. Strain sweep tests were conducted to define the linear viscoelastic regime for each blend. Since the rearrangement of particles tends to increase elasticity during the initial stages of the experiment, first, we annealed the samples for 2 hours under SAOS in the linear viscoelastic regime at frequency of 0.1rad/s and then frequency sweep measurements were conducted from low to high frequencies (0.02-600 rad/s). Similarly, strain sweep tests were performed after 2 hours of annealing under SAOS at a frequency of 1 rad/s. Reported data are the average of 3 repeats on different specimens.

5.3.8. Electrical Conductivity

The dielectric properties were measured using a Novocontrol broadband dielectric spectrometer over the frequency range of $10^{-1}\times10^{5}$ Hz under an excitation voltage of $3V_{RMS}$ with parallel brass plated electrodes. The measurements were performed on disc shape specimens with diameter of 25mm and a thickness of 2mm at room temperature. Reported data are the average of 3 repeats on different specimens.

5.4. Result and discussion

5.4.1. Graphene localization and blend phase morphology

The thermodynamic affinity of graphene to the blend constituents has been analyzed by calculating the wetting coefficient in the previous chapter [99]. This analysis shows that graphene, tends to be located at the interface at equilibrium condition. Accordingly, we expect the migration of graphene from POE toward the interface in the second step of mixing. We note that the interfacial tension between PA6/graphene is lower than that of POE/graphene indicating a greater affinity of graphene toward the PA6 major phase.

Fig. 5-2 shows the TEM micrographs of nanocomposites containing 1.5wt% graphene for the HV system, compatibilized HV system and LV system. The dark gray phase shows PA6 phase with a higher density and crystallinity and the white domains are the POE. In the case of uncompatibilized nanocomposites (Fig. 5-2a and 2c), graphene aggregates can be observed primarily inside the POE domains and a small portion of well-dispersed graphene is localized at the interface of components. The graphene dispersion is better in the case of the low viscosity system (Fig. 5-2c). Comparing the uncompatiblized LV and HV systems, more graphene can be observed at the interface of LV system. This is due to the better dispersion in the case of LV system which facilitates the incorporation of graphene at the interface as explained in our previous work[99]. In the case of the compatibilized HV system (Fig. 5-2b) less graphene is located at the interface as compared to the equivalent uncompatibilized system. This is likely due to the presence of reactive compatibilizer at the interface reducing the driving force for graphene localize at the interface.

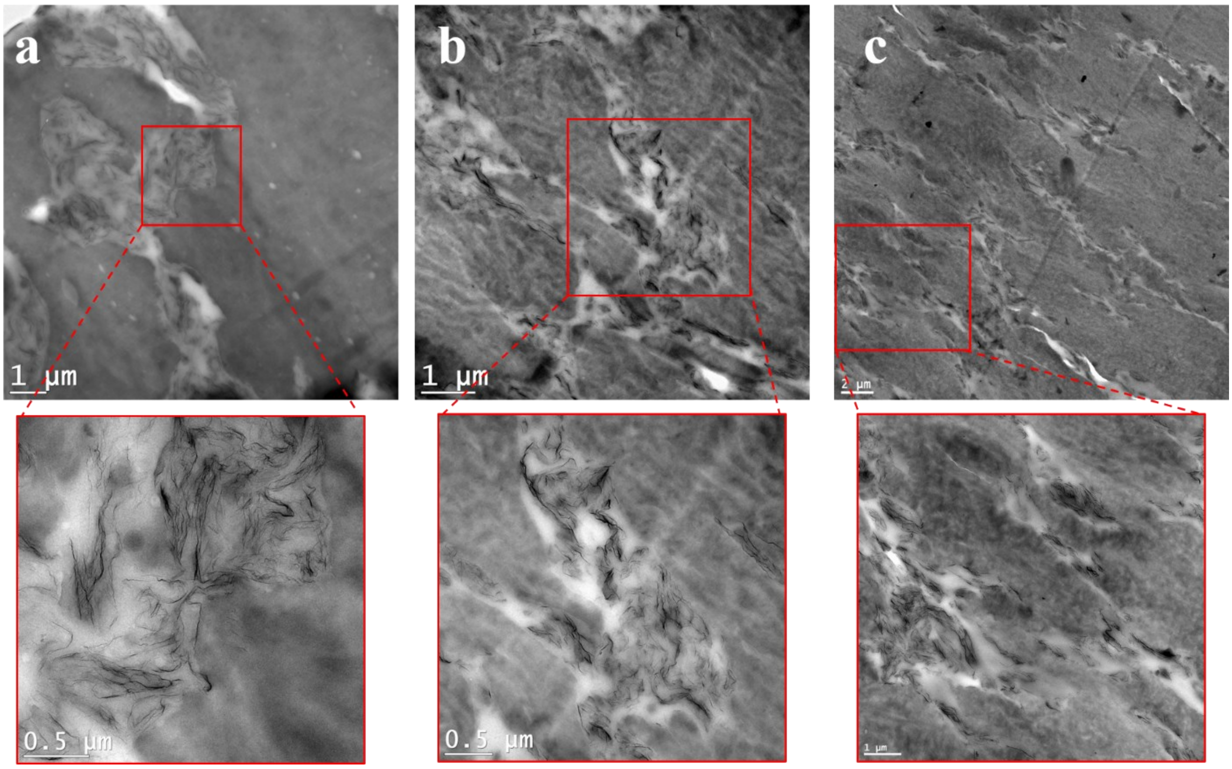

Figure 5-2. TEM images of a) 80-20-1.5-HV, b) 80-20-1.5-HV(3%GMA), c) 80-20-1.5-LV.

Next, we examine the effects of graphene content on the phase morphology of uncompatibilized HV system. Fig. 5-3 shows the SEM images of the blends as a function of graphene content. The neat blend exhibits a typical droplet-matrix morphology in which POE forms the dispersed phase (Fig. 5-3a). In the case of 80-20-0.5-HV nanocomposites (Fig. 5-3b), the presence of graphene inside the POE domains leads to formation of larger, mostly spherical droplets corresponding with lower N and higher ξ (Fig. 5-4). Increasing the graphene content gives rise to formation of larger, elongated domains in 80-20-1-HV and 80-20-1.5-HV nanocomposites resulting in a decrease in N. Note that the characteristic length, ξ, also decreases arising from the elongation of the domains (Fig. 5-4b). Formation of elongated domains is due to the impact of graphene on the elasticity of POE domains stabilizing the elongated domains as explained in the introduction. The circularity distribution and average value are provided in the supporting information (Fig. S7-15). In the case of blends containing 3wt% of graphene, we observe a refinement in the morphology and elongated domains can be observed. At this graphene content it is not possible to quantify the morphology accurately due to the concentration of graphene inside the POE domains.

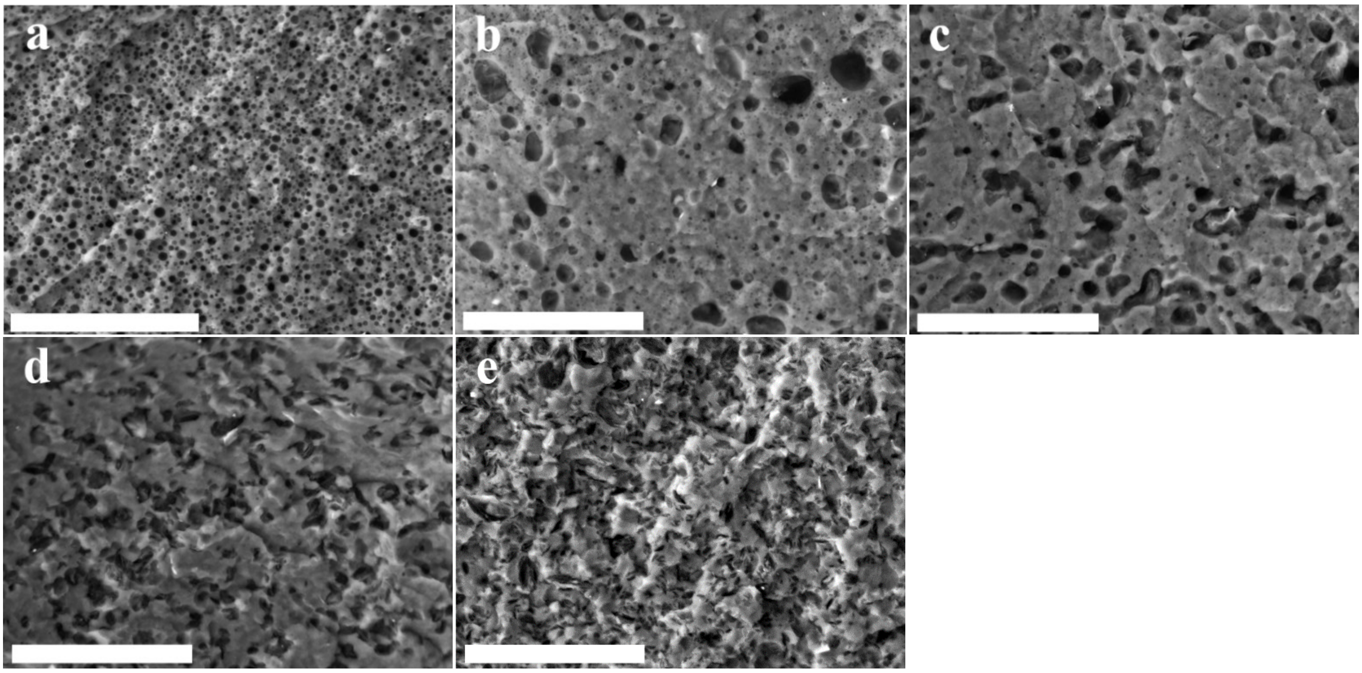

Figure 5-3. SEM images of a) 80-20-HV, b) 80-20-0.5-HV, c) 80-20-1-HV, d) 80-20-1.5-HV, e) 80-20-3-HV. Scale bars correspond to 50 µm.

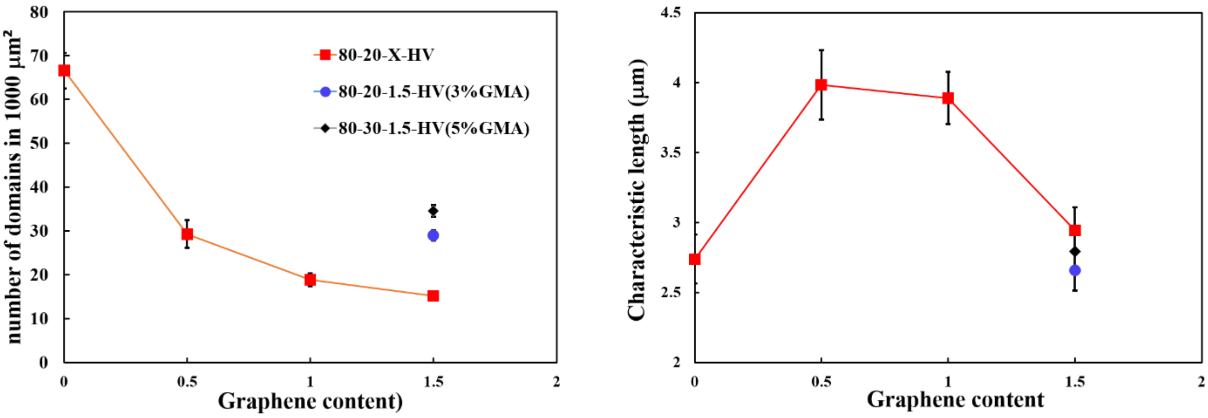

Figure 5-4. a) Number of discrete domains (N) b) characteristic length (ξ) as a function of graphene for compatibilized and uncompatibilized HV system. The lines are guide for the eye.

In order to examine the 3 dimensional continuity of the POE phase at different graphene content, the components were selectively solvent extracted and the continuity of POE phase was calculated as explained in the methods section (Fig. 5-5). The co-continuity increases with increasing the graphene content and the 80-20-1.5-HV and 80-20-3-HV nanocomposites are fully co-continuous which is consistent with formation of elongated domains and our 2D morphological analysis.

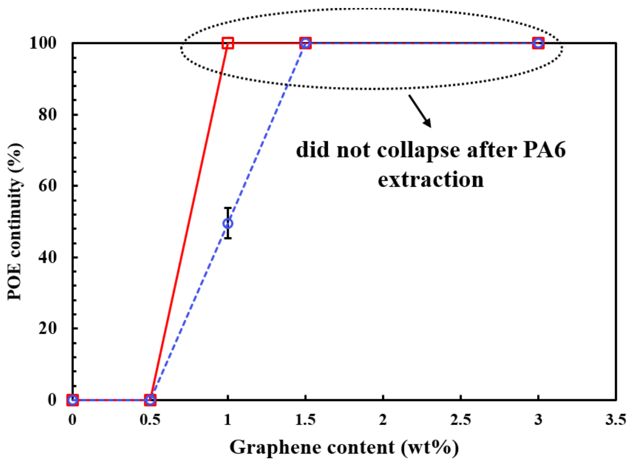

Figure 5-5. 3D continuity of POE phase as a function of graphene content for LV (red line) and HV (dotted blue line) systems. The lines are to guide the eye.

Next, we investigate the impact of compatibilizer on the phase morphology in the HV system. Fig. 5-6 displays the phase morphology for the neat blend and nanocomposite containing 1.5%wt graphene with 3 and 5wt% compatibilizer. In the case of neat blends, we observe a droplet-matrix morphology with POE being the dispersed phase (Fig. 5-6a and b). A sharp refinement in the droplet size can be observed with compatibilization. This is due to the well-known reduction of coalescence arising from the steric hindrance effect of the compatibilizer[124].

Similarly, in the case of compatibilized nanocomposites (Fig. 5-6c and d) the number of individual domains increases with the addition of compatibilizer as compared to the uncompatiblized nanocomposites (Fig. 5-4a). However, in spite of larger N, in the case of compatibilized nanocomposites, more elongated domains can be observed as compared to the uncompatibilized nanocomposites resulting in lower characteristic length (Fig. 5-4b) and lower domain circularity (Fig. S7-15). This can also be appreciated in the TEM images (Fig. 5-2). This shows that although compatibilizer increases the stability of the elongated domains during processing by decreasing the interfacial tension, it prevents coalescence giving rise to an increase in the number of discrete domains. Interestingly, the POE phase in compatibilized nanocomposites containing 1.5%wt of graphene were continuous (they were self-supporting after extraction of PA6 major phase) which is due to the formation of elongated domains inducing the percolation of POE domains.

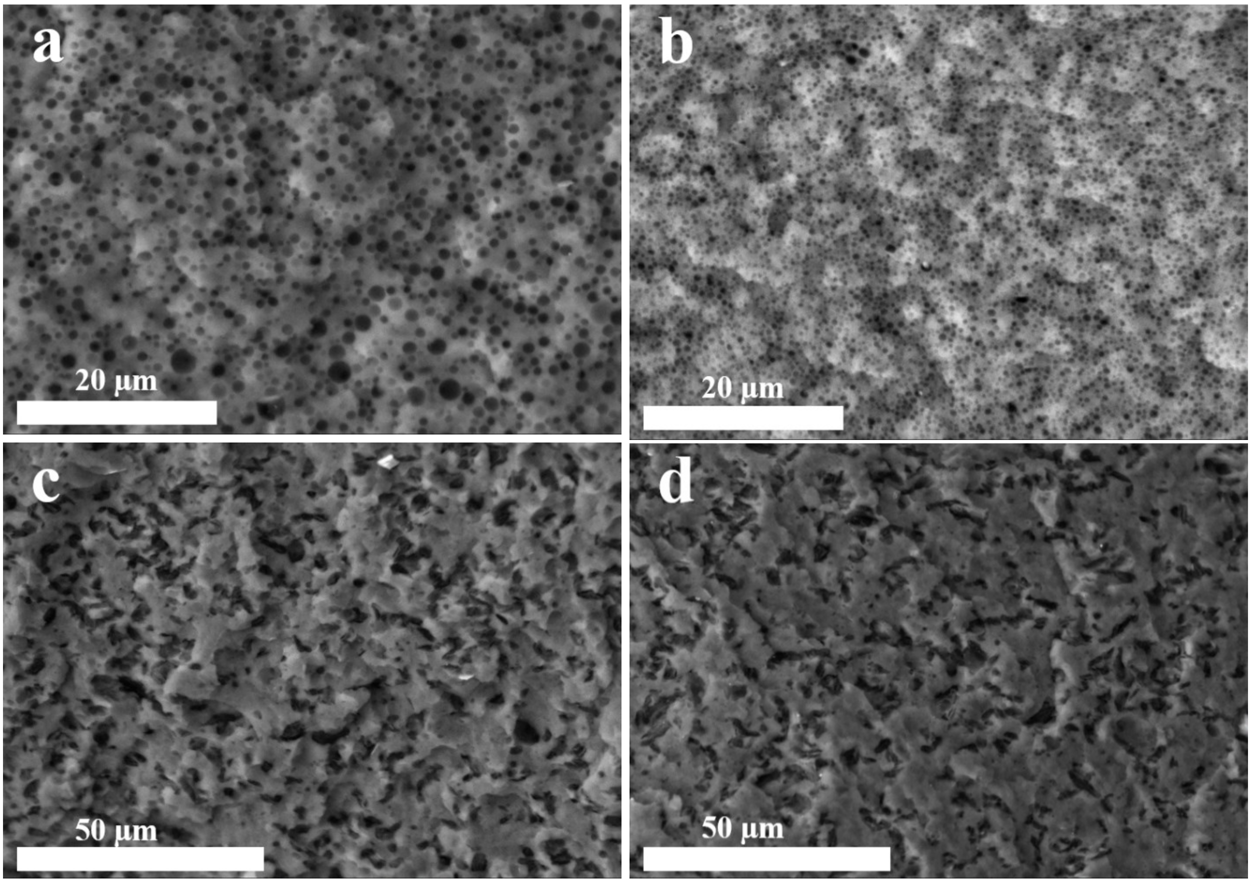

Figure 5-6. SEM images of compatibilized blends a) 80-20-HV(3%GMA), b) 80-20-HV (5%GMA), c) 80-20-1.5-HV (3%GMA), d) 80-20-1.5-HV (5%GMA).

5.4.2. Comparison between the high and low viscosity systems

We previously observed the transition from droplet-matrix to co-continuous morphology in the systems containing low viscosity POE (LV). The FESEM images of LV system can be found elsewhere [99].

Before analyzing the reasons behind the differences in detail, first we highlight the main differences between the microstructure of the two systems: (i) In the case of neat blend, the average droplet diameter (1.47 µm) in HV system is smaller in comparison to that of the LV system (~3 µm [99]). (ii) The formation of elongated domains starts at lower content of graphene in the case of LV system (0.5%wt in the LV system vs 1%wt in the HV system). (iii) In the case of nanocomposites with 1.5%wt of graphene and co-continuous morphology, the LV system has an open structure (interconnected with elongated domains) while the HV system has a compact structure (droplet clusters of slightly elongated domains). Finally (iv) more graphene bridging is observed in the LV system as compared to the HV system. Following is a detailed analysis of the phenomena behind these differences in morphology.

The smaller droplet size in the HV system is expected because it is well known that a smaller droplet size results when the viscosity ratio is close to unity [125]. The viscosity ratio (η_d/η_m) at the processing conditions (shear rate= 90 s^{-1}) are 1.03 and 0.36 for the high viscosity and low viscosity system, respectively.

In both systems, the 3D continuity of the POE phase increases with increasing the graphene content. However, in the LV system, the percolation of POE domains occurs at lower content of graphene (1wt%) as compared to the HV system (1.5 wt%, Fig. 5-5). This is consistent with the formation of elongated domains at lower graphene content in the LV system.

At 1.5%wt graphene both systems have co-continuous morphologies. Optical microscopy was carried out in order to provide a larger scale picture of the blend morphology (Fig. 5-7). Note that the POE domains appear darker due to the localization of graphene inside this component. A co-continuous morphology is observed in both cases: however, there is a significant difference between the morphologies formed. The low viscosity system exhibits an open structure phase morphology with elongated domains (Fig. 5-7a), While in the high viscosity system, the slightly elongated domains aggregate with one another and form droplet clusters with more compact fractal-like structure (Fig. 5-7b).

We note that the quality of graphene dispersion can be inferred by the relative transparency of the POE domains in optical micrographs where the areas which appear darker have denser aggregates [126]. The domains in the LV system are lighter confirming the better dispersion of graphene in this system as observed by TEM images (Fig 5-1).

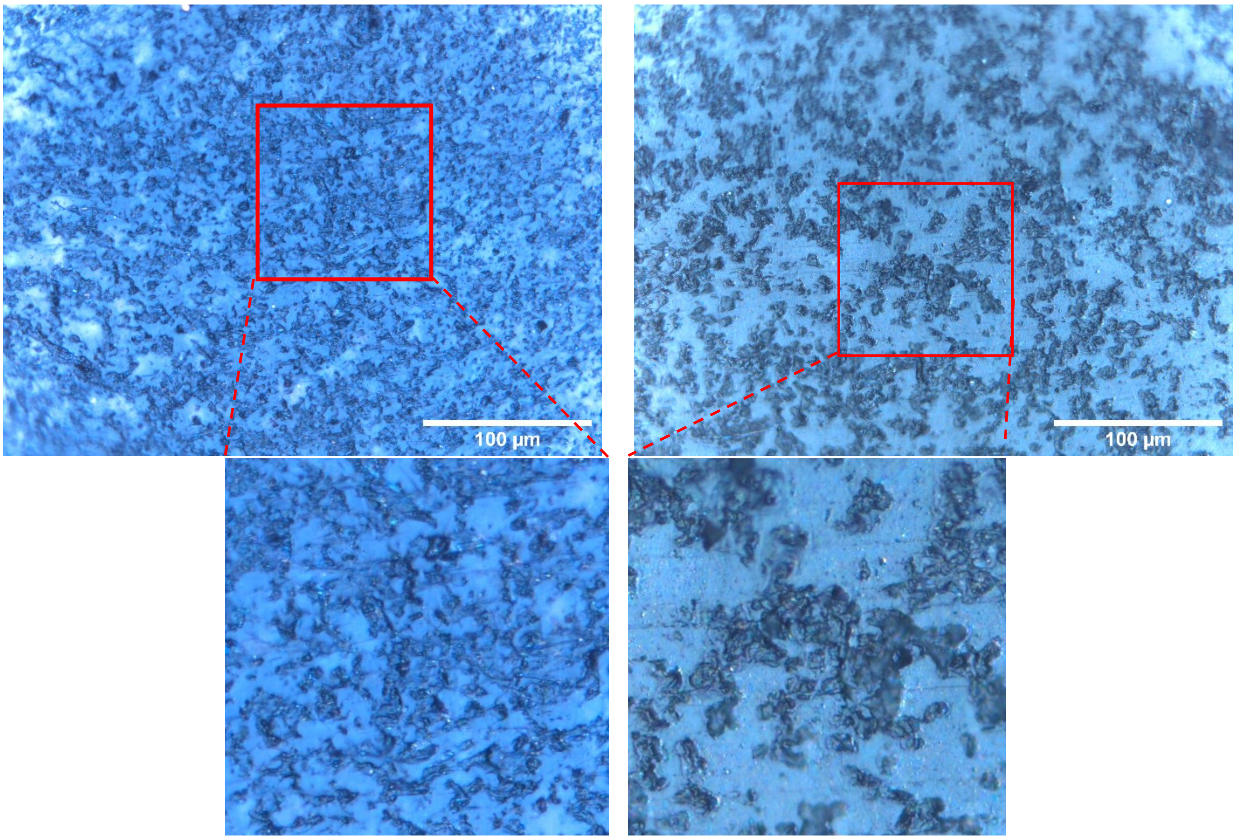

Figure 5-7. Optical micrographs of (PA6/POE/graphene) blends for; a) 80/20/1.5 low viscosity system, b) 80/20/1.5 high viscosity system. Scale bars correspond to 100 µm.

Another difference between these systems is the bridging of graphene between POE domains, which occurs in the low viscosity system (Fig. 5-8a) but not in the high viscosity system (Fig. 5-8b). Note that graphene bridging in LV system was observed at all graphene contents. This leads to a more interconnected morphology with an open structure in the LV system, since the domains stick together via the bridges.

We believe the difference between these morphologies primarily comes from the dispersion of graphene particles. As observed in TEM images (Fig. 5-2), the dispersion of graphene is finer in the case of LV system. This is likely due to the ability of low molecular weight POE to penetrate into the graphene galleries and “peel-off” the graphene sheets more effectively[127]. The good dispersion of graphene particles has 4 main consequences: (i) it increases the deformability of the POE domains, (ii) it enhances the distribution of graphene throughout the POE domains, i.e. graphene will be distributed in a larger number of domains, (iii) it increases the ability of graphene to stabilize the elongated domains, and (iv) it enhances the bridging ability of graphene.

Note that the deformability and formation of elongated domains requires the breakup of graphene structure and aggregates inside the POE domains during mixing. Due to the improved dispersion of the graphene in the LV system, we observe fewer large aggregates which tend to limit the domain elongation (Fig 5-2c). Additionally, the well-dispersed graphene particles better stabilize the elongated domains during processing by localizing at the interface. Accordingly, we observe more elongated domains in LV system.

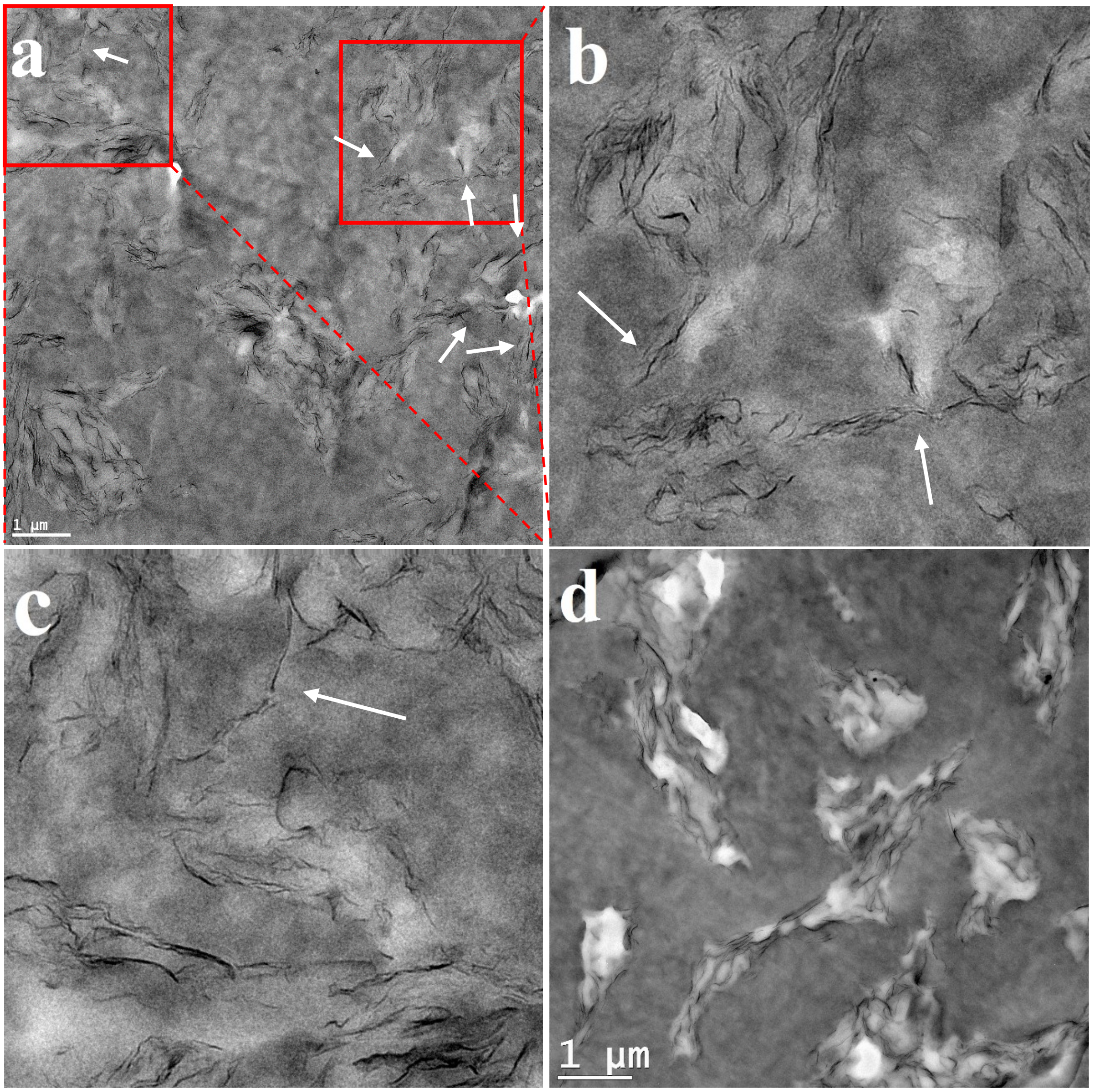

Figure 5-8. TEM images of PA6/POE/graphene blends for: a, b and c) 80/20/3 low viscosity system, d) 80/20/3 high viscosity system. Arrows indicate the bridging of graphene. Note that b and c are enlargements of the indicated areas from a. Figure a is from ref. [99].

5.4.3. Electrical conductivity

The frequency dependence of electrical conductivity,$\sigma_{AC}'(\omega)$, of the HV system is shown in Fig. 5-9a.

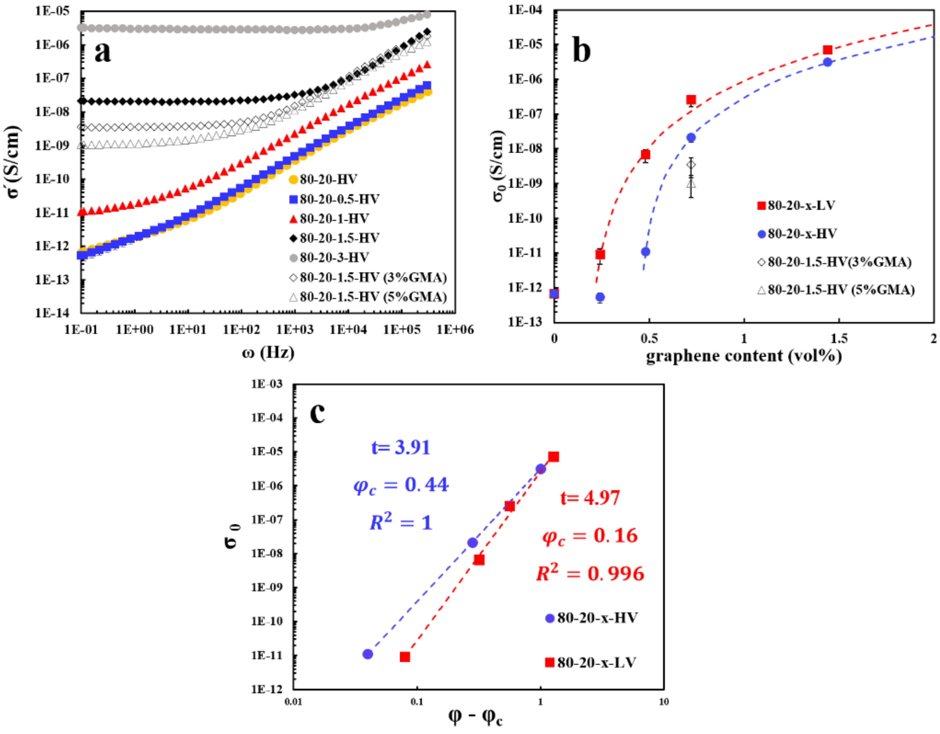

Figure 5-9. a) AC conductivity of uncompatibilized and compatibilized HV system as a function of frequency, b) σ_0 for blends at 0.1Hz for LV and HV blend, c) log (σ_0) versus log ($\varphi - \varphi_c$) and the fit of percolation model to the experimental data.

The addition of 0.5wt% of graphene does not change the $\sigma_{AC}'(\omega)$ over the frequency range investigated here (Fig 5-9a). However, at higher contents of graphene we observe a plateau at low frequencies which broadens toward higher frequencies with increasing graphene content. This plateau at low frequencies confirms the formation of a percolated graphene structure throughout the system.

The connectivity of the graphene 3D structure can be examined by comparing the AC conductivity at low frequencies. Fig. 5-9b shows the AC conductivity of the LV and HV systems at a frequency of 0.1HZ (σ_0). A reduction in σ_0 can be observed with increasing compatibilizer content in the HV system. As shown in Fig. 5-1, the compatibilizer hinders the localization of graphene at the interface. Additionally, we observe an increase in the number of individual domains with increasing compatibilizer content. These factors, decrease the number of contacts between the graphene particles reducing the conductivity. Comparing the LV and

HV systems, we observe that the σ_0 is higher in the case of LV system at all graphene contents. Graphene percolation occurs between the 0-0.24%vol (0-0.5%w) for the LV system, while it occurs between 0.24-44%vol (0.5-1wt%) in the case of HV system. The critical graphene content for percolation can be estimated by the classical percolation theory

$$\sigma = A(\varphi - \varphi_c)^t \tag{5-5}$$

Here, φ is the graphene content, φ_c is the percolation threshold, A is an exponential prefactor and t is the critical exponent. For 3D connectivity in a percolated system of randomly distributed filler, t is expected to be 1.8-2.

The parameters for Eqn. 5-5, determined by linear regression, are shown in the Fig. 5-9c. The percolation threshold for the LV system is significantly lower than that of the HV system. This is in line with the increased connectivity of the elongated LV POE domains. However, the electrical percolation threshold of graphene in both the LV and HV systems are lower than the required graphene content for formation of a co-continuous morphology. This is due to the localization of graphene at the interface and graphene bridging between the neighboring POE domains (in the case of LV system). The critical exponent in both systems, is higher than the universal 3D value, perhaps due to tunneling effect and non-random dispersion, i.e. orientation and aggregation of nanoparticles, and selective localization of graphene in the POE phase. We note that we previously found a higher exponent, t=8.49, and higher percolation threshold, 0.66wt%, for the LV system by fitting the percolation model to DC conductivity[99]. Specifically at 0.5 wt% graphene the $\sigma_0 > \sigma_{DC}$ and at 3wt% of graphene $\sigma_0 < \sigma_{DC}$ while at the intermediate graphene contents $\sigma_0 \sim \sigma_{DC}$. Kilbride et al observed a similar difference between DC and AC conductivity at low carbon nanotube content nanocomposites [120]. They argued that in terms of hopping conduction, DC conductivity is limited by the activation energy barriers throughout the whole network, while in the AC conductivity it is limited by the highest energy barrier over the distance which charge carrier travels in one half period of the electrical field. Accordingly, at the vicinity of percolation threshold, there might be large networks that are not percolated through the system. These networks increases the AC conductivity while they do not contribute to the DC conductivity[120].

5.4.4. Dynamic response

We have previously showed that the elasticity of the nanocomposites containing LV-POE, increases during annealing due to the rearrangement of graphene and evolution of morphology [ref] with the same impact on the frequency sweep response as increasing graphene content.

Accordingly, in order to measure the rheological response of our material at a more stable condition, the samples were annealed for 2 hours under SAOS at 0.1 rad/s prior to the dynamic experiments. The evolution of the viscoelastic response of the HV system is similar to that of the LV system[128].

To better compare the evolution of elasticity during the annealing under SAOS, the storage modulus is normalized by its initial value (Fig. 5-9a). Original data are provided in the supporting information (Fig. S7-16). Here, we summarize the main observations from Fig. 5-9a: (i) in the case of the neat blend the elasticity decreases during the annealing under SAOS due to coalescence-related reduction in interfacial area; (ii) in the case of nanocomposites, the elasticity increases due to the rearrangement of graphene platelets and morphological evolution; (iii) the increase in the elasticity consists of two steps, a sharp increase at early times followed by an almost linear increase at longer times; and (iv) with increasing graphene content, the linear increase in the elasticity starts at an earlier time and the slope decreases.

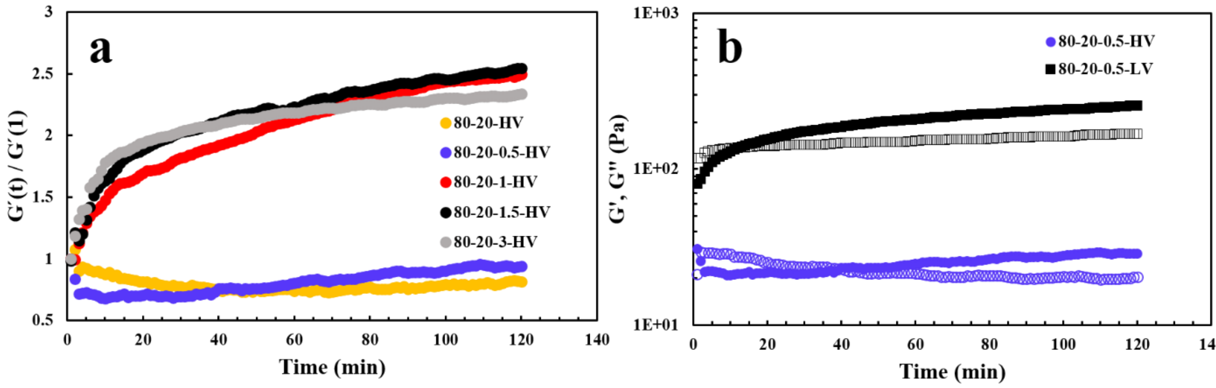

Figure 5-10. a) Evolution of storage modulus during time sweep for HV system, b) evolution of G' (solid symbols) and G" (open symbols) during time sweep for LV and HV systems containing 0.5%wt of graphene.

The main difference between the LV and the HV systems appears with nanocomposites containing 0.5%wt graphene (Fig. 5-9b). In the HV system, the sharp, early stage increase in G' is not observed and the elasticity increases almost linearly from the start of annealing. It takes approximately 40 minutes for the formation of a graphene percolated structure as indicated by the point at which the G' crosses over the G". This time was significantly shorter in the case of LV system (10 minutes) where we observed a sharp increase from the beginning of annealing (Fig. 5-9b). Note that the storage modulus is higher in the case of LV system. These results shows that the rheological percolation is easier to attain in the LV system.

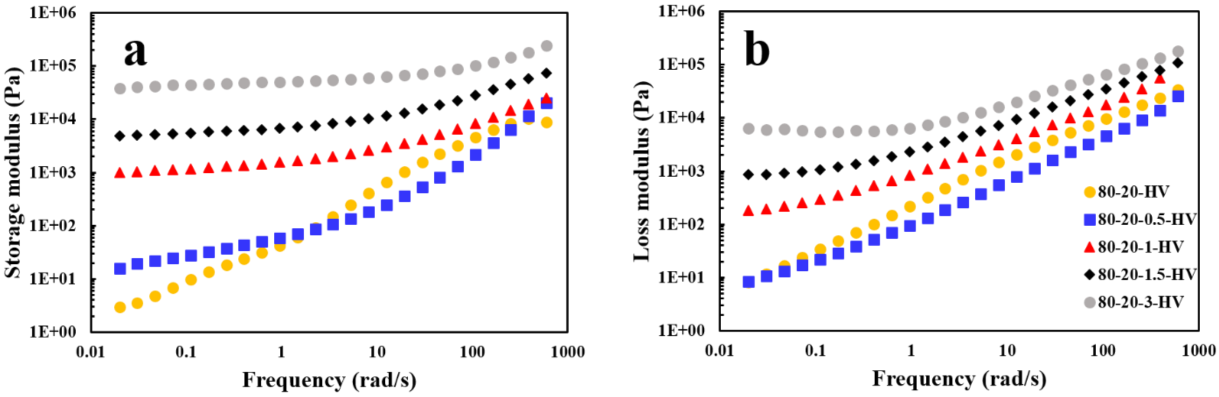

Figure 5-11. Frequency dependence of: storage modulus (a) and loss modulus (b) for different blends of HV system.

The frequency sweep response of the HV systems immediately after 2 hours of annealing under SAOS are shown in Fig. 5-10. The neat blend exhibits a predominantly viscous behavior. However, in the case of the nanocomposites, the storage modulus is independent of frequency at low frequencies indicating a solid-like behavior. We also observe (Fig. S7-17) that the viscoelastic behavior of the HV nanocomposites follows the two-phase model [109, 110] as does the LV system. This and the strong solid-like behavior indicates that the viscoelastic response of the nanocomposites is governed by the graphene structure and interfacial elasticity has negligible contribution in the viscoelastic response.

Since the 3D structure of graphene governs the viscoelastic behavior, we can use scaling theory developed by Shih et al [114] to characterize the 3D structure of graphene. This model characterize the gel structure of colloidal particles in terms of the fractal dimension of the flocs. Based on this model, the limit of viscoelastic linearity, γ_c, and the low frequency storage modulus plateau, elastic constant G'_0, scale with the filler content. Fig 5-11 shows the scaling behavior of HV system. The storage modulus at 1 rad/s, $G'(\gamma)$, is normalized by its initial value $G'(0.01)$ and the limit of linearity was evaluated based on 10% decrease in storage modulus (Fig. 5-11a). The value of storage modulus at frequency of 0.02 rad/s is chosen for the elastic constant (Fig. 5-11b). Shih et al defined two regimes: a (i) strong-link regime where the macroscopic elastic constant is governed by the intra-floc links and the limit of LVE decreases with volume fraction, and a (ii) weak-link regime where the elastic properties are dominated by the inter-floc links and the limit of LVE increases with volume fraction.

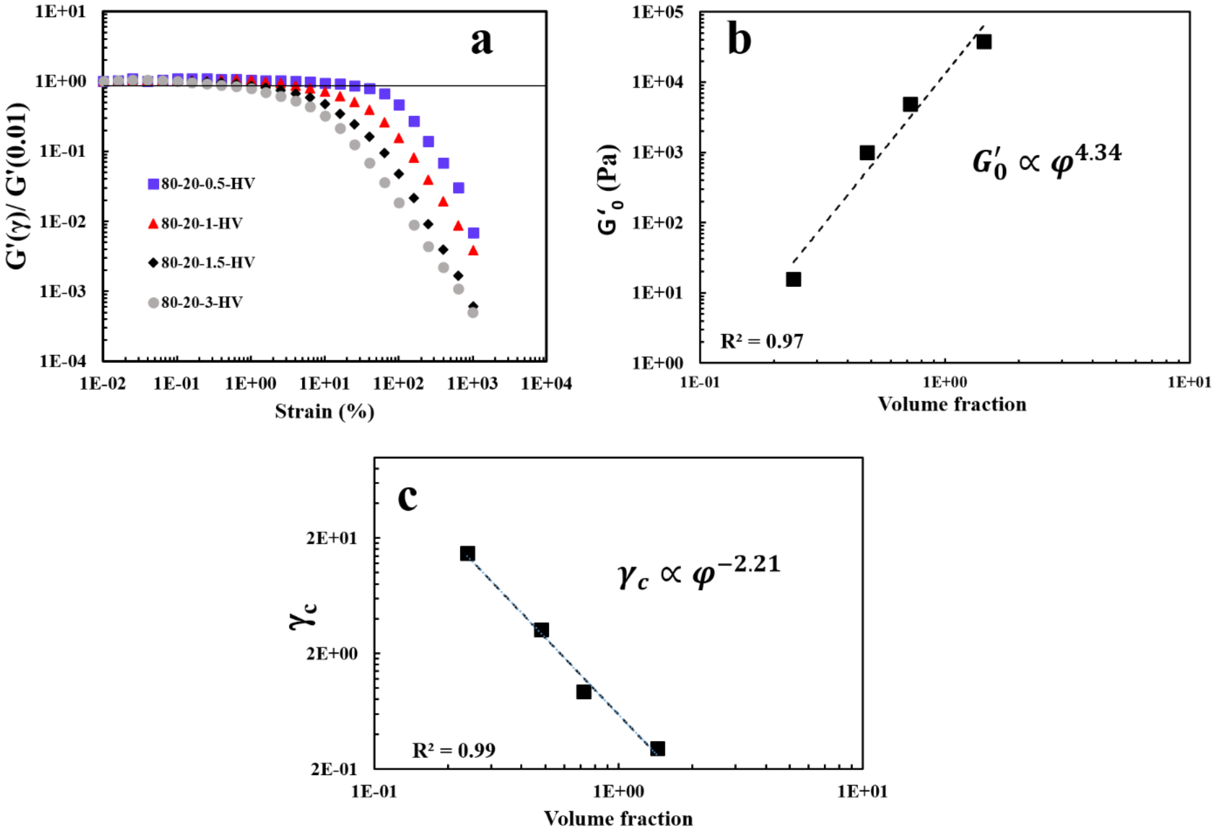

Figure 5-12. Normalized storage modulus at 1 rad/s as a function of strain for the HV system containing different graphene content (a), scaling behavior of critical strain (b) and elastic constant (c).

As shown in Fig 5-12 the LVE limit of linearity decreases with graphene content (Fig. 5-12a and c) in accordance with the strong link regime. In this regime, the fractal dimension of the flocs (d_f) and that of the effective backbone of the flocs (x) can be calculated by combining the following scaling relations[114]:

$$\gamma_c \propto \varphi^{n} \propto \varphi^{-(1+x)/(3-d_f)} \tag{5-5}$$

$$G'_0 \propto \varphi^{v} \propto \varphi^{(3+x)/(3-d_f)} \tag{5-6}$$

This analysis was previously carried out on the LV system with same thermal and mechanical history (after 2hours of annealing under SAOS within the LVE regime, and the results are summarized in Table. 5-2.

Table 5-2. Comparison between the scaling behavior of HV and LV system.

System	n (Eqn. 5-5)	v (Eqn. 5-6)	d_f	x
LV-POE	-1.56	3.03	1.64	1.12
HV-POE	-2.21	4.34	2.1	1.02

The d_f value is smaller in the case of LV system (1.64) as compared to HV system (2.1). This confirms the better dispersion of graphene platelets in the LV system resulting in a lower cluster fractal dimension. The lower fractal dimension in the case of LV system is due to the localization of graphene at the interface which hinders the formation of dense graphene cluster during mixing and annealing.

Interestingly, the fractal dimension of the effective backbone (x) in the HV system (1.02) is lower than that of the LV system (1.12). This is consistent with the more interconnected graphene 3D structure in the LV system observed in the TEM and SEM images.

As shown in TEM and SEM images, the graphene is localized at the interface and inside the POE domains. Accordingly, it can be expected that the morphology of the POE phase is influenced by the graphene 3D structure. In order to investigate this, the 2D fractal dimension of POE phase in nanocomposites containing 1.5%wt of graphene was calculated by applying the box-counting method to optical micrographs. This graphene content is chosen, because both systems have co-continuous morphology. Additionally, based on our previous study the compression force in the rheometer during sample loading has minimal impact on the phase morphology which is essentially stable during annealing under SAOS at this graphene content. Fig. 5-13 displays the distribution of the fractal dimension of individual POE domains (Fig. 5-7).

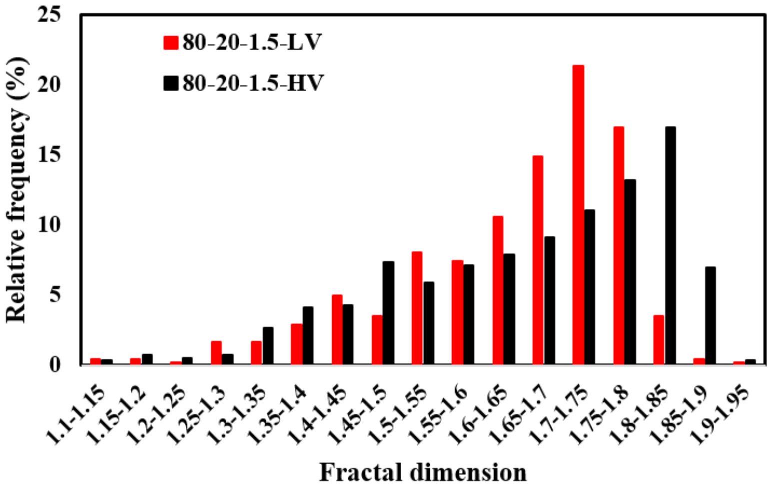

Figure 5-13. Distribution of fractal dimension of individual POE domains obtained by analyzing optical micrographs for nanocomposites containing 1.5%wt graphene.

In the case of the HV system, most POE connected domains form a compact structure with a high fractal dimension (1.7-1.9). While in the LV system, most of the domains have a fractal dimension in the range of 1.6-1.8. These results are consistent with higher 3D fractal dimension of the graphene flocs in the HV system. This shows that the structural characteristics of the nanoparticle 3D network plays an important role in the final phase morphology. Accordingly, the fractal dimension of the nanoparticle in nanocomposites obtained from rheology can give us information about the phase morphology of the host phase provided that the nanoparticles are selectively located inside one component or at the interface.

5.5. Conclusion

The impact of POE rheological properties and the incorporation of compatibilizer were investigated on the phase morphology and properties of PA6/POE nanocomposites containing graphene. It was revealed that the graphene is better dispersed in the low viscosity system. This means that in the low viscosity system, more of the interface is covered with graphene resulting in stable, elongated POE domains. Consequently, in the case of HV system, the elongated domains form at higher graphene content as compared to LV system.

Interestingly, graphene induces a co-continuous morphology in both systems. However, in the case of the LV system, we observe an open POE structure with a high degree of interconnectivity, while in the HV system a compact fractal-like POE structure was observed. The formation of a co-continuous morphology occurs at a lower graphene content in the LV system. These differences indicate a higher coalescence rate in the LV system. Similar to the formation of a co-continuous morphology, electrical percolation occurs at a lower graphene content in the LV system.

We found that the rheological response of both the LV and HV systems are governed by the graphene 3D structure which allows us to characterize the graphene 3D structure with the fractal scaling theory. The fractal scaling parameters determined from the rheological response were consistent with the better dispersion of graphene (lower fractal dimension of graphene floc) and higher degree of connectivity (higher fractal dimension of graphene effective backbone) in the LV system observed via TEM. Comparing the distribution of the 2D fractal dimension of POE domains (optical microscopy) with the 3D fractal dimension of the graphene flocs (rheological response) revealed that the structure of the POE domains are influenced by the structural features of the graphene 3D network.

In the case of the compatibilized system, our morphological analysis shows that while the addition of compatibilizer in HV system results in the formation of elongated domains, it hinders the coalescence between the POE domains increasing the number of individual domains in the system. The compatibilizer also reduces the graphene coverage at the interface. These structural changes lead to a decrease in electrical conductivity with increasing compatibilizer content.

6. CONCLUSION AND FUTURE WORK

The impact of graphene on the phase morphology, mechanical and electrical properties of PA6/POE blends were investigated. The impact of graphene localization was studied at two blend compositions (i) 60/40 (PA6/POE) which is close to the phase inversion point, and (ii) 80/20 with asymmetric composition. The final phase morphology was influenced by the impact of graphene on the elasticity of the host phase. The presence of graphene inside one phase increases the elasticity of that phase, enhancing the stability of elongated domains. In the 60/40 system, this leads to a stable co-continuous morphology independent of graphene localization. In the case of the 80/20 system prepared by the POE master batch, the presence of graphene inside the POE minor phase led to a co-continuous morphology with good mechanical properties and an ultra-low electrical percolation threshold. Accordingly, this composition and mixing order was chosen for further investigation. The evolution of phase morphology for this system was investigated during two annealing conditions (i) quiescent condition, and (ii) after compression and applying SAOS. As expected, the presence of graphene inside the POE stabilized the phase morphology during quiescent annealing. However, in the case of annealing under SAOS conditions, the morphological evolution is significantly modified by the compression force during sample loading. Our studies revealed that while the presence of graphene slows down the shape relaxation, it increases the coalescence rate at the early stage of annealing. This enhanced coalescence rate is a result of the normal force applied during sample loading along with a retarded shape relaxation and graphene bridging between neighboring domains. This eventually leads to the formation of a fractal-like structure of POE phase which is attributed to the self-assembly of graphene particles. The evolution of the graphene 3D network during annealing significantly increased the electrical properties reducing the percolation threshold. By comparing the phase morphology of two systems containing either high or low viscosity POE with different graphene dispersion and localization, it has been shown that the self-assembly of nanoparticles has a direct impact on the morphology of host phase. Accordingly, by characterizing the nanoparticle 3D structure it is possible to obtain information about the phase morphology.

The contributions of this study can be summarized as follows:

1- <u>Proposing a new strategy for achieving an ultra-low electrical percolation threshold for graphene-based nanocomposites by inducing a co-continuous morphology at low</u>

content of nanoparticle host phase: This is important when a high host phase content has detrimental impacts on the mechanical properties.

2- Providing new insight regarding the migration of platelet-like graphene nanoparticles: It has been shown that the graphene particles with better dispersion can successfully migrate to the interface which is the thermodynamically preferred location. Due to their high aspect ratio, graphene particles can penetrate to the interface and bridge neighboring domains preserving the continuity of graphene 3D structure. The migration to the interface is prevented in the case of compatibilized systems where the presence of compatibilizer at the interface reduces the thermodynamic driving force for graphene localization at the interface.

3- Providing new insights regarding the mechanism of nanoparticle-induced co-continuity: we have shown that besides the impact of nanoparticles on the stability of elongated domains, their self-assembly plays a significant role on the phase morphology. The phase morphology formed during mixing changes considerably after compression facilitating the rearrangement of the graphene particles. This subsequently leads to the formation of a percolated fractal-like structure of the nanoparticle host phase.

4- Clarifying the impact of nanoparticle 3D structure on the rheological response both at equilibrium conditions and during microstructure evolution: It has been shown that at sufficiently high nanoparticle content, the rheological response of the nanocomposites is primarily governed by the percolated structure of nanoparticles and interface elasticity has a negligible effect. Additionally, we have revealed that the annealing time has the same influence on the rheological properties as nanoparticle content.

5- Proposing a rheological method for characterizing the phase morphology where the nanoparticles are located inside one component or at the interface: It has been shown that the structure of the host phase for graphene is influenced by the structural feature of graphene 3D network. This allows us to obtain information about the phase morphology by characterizing the nanoparticle 3D network using rheological methods.

6.1. Future work

1- Morphological characterization during mixing. There is considerably less information about the impact of nanoparticle on the evolution of phase morphology during the mixing step. By tracking the morphological evolution, especially at early stages of mixing or in simpler flows, we can have valuable information on how nanoparticles affect the breakup and coalescence behavior of the domains.

2- It is also interesting to look at the impact of shear force during mixing, both on the final morphology and its evolution during mixing.

3- Further investigation on the impact of dispersion of graphene on the phase morphology. It is possible to employ different methods for preparing the master batch such as solvent mixing. Comparing the structural features of the master batch and that of the blend nanocomposite could also provide valuable information regarding the impact of self-assembly of nanoparticle on the phase morphology and vice versa.

4- Investigating the impact of functionalized graphene on rheological behavior and phase morphology. We have shown that the mechanism by which graphene slows down the dynamics is independent of graphene content and phase morphology. However, in our case graphene does not have strong interaction with either of the components. Comparing our results with systems that do have a strong interaction can provide new insight regarding the impact of nanoparticle on the rheological response of complex systems such as polymer blends.

5- Investigating the non-linear rheological response. This gives us information about rheological behavior in real processing conditions which is substantially less explored.

7. APPENDICES

7.1. Appendix 1. Supporting Information for chapter 3

7.1.1. Surface energy, interfacial tension and wetting coefficient

Here we use thermodynamic analysis to predict the expected location of graphene in our system. At the equilibrium state, the localization of particles in immiscible blends is predicted by the wetting parameter, ω, proposed by Sumita et al[57]

$$\omega = \frac{\gamma_{P/PA} - \gamma_{P/POE}}{\gamma_{PA/POE}} \qquad \text{(S7-1)}$$

Here, $\gamma_{P/PA}$ is interfacial tension between the graphene particle and PA phase, $\gamma_{P/POE}$ is interfacial tension between the particle and POE and $\gamma_{PA/POE}$ is the interfacial tension between the polymer phases. If $\omega > 1$, the particles are expected to be dispersed in POE. If $\omega < -1$, the particles are expected to be dispersed in PA and if $-1 < \omega < 1$ the particle is expected to be localized at the interface. The interfacial tension between the various components can be calculated by the geometric mean and harmonic mean equations[58, 59].

$$\gamma_{1/2} = \gamma_1 + \gamma_2 - 2(\sqrt{\gamma_1^d \gamma_2^d} + \sqrt{\gamma_1^p \gamma_2^p}) \qquad \text{(S7-2)}$$

$$\gamma_{1/2} = \gamma_1 + \gamma_2 - 4\,(\frac{\gamma_1^d \gamma_2^d}{\gamma_1^d + \gamma_2^d} + \frac{\gamma_1^p \gamma_2^p}{\gamma_1^p + \gamma_2^p}) \qquad \text{(S7-3)}$$

Here γ_i is the surface energy of component i and γ_i^d and γ_i^p are the dispersive and polar contributions to the surface energy, respectively.

The interfacial energy of blend components are determined as explained in Section 2.3.1. using contact angles of water and diiodomethane with each constituent (Table S7-1).

Table S7-1. Contact angles and surface energy of components at room temperature

Component	Contact angle (º)		Surface tension at 25 °C (mN/m)		
	diiodomethane	Water	Total	Polar	Disperse part
PA	57.1	76.8	37.34	7.11	30.23
POE	67.4	98.6	25.58	1.12	24.35
Graphene	0	117	54.32	3.52	50.8

Since the mixing process is performed at 240°C, we use literature values of the temperature coefficients to extrapolate the surface energies to that temperature (Table S7-2).

Table S7-2. Surface energies of components at compounding temperature

material	Temperature coefficient $d\gamma/dT$ (mN/m^2 °C)	Total surface energy at 240°C ($mN\ m^{-1}$)	Dispersive surface energy at 240°C ($mN\ m^{-1}$)	Polar surface energy at 240°C ($mN\ m^{-1}$)
PA	-0.065 [129]	22.94	18.57	4.37
POE	-0.052 [130]	14.4	13.77	0.63
Graphene	-0.1[74]	32.82	30.7	2.12

The calculated interfacial tension between the various component pairs and the wetting coefficient are summarized in Table S7-3.

Table S7-3. Calculated interfacial tension between components and wetting parameters

Method	$\gamma_{PA6/Graphene}$	$\gamma_{POE/Graphene}$	$\gamma_{PA6/POE}$	ω	Predicted location
Mean harmonic equation	3.75	7.25	3.5	-0.99	Interface
Mean geometric equation	1.91	3.78	2.03	-0.92	Interface

As we can see, this analysis predicts that at thermodynamic equilibrium, graphene is located at the interface of the two polymers. Note that graphene has more affinity toward the PA phase.

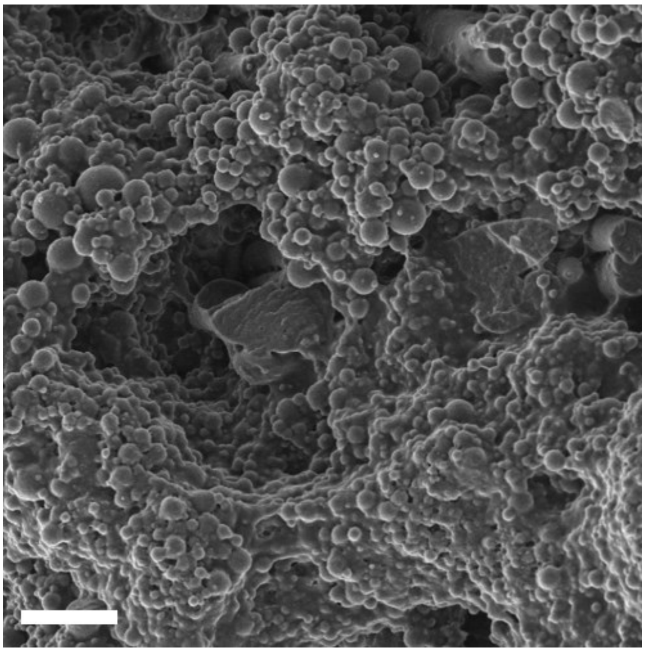

Figure S7-1. FESEM micrograph of PA6/POE blend (60/40) after 15 minutes compression molding. (Scale bar corresponds to 10μm.)

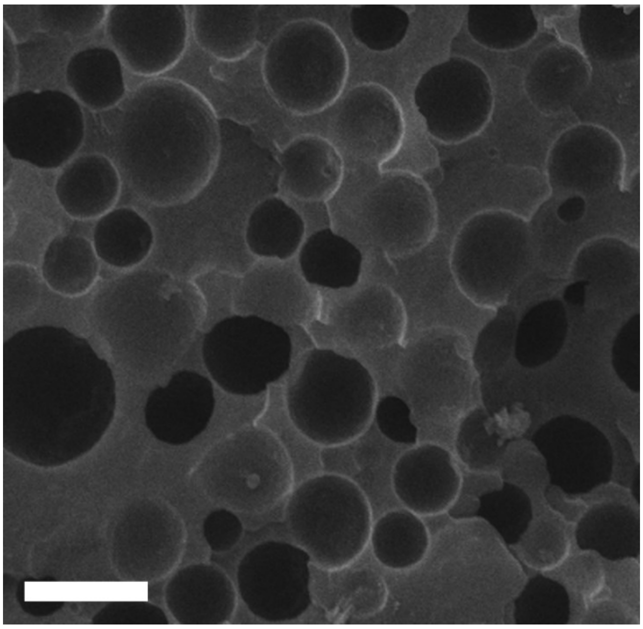

Figure S7-2. SEM micrograph of PA6/POE blend (70/30). (Scale bar corresponds to 5μm.)

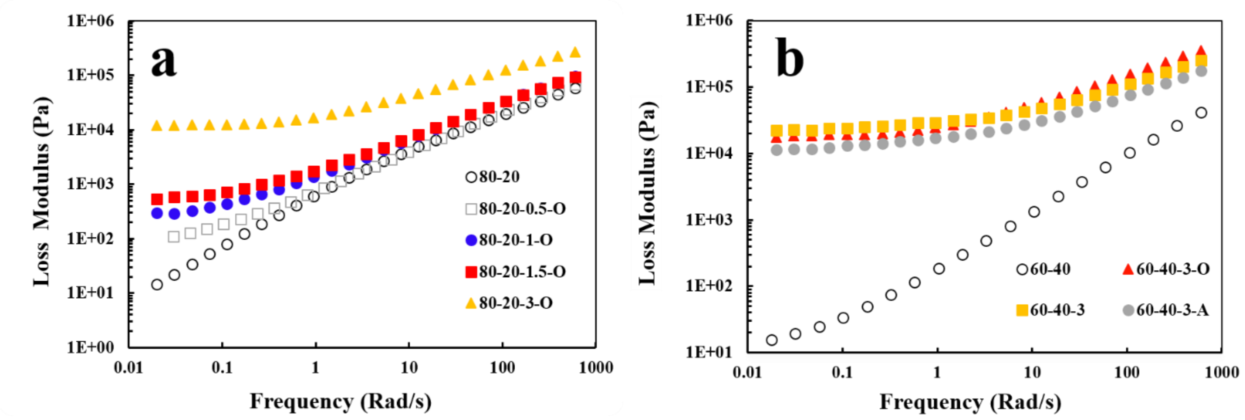

Figure S7-3. Melt state loss modulus of a) 80/20 (PA6/POE) blends prepared by POE master batch, b) 60/40 blend prepared by different mixing order.

Table S7-4. Crystallization temperature (Tc), crystallization enthalpy (ΔHc), melting temperature(Tm), melting enthalpy (ΔH$_m$), for different blends.

Sample	T_m (°C)	T_{c1} (°C)	T_{c2} (°C)	T_{c3} (°C)	ΔH_{m1} (J. g $^{-1}$)	$\Delta H_{m2,3}$ (J. g $^{-1}$)	ΔH_{c1} (J. g $^{-1}$)	$\Delta H_{c2,3}$ (J. g $^{-1}$)
PA	218.8	---	195.19	---	---	89.3	---	87.7
60-40	220	112.82	195.5	---	1.36	48.9	0.7898	48.1
60-40-3-O	221.4	---	196.2	---	---	44.9	---	42.2
60-40-3	221.3	---	196.9	206.9	---	57.5	---	49.9
60-40-3-A	220.0	---	197	206.9	---	53.4	---	49.3
80-20	217.9	---	194	---	---	64.8	---	63.2
80-20-0.5-O	219.8	---	195.8	---	---	64.1	---	61.1
80-20-1-O	220.9	---	195.6	---	---	63.4	---	61.4
80-20-1.5-O	220.4	---	195	---	---	62.4	---	60
80-20-3-O	221.4	---	196	---	---	56.1	---	56.3

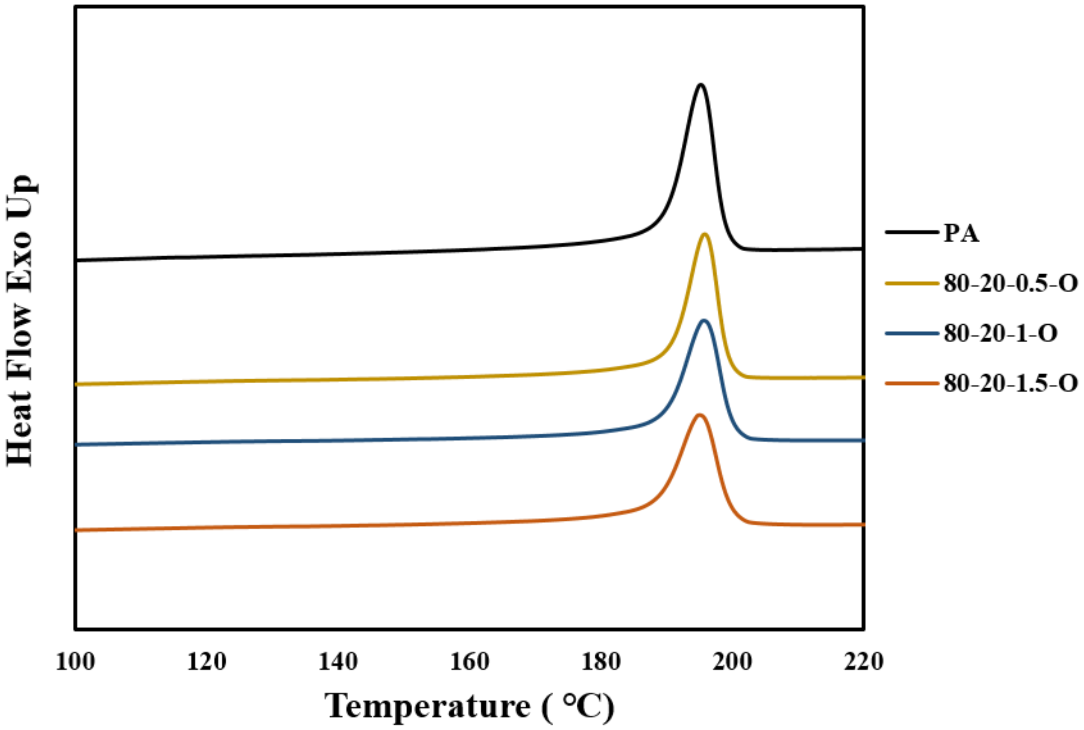

Figure S7-4. DSC cooling curves.

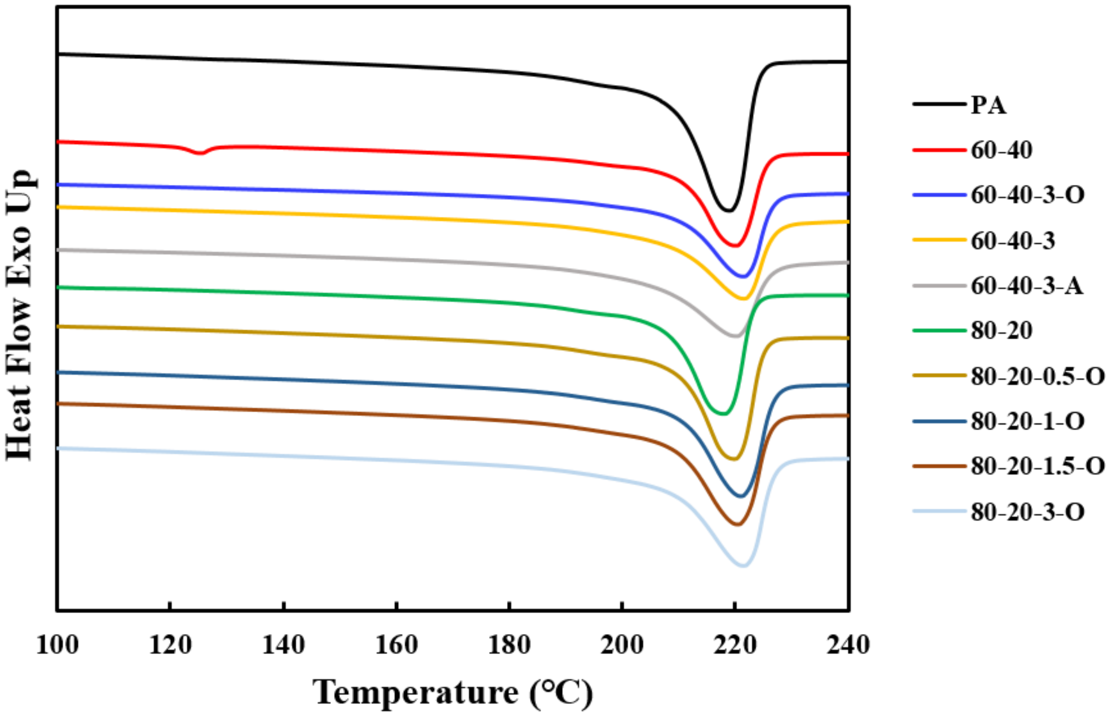

Figure S7-5. DSC heating curves.

7.2. Appendix 2. Supporting Information for chapter 4

Figure S7-6 shows that while degradation occurs during processing, the storage modulus reaches a constant value within a few minutes during annealing.

SEM images of the blend and nanocomposites annealed under SAOS conditions, at time=0 and time=34 minutes are shown in Figure S7-7.

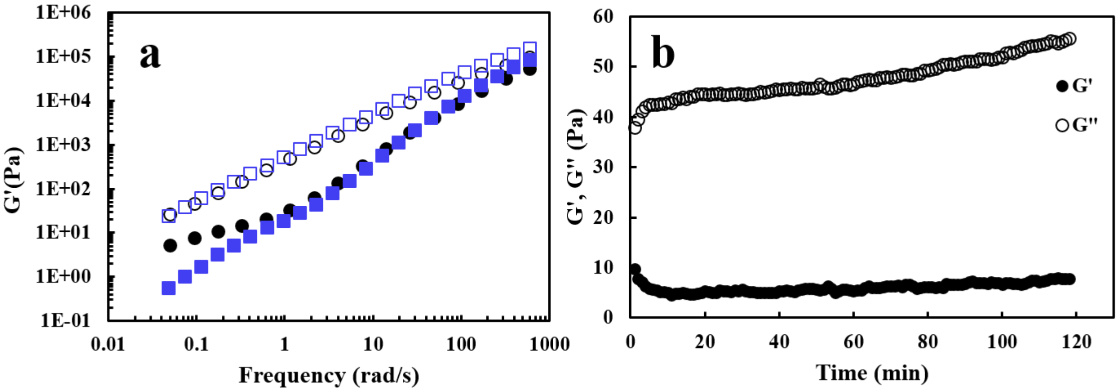

Figure S7-6. a) Frequency dependence of storage (solid symbols) and loss modulus (open symbols) for un-processed (blue squares) and processed (black circles) PA6. b) Evolution of viscoelastic response of processed PA6 during annealing at 0.1 rad/s.

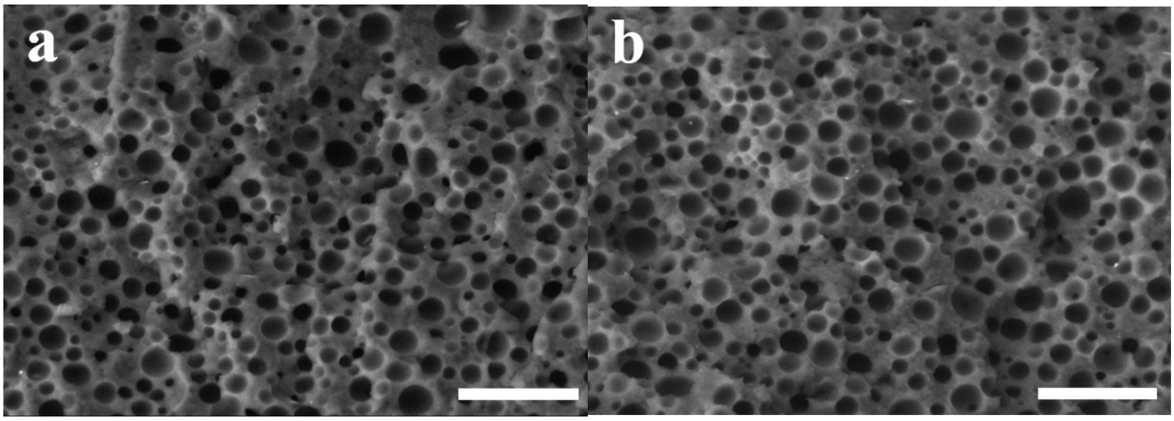

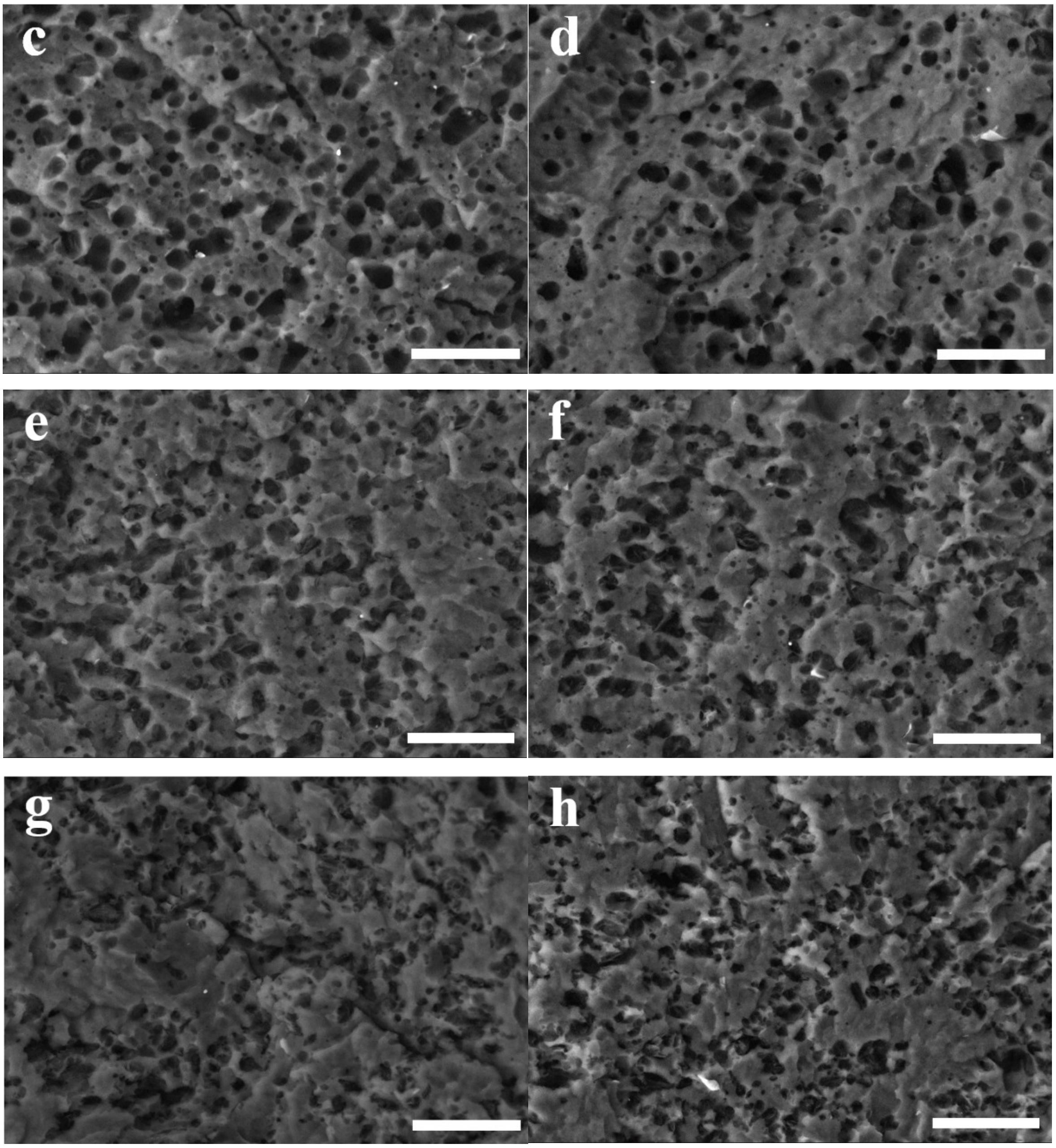

Figure S7-7. Phase morphology while annealing under SAOS conditions at 0.1 rad/s: 80-20 at time=0 (a), 80-20 after 30 minutes of SAOS (b), 80-20-0.5 at time=0 (c), 80-20-0.5 after 30 minutes of SAOS (d), 80-20-1 after time=0 (e), 80-20-1 after 30 minutes of SAOS (f), 80-20-1.5 at time=0 (g), 80-20-1.5 after 30 minutes of SAOS (h). The POE phase is extracted and scale bars correspond to 25µm.

SEM images of the blend and nanocomposites annealed under quiescent conditions, at time=0 and time=34 minutes are shown in Figure S7-8.

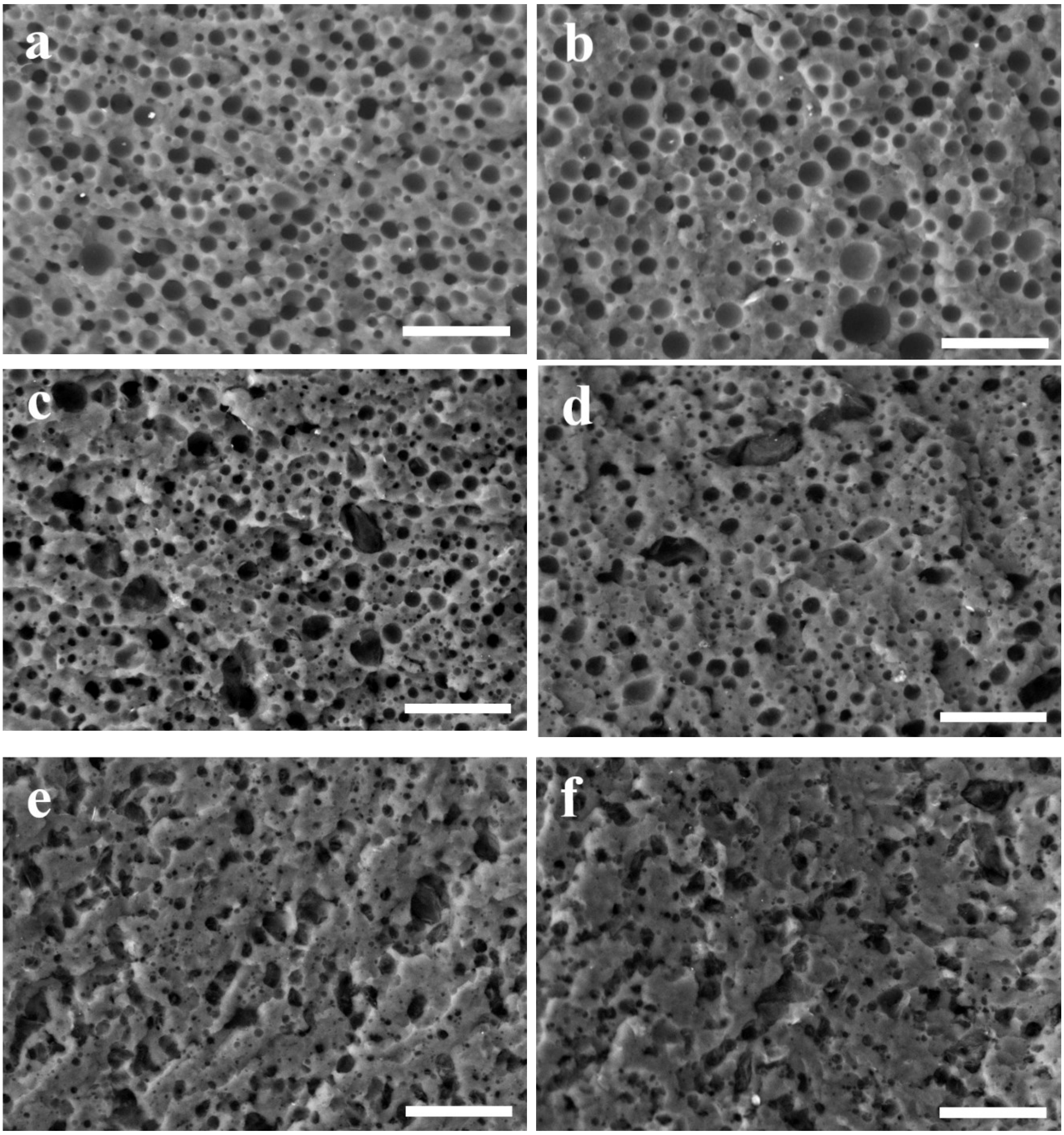

Figure S7-8. Phase morphology while annealing under quiescent conditions for: 80-20 at time=0 (a), 80-20 after 34 minutes (b), 80-20-0.5 at time=0 (c), 80-20-0.5 after 34 minutes (d), 80-20-1 at time=0 (e), 80-20-1 after 34 minutes (f). The POE phase is extracted and scale bars correspond to 25µm.

The circularity distribution and average circularity of neat blend and nanocomposites are compared at time=0 and after 34 minutes of annealing under the quiescent conditions (without applying a normal force) and SAOS conditions (after squeezing the sample).

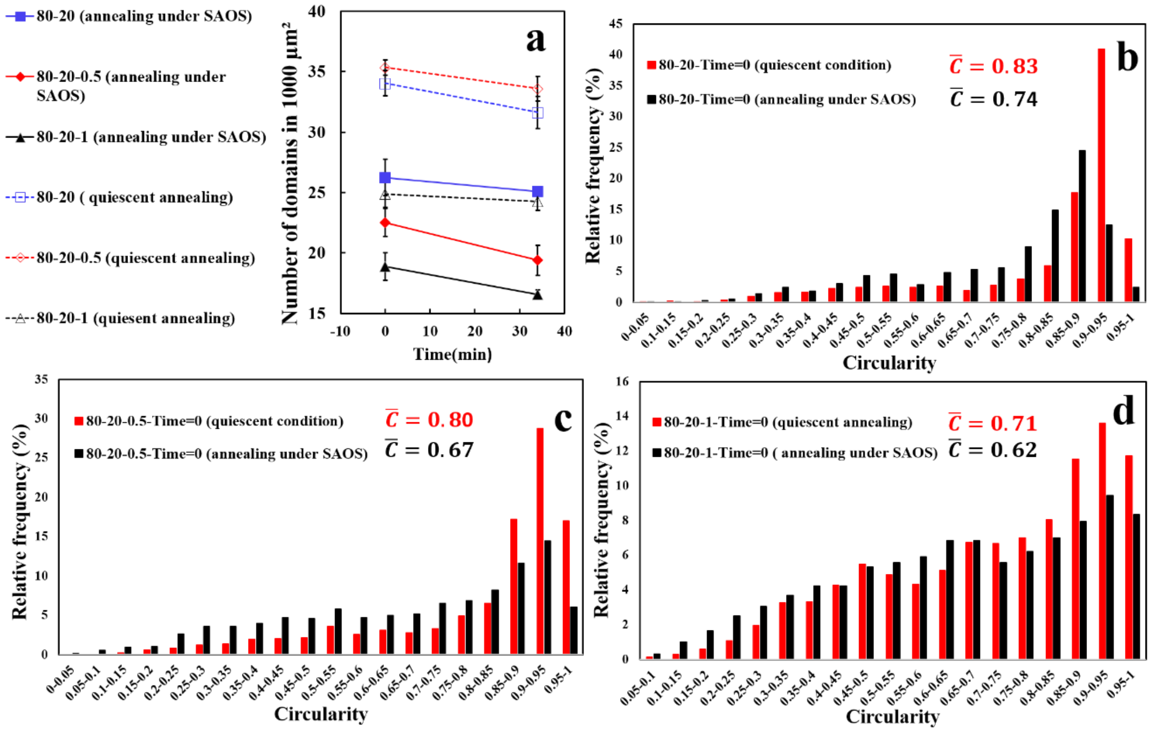

Figure S7-9. a) Change in N for the samples annealed under SAOS and quiescent conditions during first 30 minutes. b,c and d) Domain circularity distribution and average circularity for nanocomposites at time=0, without applying compression force (quiescent annealing) and with applying the compression force (annealing under SAOS) with the same thermal history.

These results show that the number of discrete domains decreases significantly after compression in the rheometer.

During annealing, the coalescence rate, shown by the slope of "N" versus time, is lower under quiescent conditions as compared to the SAOS condition for the nanocomposites. Since the normal force decreases the number of domains at time=0, we believe that the increased coalescence rate is primarily due to the normal force (squeezing force) applied before starting the SAOS that takes time to relax.

7.2.1. Estimation of Hamaker constant

The Hamaker constant for two objects of the same material separated in a vacuum (A_{11}) can be estimated by eqn. S7-4[131]:

$$A_{11} = 24\,\pi {D_0}^2 \gamma_1 \quad \text{(S7-4)}$$

Where the D_0= 1.65 10^{-10} m and γ_1 is the surface tension of the object.

The Hamaker constant between the two bodies interacting in a medium 2 can be estimated using eqn. S7-5[131].

$$A_{121} = (\sqrt{A_{11}} - \sqrt{A_{22}})^2 \tag{S7-5}$$

The surface tension of our components at room temperature have been measured in our previous work and extrapolated to the annealing temperature (T= 240°C) which are summarized in Table S7-5[99].

Table 7-5. Surface tension of components at annealing temperature.

material	**Total surface energy at 240℃ (mN m^{-1})**
PA	22.94
POE	14.4
Graphene	32.82

Using the surface tension of components, it is possible to estimate the Hameker constant A_{11} for the components using eqn. S7-4 (Table S7-6).

Table S7-6. Hamaker constant at 240°C for the components interacting under vacuum.

Component	**A_{11} *10^{20} (J)**
PA6	4.7
POE	2.9
Graphene	6.7

From these values, we can estimate the Hameker constant between the POE domains and graphene particles interacting in a PA6 matrix. The Hameker constant between the graphene particles gives us an estimate of the Hameker constant between the graphene coated POE domains (Table S7-7).

Table S7-7. Hamaker constant for the POE and graphene interacting in PA matrix at 240°C.

Media (1-2-1)	**$A_{121}*10^{21}$ (J)**
POE-PA6-POE	2
Graphene-PA6-Graphene	1.8

This analysis shows that the Hamekar constants for the bare POE domains and graphene-coated domains are essentially the same. Accordingly, the decreased coalescence rate in the nanocomposites is most probably due to the increase in the viscosity of POE phase when it contains graphene.

Samples exposed to solvent extraction are shown in Figure S7-10.

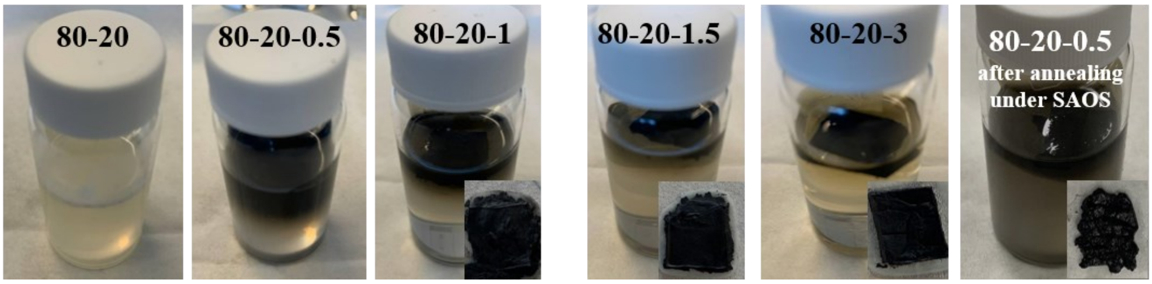

Figure S7-10. The samples after solvent extraction of PA6 major phase for different content of graphene.

7.2.2. Comparison between the thermal energy and energy required for removing one graphene sheet from the interface

The energy required for removing one graphene sheet from the interface to component A can be estimated by Eqn. S7-6. Here the energy is normalized by the thermal energy at annealing temperature.

$$\frac{\Delta E_{interface/A}}{k_b T} = \frac{A_G(\gamma_{G/A}-\gamma_{G/B}+\gamma_{A/B})}{k_b T} \qquad \text{(S7-6)}$$

Here γ_{ij} is the interfacial tension between the component i and j at 240°C (these values have been measured at room temperature and estimated at 240°C in our previous paper [99]), and A_G is the surface area of graphene and k_B, and T are Boltzmann constant and temperature (513 K), respectively. The graphene used in this study has a broad size distribution (from 200 nm to 4000 nm) with an average area of ~ 1.25μm^2 and average diameter of ~1.26μm [64]. Fig. S7-11 shows the $\frac{\Delta E_{interface/A}}{k_b T}$ as a function of platelet diameter (d).

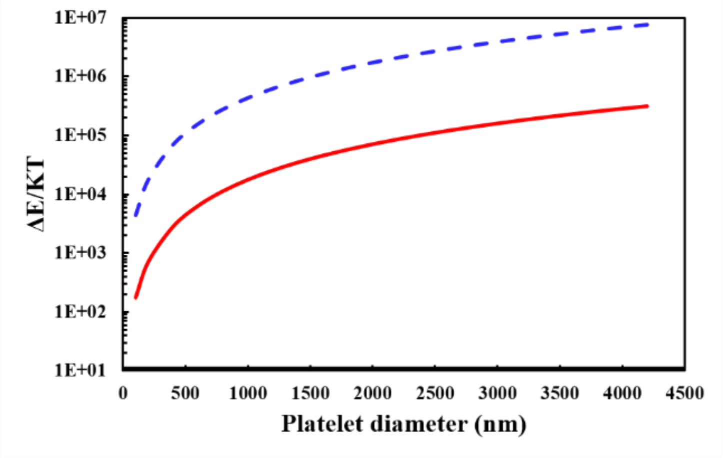

Figure S7-11. Estimated energy required for detachment of one graphene sheet from interface normalized by the thermal energy as a function of platelet diameter. The dotted blue line and the red line show the detachment energy for graphene toward POE and PA phase, respectively.

From this figure, we see that the detachment energy toward PA is less than that of POE; however, both are far higher than the thermal energy especially for larger platelets. Note that it is not clear whether the interparticle interactions or the compression force can overcome this energy barrier during annealing when two domains are sufficiently close to each other.

7.2.3. Estimation of two-phase model shift factors for master curves

In order to estimate the horizontal, a_φ, and vertical, b_φ, shift factors we followed the procedure proposed by Fillippone et al[110]:

To consider the impact of hydrodynamic effect arising from the presence of graphene particles, the loss modulus (G″(ω)) of the neat blend (PA6/POE) with same thermal history was amplified by $B(\varphi) = \frac{G^*{}_{PA6/POE/graphene}}{G^*{}_{PA6/POE}}$ where the G* are those associated with the highest frequency (600 rad/s).

The a_φ and b_φ are then calculated as the coordinate of the point at which G′(ω→0)= b_φ (elasticity of the nanocomposite at the lowest frequency) equals to the amplified G″ of the neat blend. This procedure is shown for the 80-20-0.5 and 80-20-1 nanocomposites in Fig. S7-12.

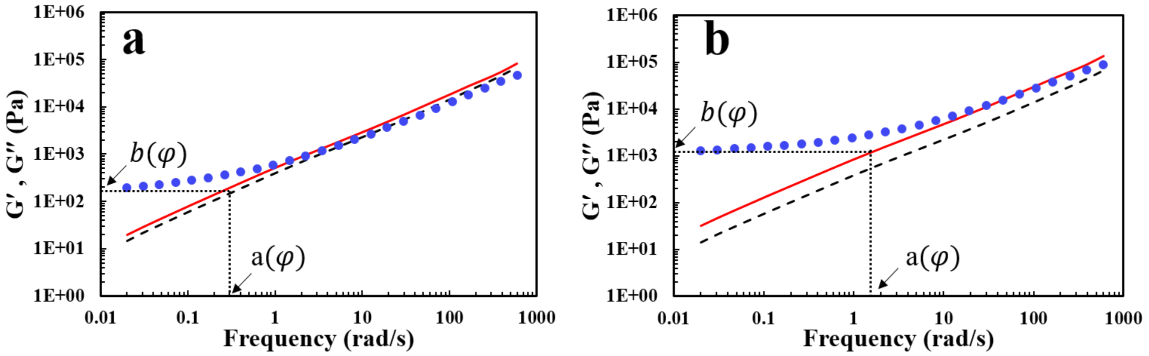

Figure S7-12. Estimation of horizontal and vertical shift factors for a) 80-20-0.5 and b) 80-20-1 nanocomposites. The blue data points show the storage modulus of the nanocomposite. The dashed line is the loss modulus of neat blend (PA6/POE: 80/20) at the same thermal history as nanocomposites. The red line is the amplified loss modulus of neat blend ($\boldsymbol{B(\varphi) \times G''(\omega)}$).

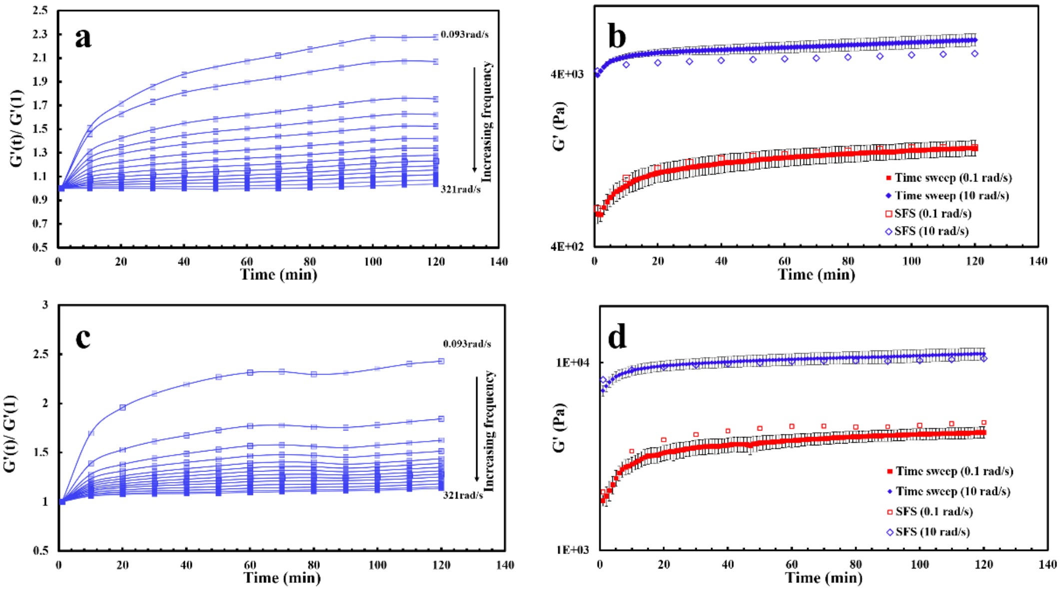

Figure S7-13. The evolution of normalized storage modulus over time at different frequencies calculated by interpolation of SFS results for 80-20-1(a) and 80-20-1.5(c). Comparison between the evolution of storage modulus during time sweep at constant frequency and SFS at 0.1 and 10 rad/s, for 80-20-1(b) and 80-20-1.5 (d) nanocomposite.

7.3. Appendix 4. Supporting Information for chapter 5

Figure S7-14 show that while degradation occurs during processing the storage modulus reaches a constant value within a few minutes during annealing.

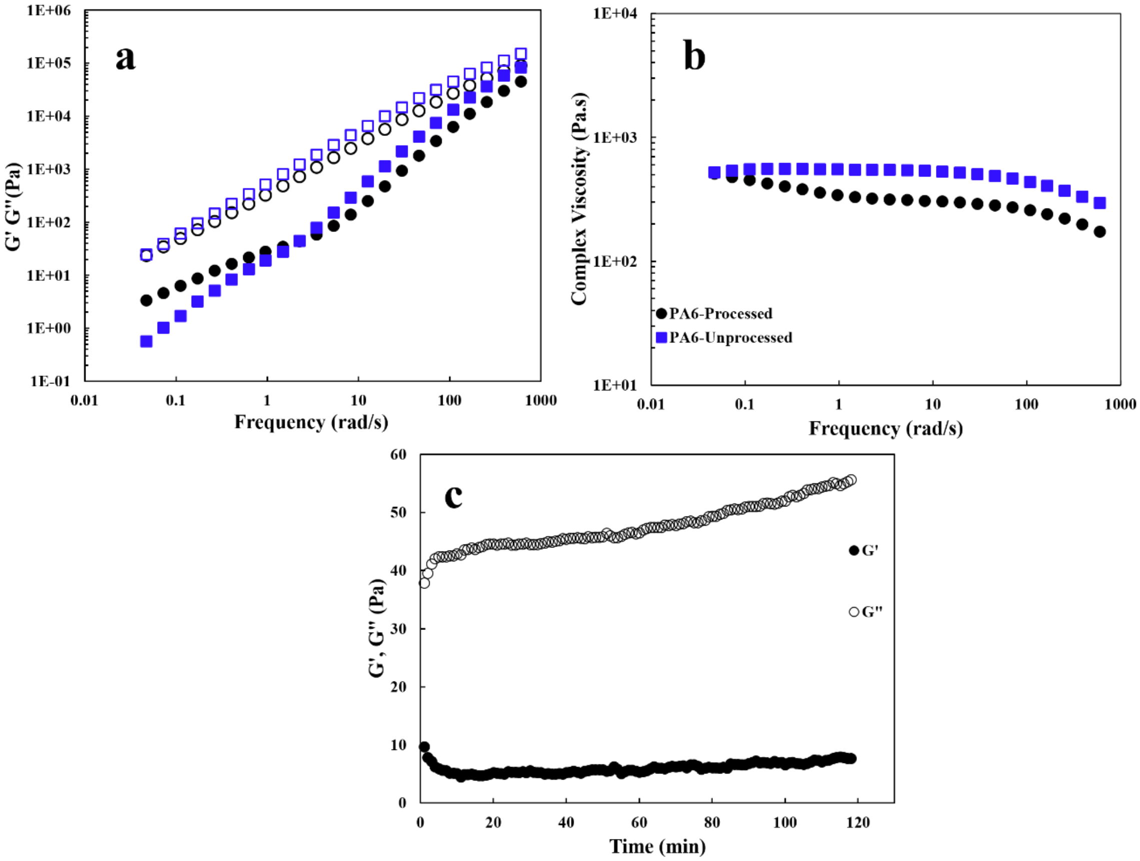

Figure S7-14. Frequency dependence of a) storage (solid symbols) and loss modulus (open symbols) b) complex viscosity, for un-processed (blue squares) and processed (black circles) PA6. c) Evolution of viscoelastic response of processed PA6 during annealing at 0.1 rad/s.

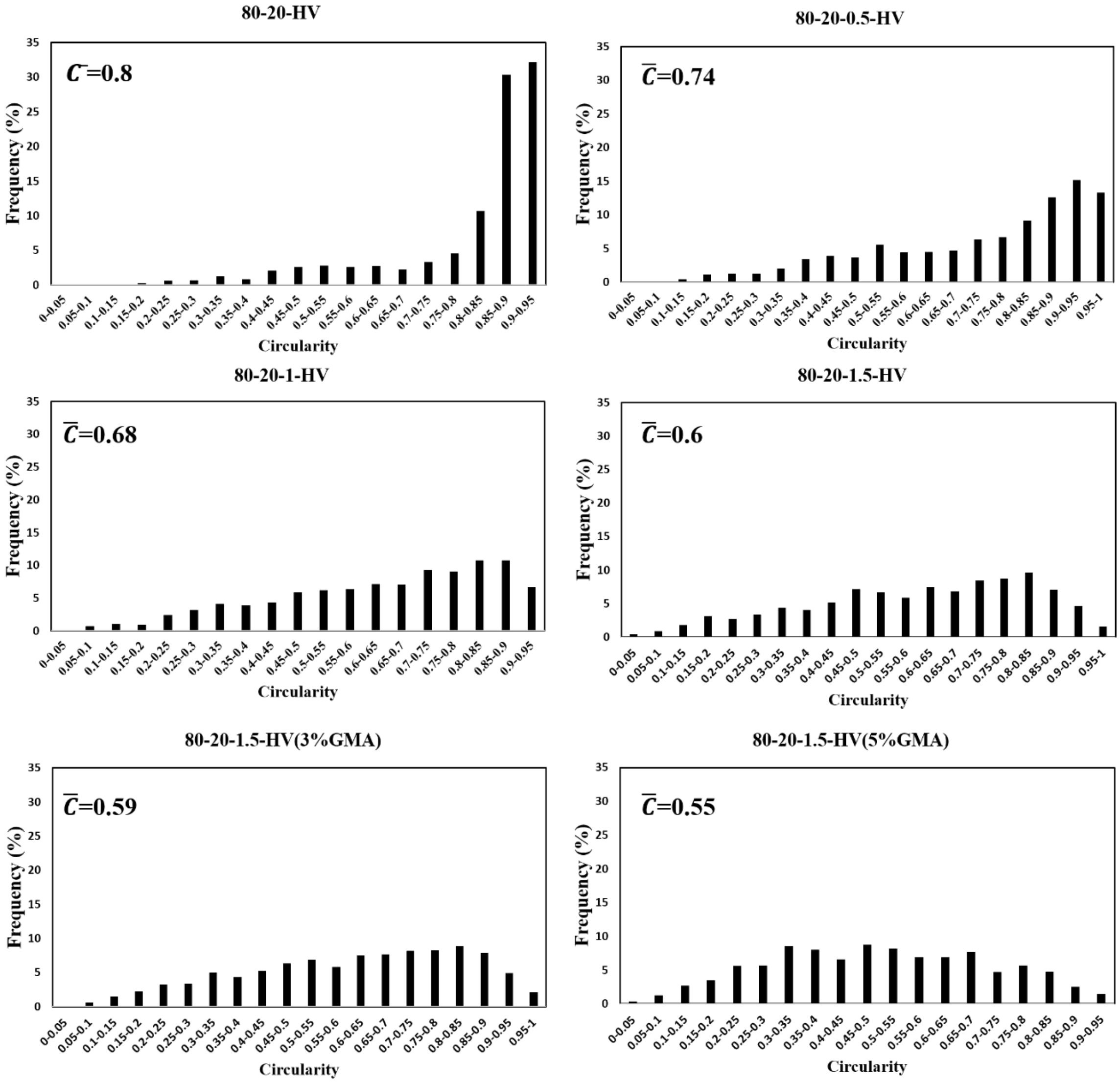

Figure S7-15. Distribution of domain circularity and its average value for uncompatiblized and compatibilized HV system.

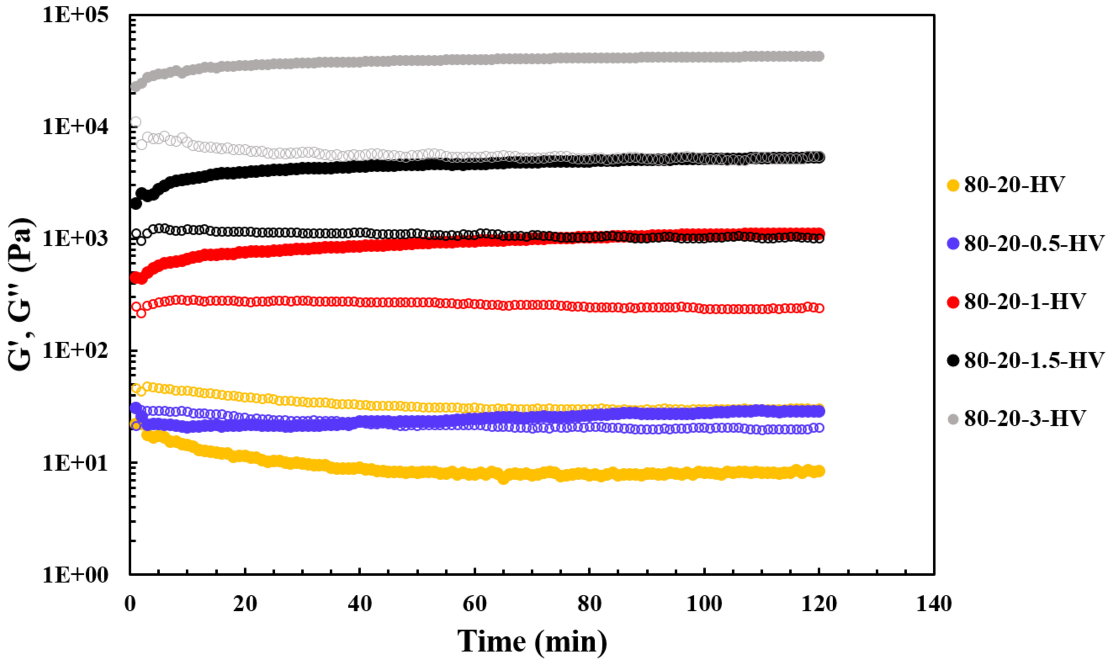

Figure S7-16. Evolution of viscoelastic response of different samples in HV system.

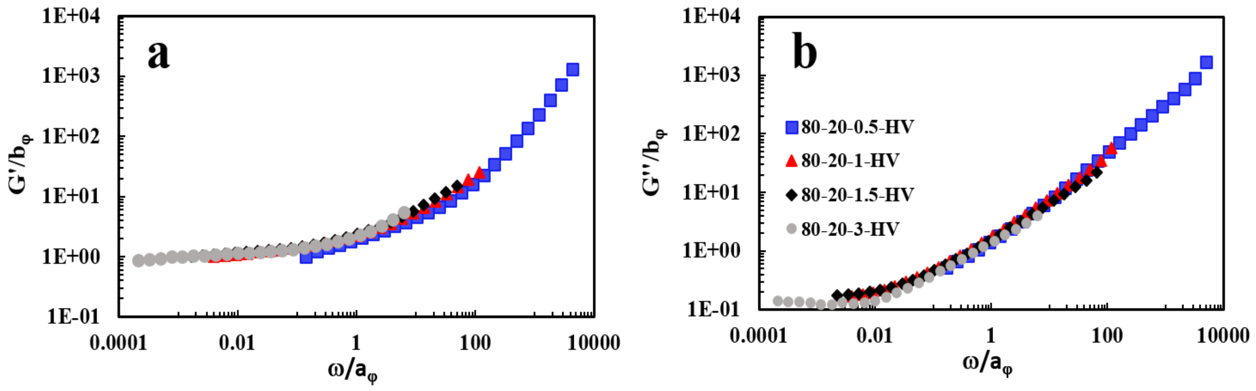

Figure S7-17. Master curve of a) G’ and b) G” produced with two shift factors for HV system.

8. REFERENCES

1. Afshari, M., et al., *Effect of blend ratio on bulk properties and matrix–fibril morphology of polypropylene/nylon 6 polyblend fibers*, in *Polymer*. 2002. p. 1331-1341.
2. Filippone, G., et al., *The role of organoclay in promoting co-continuous morphology in high-density poly (ethylene)/poly (amide) 6 blends.* Polymer, 2008. **49**(5): p. 1312-1322.
3. Bai, L., et al., *Localizing graphene at the interface of cocontinuous polymer blends: Morphology, rheology, and conductivity of cocontinuous conductive polymer composites.* Journal of Rheology, 2017. **61**(4): p. 575-587.
4. Wilson, J., et al., *Synthesis and magnetic properties of polymer nanocomposites with embedded iron nanoparticles.* Journal of Applied Physics, 2004. **95**(3): p. 1439-1443.
5. Guo, L., et al., *Highly monodisperse polymer-capped ZnO nanoparticles: preparation and optical properties.* Applied Physics Letters, 2000. **76**(20): p. 2901-2903.
6. Kim, H., A.A. Abdala, and C.W. Macosko, *Graphene/polymer nanocomposites.* Macromolecules, 2010. **43**(16): p. 6515-6530.
7. Xie, S., Y. Liu, and J. Li, *Comparison of the effective conductivity between composites reinforced by graphene nanosheets and carbon nanotubes.* Applied Physics Letters, 2008. **92**(24): p. 243121.
8. Kim, H., et al., *Graphene/polyethylene nanocomposites: Effect of polyethylene functionalization and blending methods.* Polymer, 2011. **52**(8): p. 1837-1846.
9. Brigandi, P.J., J.M. Cogen, and R.A. Pearson, *Electrically conductive multiphase polymer blend carbon-based composites.* Polymer Engineering & Science, 2014. **54**(1): p. 1-16.
10. Mayoral, B., et al., *Melt processing and characterisation of polyamide 6/graphene nanoplatelet composites.* Rsc Advances, 2015. **5**(65): p. 52395-52409.
11. Papadopoulou, E.L., et al., *Nylon 6, 6/graphene nanoplatelet composite films obtained from a new solvent.* RSC advances, 2016. **6**(8): p. 6823-6831.
12. Zheng, D., et al., *In situ thermal reduction of graphene oxide for high electrical conductivity and low percolation threshold in polyamide 6 nanocomposites.* Composites Science and Technology, 2012. **72**(2): p. 284-289.

13. Gubbels, F., et al., *Selective localization of carbon black in immiscible polymer blends: a useful tool to design electrical conductive composites.* Macromolecules, 1994. **27**(7): p. 1972-1974.
14. Gubbels, F., et al., *Design of electrical composites: determining the role of the morphology on the electrical properties of carbon black filled polymer blends.* Macromolecules, 1995. **28**(5): p. 1559-1566.
15. Faridirad, F., S. Ahmadi, and M. Barmar, *Polyamide/carbon nanoparticles nanocomposites: A review.* Polymer Engineering & Science, 2017. **57**(5): p. 475-494.
16. Lee, J.K. and C.D. Han, *Evolution of polymer blend morphology during compounding in an internal mixer.* Polymer, 1999. **40**(23): p. 6277-6296.
17. Sundararaj, U., et al., *Morphology development in polymer blends.* Polymer Engineering & Science, 1992. **32**(24): p. 1814-1823.
18. Jordhamo, G., J. Manson, and L. Sperling, *Phase continuity and inversion in polymer blends and simultaneous interpenetrating networks.* Polymer Engineering & Science, 1986. **26**(8): p. 517-524.
19. Utracki, L., *On the viscosity-concentration dependence of immiscible polymer blends.* Journal of Rheology, 1991. **35**(8): p. 1615-1637.
20. Ottino, J.M., et al., *Mixing and dispersion of viscous liquids and powdered solids*, in *Advances in chemical engineering*. 1999, Elsevier. p. 105-204.
21. Bentley, B. and L.G. Leal, *An experimental investigation of drop deformation and breakup in steady, two-dimensional linear flows.* Journal of Fluid Mechanics, 1986. **167**: p. 241-283.
22. Tucker III, C.L. and P. Moldenaers, *Microstructural evolution in polymer blends.* Annual Review of Fluid Mechanics, 2002. **34**(1): p. 177-210.
23. De Bruijn, R., *Tipstreaming of drops in simple shear flows.* Chemical engineering science, 1993. **48**(2): p. 277-284.
24. Fenouillot, F., P. Cassagnau, and J.-C. Majesté, *Uneven distribution of nanoparticles in immiscible fluids: Morphology development in polymer blends.* Polymer, 2009. **50**(6): p. 1333-1350.
25. Kong, M., et al., *Retarded relaxation and breakup of deformed PA6 droplets filled with nanosilica in PS matrix during annealing.* Polymer, 2011. **52**(22): p. 5231-5236.
26. Nuzzo, A., et al., *Nanoparticle-induced co-continuity in immiscible polymer blends–A comparative study on bio-based PLA-PA11 blends filled with organoclay, sepiolite, and carbon nanotubes.* Polymer, 2014. **55**(19): p. 4908-4919.

27. Ginzburg, V.V., *Influence of nanoparticles on miscibility of polymer blends. A simple theory.* Macromolecules, 2005. **38**(6): p. 2362-2367.
28. Si, M., et al., *Compatibilizing bulk polymer blends by using organoclays.* Macromolecules, 2006. **39**(14): p. 4793-4801.
29. Altobelli, R., M.S. de Luna, and G. Filippone, *Interfacial crowding of nanoplatelets in co-continuous polymer blends: assembly, elasticity and structure of the interfacial nanoparticle network.* Soft matter, 2017. **13**(37): p. 6465-6473.
30. Filippone, G., G. Romeo, and D. Acierno, *Role of Interface Rheology in Altering the Onset of Co-Continuity in Nanoparticle-Filled Polymer Blends.* Macromolecular Materials and Engineering, 2011. **296**(7): p. 658-665.
31. Willemse, R., et al., *Co-continuous morphologies in polymer blends: a new model.* Polymer, 1998. **39**(24): p. 5879-5887.
32. Wu, G., B. Li, and J. Jiang, *Carbon black self-networking induced co-continuity of immiscible polymer blends.* Polymer, 2010. **51**(9): p. 2077-2083.
33. Cai, X., et al., *Morphology evolution of immiscible polymer blends as directed by nanoparticle self-agglomeration.* Polymer, 2012. **53**(1): p. 259-266.
34. Xiu, H., et al., *Deep insight into the key role of carbon black self-networking in the formation of co-continuous-like morphology in polylactide/poly (ether) urethane blends.* Polymer, 2016. **82**: p. 11-21.
35. de Luna, M.S. and G. Filippone, *Effects of nanoparticles on the morphology of immiscible polymer blends–challenges and opportunities.* European Polymer Journal, 2016. **79**: p. 198-218.
36. Li, L., et al., *Kinetically trapped co-continuous polymer morphologies through intraphase gelation of nanoparticles.* Nano letters, 2011. **11**(5): p. 1997-2003.
37. Pötschke, P., A.R. Bhattacharyya, and A. Janke, *Morphology and electrical resistivity of melt mixed blends of polyethylene and carbon nanotube filled polycarbonate.* Polymer, 2003. **44**(26): p. 8061-8069.
38. Chesters, A.K., *Modelling of coalescence processes in fluid-liquid dispersions: a review of current understanding.* Chemical engineering research and design, 1991. **69**(A4): p. 259-270.
39. Janssen, J.M. and H.E. Meijer, *Dynamics of liquid-liquid mixing: A 2-zone model.* Polymer Engineering & Science, 1995. **35**(22): p. 1766-1780.
40. Lyu, S., F.S. Bates, and C.W. Macosko, *Modeling of coalescence in polymer blends.* AIChE journal, 2002. **48**(1): p. 7-14.

41. Lyu, S.P., F.S. Bates, and C.W. Macosko, *Coalescence in polymer blends during shearing.* AIChE journal, 2000. **46**(2): p. 229-238.
42. Wang, H., A.Z. Zinchenko, and R.H. Davis, *The collision rate of small drops in linear flow fields.* Journal of fluid mechanics, 1994. **265**: p. 161-188.
43. Mousa, H., W. Agterof, and J. Mellema, *Experimental investigation of the orthokinetic coalescence efficiency of droplets in simple shear flow.* Journal of colloid and interface science, 2001. **240**(1): p. 340-348.
44. Shardt, O., S.K. Mitra, and J. Derksen, *The critical conditions for coalescence in phase field simulations of colliding droplets in shear.* Langmuir, 2014. **30**(48): p. 14416-14426.
45. Yoon, Y., et al., *Viscosity ratio effects on the coalescence of two equal-sized drops in a two-dimensional linear flow.* Journal of Fluid Mechanics, 2005. **525**: p. 355-379.
46. Leal, L., *Flow induced coalescence of drops in a viscous fluid.* Physics of fluids, 2004. **16**(6): p. 1833-1851.
47. Vandebril, S., J. Vermant, and P. Moldenaers, *Efficiently suppressing coalescence in polymer blends using nanoparticles: role of interfacial rheology.* Soft Matter, 2010. **6**(14): p. 3353-3362.
48. Palierne, J., *Linear rheology of viscoelastic emulsions with interfacial tension.* Rheologica acta, 1990. **29**(3): p. 204-214.
49. Thareja, P. and S. Velankar, *Rheology of immiscible blends with particle-induced drop clusters.* Rheologica acta, 2008. **47**(2): p. 189-200.
50. Thareja, P., K. Moritz, and S.S. Velankar, *Interfacially active particles in droplet/matrix blends of model immiscible homopolymers: Particles can increase or decrease drop size.* Rheologica acta, 2010. **49**(3): p. 285-298.
51. Zou, Z.-M., Z.-Y. Sun, and L.-J. An, *Effect of fumed silica nanoparticles on the morphology and rheology of immiscible polymer blends.* Rheologica Acta, 2014. **53**(1): p. 43-53.
52. Luna, M.S.d., A. Causa, and G. Filippone, *Interfacially-located nanoparticles anticipate the onset of co-continuity in immiscible polymer blends.* Polymers, 2017. **9**(9): p. 393.
53. Filippone, G. and D. Acierno, *Clustering of coated droplets in clay-filled polymer blends.* Macromolecular Materials and Engineering, 2012. **297**(9): p. 923-928.
54. Elias, L., et al., *Immiscible polymer blends stabilized with nano-silica particles: Rheology and effective interfacial tension.* Polymer, 2008. **49**(20): p. 4378-4385.

55. Taguet, A., P. Cassagnau, and J.-M. Lopez-Cuesta, *Structuration, selective dispersion and compatibilizing effect of (nano) fillers in polymer blends.* Progress in Polymer Science, 2014. **39**(8): p. 1526-1563.
56. Hong, J.S., et al., *The role of organically modified layered silicate in the breakup and coalescence of droplets in PBT/PE blends.* Polymer, 2006. **47**(11): p. 3967-3975.
57. Sumita, M., et al., *Dispersion of fillers and the electrical conductivity of polymer blends filled with carbon black.* Polymer bulletin, 1991. **25**(2): p. 265-271.
58. Owens, D.K. and R. Wendt, *Estimation of the surface free energy of polymers.* Journal of applied polymer science, 1969. **13**(8): p. 1741-1747.
59. Wu, S., *Polymer interface and adhesion*. Vol. 188. 1982: M. Dekker New York.
60. Elias, L., et al., *Migration of nanosilica particles in polymer blends.* Journal of Polymer Science Part B: Polymer Physics, 2008. **46**(18): p. 1976-1983.
61. Dil, E.J. and B.D. Favis, *Localization of micro-and nano-silica particles in heterophase poly (lactic acid)/poly (butylene adipate-co-terephthalate) blends.* Polymer, 2015. **76**: p. 295-306.
62. Dil, E.J. and B.D. Favis, *Localization of micro and nano-silica particles in a high interfacial tension poly (lactic acid)/low density polyethylene system.* Polymer, 2015. **77**: p. 156-166.
63. Göldel, A., et al., *Shape-dependent localization of carbon nanotubes and carbon black in an immiscible polymer blend during melt mixing.* Macromolecules, 2011. **44**(15): p. 6094-6102.
64. Bai, L., et al., *Kinetic control of graphene localization in co-continuous polymer blends via melt compounding.* Langmuir, 2017. **34**(3): p. 1073-1083.
65. Plattier, J., et al., *Viscosity-induced filler localisation in immiscible polymer blends.* Polymer, 2015. **59**: p. 260-269.
66. Feng, J., C.m. Chan, and J.x. Li, *A method to control the dispersion of carbon black in an immiscible polymer blend.* Polymer Engineering & Science, 2003. **43**(5): p. 1058-1063.
67. Clarke, J., et al., *Compatibilising effect of carbon black on morphology of NR–NBR blends.* Plastics, rubber and composites, 2001. **30**(1): p. 39-44.
68. Jaensson, N.O., et al., *Shear-induced migration of rigid particles near an interface between a Newtonian and a viscoelastic fluid.* Langmuir, 2018. **34**(4): p. 1795-1806.

69. Gubbels, F., et al., *Kinetic and thermodynamic control of the selective localization of carbon black at the interface of immiscible polymer blends.* Chemistry of materials, 1998. **10**(5): p. 1227-1235.
70. Strugova, D., et al., *Ultra-Low Percolation Threshold Induced by Thermal Treatments in Co-Continuous Blend-Based PP/PS/MWCNTs Nanocomposites.* Nanomaterials, 2021. **11**(6): p. 1620.
71. Zaikin, A., R. Karimov, and V. Arkhireev, *A study of the redistribution conditions of carbon black particles from the bulk to the interface in heterogeneous polymer blends.* Colloid Journal, 2001. **63**(1): p. 53-59.
72. Dharaiya, D.P., S.C. Jana, and S.F. Lyuksyutov, *Production of electrically conductive networks in immiscible polymer blends by chaotic mixing.* Polymer Engineering & Science, 2006. **46**(1): p. 19-28.
73. Shi, Y.-y., et al., *Selective localization of carbon nanotubes at the interface of poly (L-lactide)/ethylene-co-vinyl acetate resulting in lowered electrical resistivity.* Composites Part B: Engineering, 2013. **55**: p. 463-469.
74. Mun, S.C., et al., *Strategies for interfacial localization of graphene/polyethylene-based cocontinuous blends for electrical percolation.* AIChE Journal, 2019. **65**(6).
75. Gao, T., et al., *Tailoring co-continuous like morphology in blends with highly asymmetric composition by MWCNTs: Towards biodegradable high-performance electrical conductive poly (l-lactide)/poly (3-hydroxybutyrate-co-4-hydroxybutyrate) blends.* Composites Science and Technology, 2017. **152**: p. 111-119.
76. Gao, J.-F., et al., *Large-scale fabrication and electrical properties of an anisotropic conductive polymer composite utilizing preferable location of carbon nanotubes in a polymer blend.* Composites Science and Technology, 2010. **70**(13): p. 1973-1979.
77. Favis, B.D. and J.-P. Chalifoux, *The effect of viscosity ratio on the morphology of polypropylene/polycarbonate blends during processing.* Polymer Engineering & Science, 1987. **27**(21): p. 1591-1600.
78. Trifkovic, M., et al., *Stabilization of PE/PEO cocontinuous blends by interfacial nanoclays.* Macromolecules, 2015. **48**(13): p. 4631-4644.
79. Yan, D., et al., *Improved electrical conductivity of polyamide 12/graphene nanocomposites with maleated polyethylene-octene rubber prepared by melt compounding.* ACS applied materials & interfaces, 2012. **4**(9): p. 4740-4745.
80. Harrats, C., et al., *Molecular design of multicomponent polymer systems XIX: Stability of cocontinuous phase morphologies in low-density polyethylene–polystyrene blends*

emulsified by block copolymers. Journal of Polymer Science Part B: Polymer Physics, 1995. **33**(5): p. 801-811.

81. Zhang, K., L. Jiang, and G. Wu, *Co-continuity and thermal expansion of injection-molded EPDM/PP blends with heterogeneous dispersion of nanoparticles.* Composites Science and Technology, 2016. **125**: p. 123-131.
82. Xiu, H., et al., *Improving impact toughness of polylactide/poly (ether) urethane blends via designing the phase morphology assisted by hydrophilic silica nanoparticles.* Polymer, 2014. **55**(6): p. 1593-1600.
83. Xiu, H., et al., *Formation of new electric double percolation via carbon black induced co-continuous like morphology.* RSC Advances, 2014. **4**(70): p. 37193-37196.
84. Cox, W. and E. Merz, *Correlation of dynamic and steady flow viscosities.* Journal of Polymer Science, 1958. **28**(118): p. 619-622.
85. Ishak, Z.M., W. Chow, and T. Takeichi, *Influence of SEBS-g-MA on morphology, mechanical, and thermal properties of PA6/PP/organoclay nanocomposites.* European Polymer Journal, 2008. **44**(4): p. 1023-1039.
86. Shen, Y. and H. Wu, *Interlayer shear effect on multilayer graphene subjected to bending.* Applied Physics Letters, 2012. **100**(10): p. 101909.
87. Pawar, S.P. and S. Bose, *Peculiar morphological transitions induced by nanoparticles in polymeric blends: retarded relaxation or altered interfacial tension?* Physical Chemistry Chemical Physics, 2015. **17**(22): p. 14470-14478.
88. Ghasemi, I. and S. Gomari, *Polymeric Nanocomposites Including Graphene Nanoplatelets.* Handbook of Graphene Set, 2019. **1**: p. 481-515.
89. Dai, K., X.-B. Xu, and Z.-M. Li, *Electrically conductive carbon black (CB) filled in situ microfibrillar poly (ethylene terephthalate)(PET)/polyethylene (PE) composite with a selective CB distribution.* Polymer, 2007. **48**(3): p. 849-859.
90. Balberg, I., *A comprehensive picture of the electrical phenomena in carbon black–polymer composites.* Carbon, 2002. **40**(2): p. 139-143.
91. Tan, Y., et al., *Grafting of copolymers onto graphene by miniemulsion polymerization for conductive polymer composites: improved electrical conductivity and compatibility induced by interfacial distribution of graphene.* Polymer Chemistry, 2013. **4**(10): p. 2939-2944.
92. Jose, S., et al., *Phase morphology, crystallisation behaviour and mechanical properties of isotactic polypropylene/high density polyethylene blends.* European polymer journal, 2004. **40**(9): p. 2105-2115.

93. Di Lorenzo, M.L., *Spherulite growth rates in binary polymer blends.* Progress in Polymer Science, 2003. **28**(4): p. 663-689.

94. Frensch, H., P. Harnischfeger, and B. Jungnickel, *Fractionated crystallization in incompatible polymer blends.* Multiphase polymers: blends and ionomers, 1989. **395**: p. 101.

95. Laoutid, F., et al., *The influence of nanosilica on the nucleation, crystallization and tensile properties of PP–PC and PP–PA blends.* Polymer, 2013. **54**(15): p. 3982-3993.

96. Khatua, B., et al., *Effect of organoclay platelets on morphology of nylon-6 and poly (ethylene-r an-propylene) rubber blends.* Macromolecules, 2004. **37**(7): p. 2454-2459.

97. Solomon, M.J., et al., *Rheology of polypropylene/clay hybrid materials.* Macromolecules, 2001. **34**(6): p. 1864-1872.

98. Amoabeng, D., et al., *A composition-morphology map for particle-filled blends of immiscible thermoplastic polymers.* Polymer, 2017. **119**: p. 212-223.

99. Hadaeghnia, M., et al., *Manipulating the morphology of PA6/POE blends using graphene to achieve balanced electrical and mechanical properties.* Composites Science and Technology, 2020: p. 108412.

100. Yuryev, Y. and P. Wood-Adams, *Rheological properties of crystallizing polylactide: Detection of induction time and modeling the evolving structure and properties.* Journal of Polymer Science Part B: Polymer Physics, 2010. **48**(7): p. 812-822.

101. Schneider, C.A., W.S. Rasband, and K.W. Eliceiri, *NIH Image to ImageJ: 25 years of image analysis.* Nature methods, 2012. **9**(7): p. 671-675.

102. Kong, M., et al., *Morphology mapping of nanoparticle-filled immiscible polymer blends in flow: the existence of a critical ratio between nanoparticle concentration and droplet concentration.* ACS omega, 2018. **3**(9): p. 11550-11557.

103. Fortelný, I. and A. Źivný, *Film drainage between droplets during theircoalescence in quiescent polymer blends.* Polymer, 1998. **39**(12): p. 2669-2675.

104. Fortelný, I., et al., *The effect of anisometry of dispersed droplets on their coalescence during annealing of polymer blends.* Colloid and Polymer Science, 2011. **289**(17): p. 1895-1903.

105. Nagarkar, S.P. and S.S. Velankar, *Morphology and rheology of ternary fluid–fluid–solid systems.* Soft matter, 2012. **8**(32): p. 8464-8477.

106. Kim, H. and C.W. Macosko, *Processing-property relationships of polycarbonate/graphene composites.* Polymer, 2009. **50**(15): p. 3797-3809.

107. Treece, M.A. and J.P. Oberhauser, *Ubiquity of soft glassy dynamics in polypropylene–clay nanocomposites.* Polymer, 2007. **48**(4): p. 1083-1095.

108. Huang, S., et al., *Controlling the morphology of immiscible cocontinuous polymer blends via silica nanoparticles jammed at the interface.* Macromolecules, 2016. **49**(10): p. 3911-3918.

109. Trappe, V. and D. Weitz, *Scaling of the viscoelasticity of weakly attractive particles.* Physical review letters, 2000. **85**(2): p. 449.

110. Filippone, G. and M. Salzano de Luna, *A unifying approach for the linear viscoelasticity of polymer nanocomposites.* Macromolecules, 2012. **45**(21): p. 8853-8860.

111. Filippone, G., et al., *Assembly of plate-like nanoparticles in immiscible polymer blends–effect of the presence of a preferred liquid–liquid interface.* Soft Matter, 2014. **10**(18): p. 3183-3191.

112. Nakhle, W. and P. Wood-Adams, *Solvent diffusion in molten polystyrene under small amplitude oscillatory shear.* Polymer, 2017. **132**: p. 59-68.

113. Nakhle, W., M.-C. Heuzey, and P.M. Wood-Adams. *Interdiffusion dynamics at the interface between two polystyrenes with different molecular weight probed by a rheological tool*. in *AIP Conference Proceedings*. 2019. AIP Publishing LLC.

114. Shih, W.-H., et al., *Scaling behavior of the elastic properties of colloidal gels.* Physical review A, 1990. **42**(8): p. 4772.

115. Sabzi, M., et al., *Graphene nanoplatelets as poly (lactic acid) modifier: linear rheological behavior and electrical conductivity.* Journal of materials chemistry A, 2013. **1**(28): p. 8253-8261.

116. Spinelli, G., et al., *Rheological and electrical behaviour of nanocarbon/poly (lactic) acid for 3D printing applications.* Composites Part B: Engineering, 2019. **167**: p. 467-476.

117. Domenech, T., et al., *Formation of fractal-like structure in organoclay-based polypropylene nanocomposites.* Macromolecules, 2014. **47**(10): p. 3417-3427.

118. Kim, H. and C.W. Macosko, *Morphology and properties of polyester/exfoliated graphite nanocomposites.* 2008.

119. Jonscher, A.K., *The 'universal'dielectric response.* nature, 1977. **267**(5613): p. 673-679.

120. Kilbride, B.e., et al., *Experimental observation of scaling laws for alternating current and direct current conductivity in polymer-carbon nanotube composite thin films.* Journal of applied physics, 2002. **92**(7): p. 4024-4030.
121. Barrau, S., et al., *DC and AC conductivity of carbon nanotubes− polyepoxy composites.* Macromolecules, 2003. **36**(14): p. 5187-5194.
122. Liebscher, M., et al., *A morphological study on the dispersion and selective localization behavior of graphene nanoplatelets in immiscible polymer blends of PC and SAN.* Polymer, 2013. **54**(21): p. 5875-5882.
123. Li, J., P.L. Ma, and B.D. Favis, *The role of the blend interface type on morphology in cocontinuous polymer blends.* Macromolecules, 2002. **35**(6): p. 2005-2016.
124. Sundararaj, U. and C. Macosko, *Drop breakup and coalescence in polymer blends: the effects of concentration and compatibilization.* Macromolecules, 1995. **28**(8): p. 2647-2657.
125. Wu, S., *Formation of dispersed phase in incompatible polymer blends: Interfacial and rheological effects.* Polymer Engineering & Science, 1987. **27**(5): p. 335-343.
126. Kamkar, M., et al., *Structural characterization of CVD custom-synthesized carbon nanotube/polymer nanocomposites in large-amplitude oscillatory shear (LAOS) mode: Effect of dispersion characteristics in confined geometries.* Macromolecules, 2019. **52**(4): p. 1489-1504.
127. Dong, Y. and D. Bhattacharyya, *Effects of clay type, clay/compatibiliser content and matrix viscosity on the mechanical properties of polypropylene/organoclay nanocomposites.* Composites Part A: Applied Science and Manufacturing, 2008. **39**(7): p. 1177-1191.
128. Hadaeghnia, M., et al., *Evolution of Phase Morphology, Rheology, and Electrical Conductivity of PA6/POE Blends Containing Graphene during Annealing under SAOS.* Macromolecules, 2022.
129. Mazidi, M.M., et al., *Structure–property relationships in super-toughened polypropylene-based ternary blends of core–shell morphology.* Rsc Advances, 2016. **6**(2): p. 1508-1526.
130. Gomari, S., et al., *Organoclay localization in polyamide 6/ethylene-butene copolymer grafted maleic anhydride blends: the effect of different types of organoclay.* Journal of Polymer Research, 2012. **19**(1): p. 9769.
131. Israelachvili, J.N., *Intermolecular and surface forces*. 2015: Academic press.